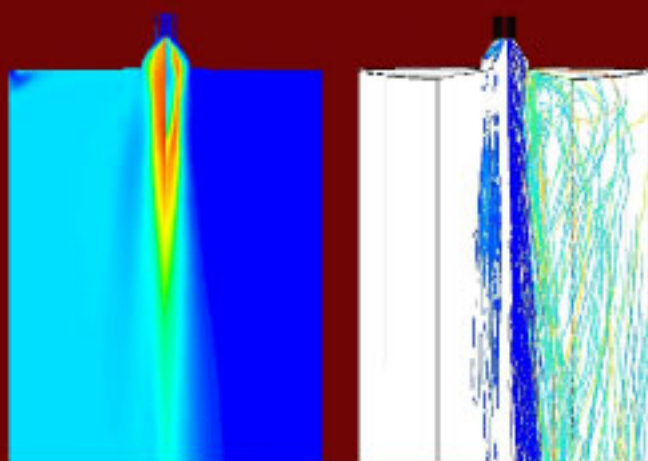


Sylvie Honnet

Detailed and Reduced Kinetic Mechanisms in Low-Emission Combustion Processes



Cuvillier Verlag Göttingen

Detailed and Reduced Kinetic Mechanisms in Low-Emission Combustion Processes

Der Fakultät für Maschinenwesen der Rheinisch-Westfälischen
Technischen Hochschule Aachen vorgelegte Dissertation zur
Erlangung des akademischen Grades einer Doktorin der
Ingenieurwissenschaften

von

Sylvie Honnet

aus

Evreux (Frankreich)

Berichter:

Univ.-Prof. Dr.-Ing. Dr. h. c. Dr.-Ing. E. h. N. Peters

Univ.-Prof. Dr.-Ing. R. Kneer

Tag der mündlichen Prüfung: 17. September 2007

Bibliografische Information Der Deutschen Bibliothek

Die Deutsche Bibliothek verzeichnet diese Publikation in der Deutschen Nationalbibliografie; detaillierte bibliografische Daten sind im Internet über <http://dnb.ddb.de> abrufbar.

1. Aufl. - Göttingen : Cuvillier, 2007

Zugl.: (TH) Aachen, Univ., Diss., 2007

978-3-86727-391-6

© CUVILLIER VERLAG, Göttingen 2007

Nonnenstieg 8, 37075 Göttingen

Telefon: 0551-54724-0

Telefax: 0551-54724-21

www.cuvillier.de

Alle Rechte vorbehalten. Ohne ausdrückliche Genehmigung des Verlages ist es nicht gestattet, das Buch oder Teile daraus auf fotomechanischem Weg (Fotokopie, Mikrokopie) zu vervielfältigen.

1. Auflage, 2007

Gedruckt auf säurefreiem Papier

978-3-86727-391-6

To Vincent

Vorwort

Die vorliegende Arbeit entstand während meiner Tätigkeit als wissenschaftliche Mitarbeiterin am Institut für Technische Verbrennung der Rheinisch-Westfälischen Technischen Hochschule Aachen.

Mein besonderer Dank gilt Herrn Professor Dr.-Ing. Dr. h.c. Dr.-Ing. E.h. N. Peters für die Anregung und Förderung dieser Arbeit, seinen fachlichen Rat sowie seine vielfältige, wertvolle Unterstützung. Herrn Professor Dr.-Ing. R. Kneer danke ich für seine Tätigkeit als weiterer Berichterstatter und Herrn Professor Dr.-Ing. K. Lucas für die Übernahme des Vorsitzes der Prüfungskommission.

Danken möchte ich auch dem Geschäftsführer des Instituts für Technische Verbrennung, Herrn D. Osthoff, für die gute Zusammenarbeit während meiner Tätigkeit.

Herr Dr. D. Toporov hat mir in zahlreichen Diskussionen wertvolle Ideen und Hinweise gegeben. Hierfür sei ihm an dieser Stelle herzlich gedankt.

Allen Mitarbeitern des Instituts, die mich bei der Durchführung dieser Arbeit unterstützt haben, möchte ich ebenfalls danken. Insbesondere gilt mein Dank Jost Weber, Georgios Bikas, Elmar Riesmeier, Stefan Vogel und Jens Henrik Göbbert.

Meinem Mann Vincent danke ich für die geduldige Unterstützung, auf die ich mich stets verlassen konnte.

Aachen, im September 2007

Sylvie Honnet

Detailed and Reduced Kinetic Mechanisms in Low-Emission Combustion Processes

Zusammenfassung

Gegenstand der vorliegenden Arbeit ist die Anwendung des Representative Interactive Flamelet (RIF) Modells mit detaillierter und reduzierter Kinetik zur Beschreibung von Verbrennungsprozessen mit niedrigen Schadstoffemissionen. Chemische kinetische Reaktionsmechanismen werden entwickelt. Hinsichtlich der Anwendung dieser Mechanismen in der numerischen Simulation von Verbrennungsprozessen wird insbesondere die Beschreibung der Stickoxidbildung berücksichtigt.

Nach einer Einführung in die Thematik stellt Kapitel 2 die Erhaltungsgleichungen, die Beschreibung der turbulenten Strömungs- und Mischungsfelder vor. Das Flamelet Modell und das RIF-Konzept werden beschrieben: die chemische Reaktionskinetik wird von der Strömungsdynamik isoliert betrachtet. Es wird durch die Annahme der Existenz einer sehr dünnen Flammenschicht ermöglicht, in der die chemischen Prozesse ablaufen. Diese auch in turbulenten Strömungen als laminar betrachtete Flammenschicht wird Flamelet genannt. Die Berechnung der Zündung, Wärmefreisetzung und Stickstoffbildung mit detaillierter Kinetik wird dadurch ermöglicht.

In Kapitel 3 wird ein Modell zur Berechnung dreidimensionaler Verbrennungsvorgänge vorgestellt. Es basiert auf dem Flamelet Modell. Zur Berücksichtigung der Stickoxid-Bildung ist die Betrachtung der Verbrennung als instationärer Prozess von besonderer Bedeutung. Dies wird durch die Verwendung instationärer Flamelets ermöglicht. Die Flamelets werden interaktiv mit dem Strömungslöser jeweils repräsentativ für einen bestimmten Weg von Partikeln durch die Brennkammer berechnet. Der statistische Weg der Fluid-Partikel durch die Brennkammer wird mit Euler'schen Transportgleichungen beschrieben.

In Kapitel 4 werden chemische Reaktionsmechanismen erstellt und durch Vergleich mit experimentellen Ergebnissen validiert. Besonders Augenmerk wird auf den Methan-Mechanismus mit Berücksichtigung der Stickoxid-Bildung gelegt. Dieser Mechanismus wird anhand Stationnaritätsannahmen reduziert. Zusätzlich werden ein Pyrolyse- und Abbrand-Modell vorgestellt, die bei der Simulation der Kohleverbrennung in Kapitel 5 angewendet werden.

In Kapitel 5 werden Simulationsergebnisse für zwei unterschiedlichen Konfigurationen mit experimentellen Daten verglichen. Bei der MILD-Brennkammer wird die Stickoxid-Bildung unter Anwendung der in Kapitel 4 vorgestellten detaillierten und reduzierten Kinetik untersucht. Das Eulerian Particle Flamelet Modell wird ergänzt und bei der Simulation der Gasphase während der Kohleverbrennung angewendet.

Auf Basis der Ergebnisse wird gezeigt, dass das mit detaillierter und reduzierter Kinetik gekoppelte Flamelet Modell in der Lage ist, Verbrennungsprozesse mit niedrigen Schadstoffemissionen zu modellieren.

Contents

1	Introduction	1
2	Mathematical Models	5
2.1	Conservation Equations	5
2.2	Turbulence Modelling	8
2.2.1	Mean Values in Turbulent Flows	10
2.2.2	Turbulence Models	11
2.3	Laminar Flamelets	14
2.3.1	Definition of the Mixture Fraction	15
2.3.2	Flamelet Equations	17
2.3.3	Flamelet Parameters	20
2.4	The Representative Interactive Flamelet (RIF) Model	23
2.4.1	Presumed Shape Pdf Ansatz	23
2.4.2	Temporal Change of the Flamelet Parameter	25
3	Numerical Implementation	27
3.1	CFD code	27
3.1.1	Ansatz of the Pdf-mixture fraction	28
3.1.2	Burke-Schumann solution	30
3.1.3	Chemical equilibrium	31
3.2	Coupling of the CFD and the RIF-Codes	32
3.2.1	Supply of the Flamelet Parameters	32
3.3	The Eulerian Particle Flamelet Model	35
3.3.1	Flamelet Initialization	36
3.3.2	Distribution of the Flamelet Parameter	37
3.3.3	Temporal Evolution of the Flamelet Profile	37

4	Chemical Mechanisms	43
4.1	C ₁ -C ₂ Kinetics	43
4.1.1	Reaction paths	43
4.1.2	Validation	45
4.2	NO _x Model	47
4.3	Reduction of Chemical Mechanisms	50
4.3.1	Steady-State Assumptions for Radicals	50
4.3.2	The Reduced Mechanism	51
4.3.3	Concluding Remarks	58
4.4	Combustion of Solid Carbon Particles	59
4.4.1	Pyrolysis Model	60
4.4.2	Burnout Model	61
5	Results and Discussions	63
5.1	Simulation of a MILD Combustor	63
5.1.1	Experimental Set-up	64
5.1.2	Computational Grid	67
5.1.3	Comparison with the Experimental Results	67
5.2	Simulation of the Combustion in a Pressurised Pulverized Coal Combustion Facility	75
5.2.1	Experimental Set-up	75
5.2.2	Computational Grid	76
5.2.3	Comparison with the Experimental Results	79
6	Summary and Conclusions	99
A	Chemical Mechanism	109
B	Global Rates	115
C	Coal Analysis	123
D	Influence of the Initial Composition of Volatiles	125
E	Nomenclature	128

Chapter 1

Introduction

The last centuries were marked by a large-scale industrial development due to the use of fossil fuels which are the main source of energy not only for heating but also for power generation and transportation. As a consequence of this increased consumption of fossil fuels, two major features have to be taken into account. First, fossil fuels are not renewable, thus leading to a deficit of fuels when their sources will be depleted. Furthermore, the burning of fossil fuels by humans is the largest source of emissions of carbon dioxide, which is one of the greenhouse gases that contributes to the global warming of the Earth. Other emissions during combustion processes are soot, often thought to be cancerogeneous, and NO_x , responsible for the acid rain and the ozon formation.

That is the reason of the necessity to increase the efficiency of the combustion and reduce pollutant formation. Then for example, more power could be obtained by consuming less fuel and emitting no or less pollutant.

It implies a good understanding of all the processes taking place during the combustion. For that purpose, the models of these complex processes are still subject to intensive research.

Until 2020 it is foreseen to build many new power plants in Germany and Europe due to the aging of those currently in use. Furthermore an increase of the power installations in Europe is already predicted [35].

It is not clear whether the renewable energies will be able to cover this need. Since the future contributions from the nuclear energy cannot be predicted, there remains the use of fossil fuels. Because of the disponibility, delivery guarantee and economics on a long-time scale, the use of coal is particularly

interesting.

Nevertheless, an increasing use of coal also results in an increase of CO₂ emission, which is in contradiction to the 1997 Kyoto protocol [86] ratified by 168 nations and one regional economic integration organization (the EEC) as of the 26 February 2007. Of these, 35 countries and the EEC are required to reduce greenhouse gas emissions below levels specified for each of them in the treaty. These add up to a total cut in greenhouse-gas emissions of at least 5% from 1990 levels in the commitment period 2008-2012.

In order to overcome this problem, new techniques are developed. One of them consists in a combustion not with combustion air for the oxidizer as usually done, but with a mixture of oxygen and flue gas, the oxygen being supplied by a high temperature membrane. It is the OXYCOAL-AC process [61].

Nowadays the development of such new techniques is supported by three-dimensional simulations which have the advantage of giving an insight into the combustion processes on a short-time scale with low costs compared to what experiments would offer. For that purpose, the models used in the Computational Fluid Dynamics (CFD) for the combustion processes must be reliable to give results of good quality. Many studies were already done in the past for different regimes and under different configurations (for example Diesel combustion [6], MILD combustion [18], [37], premixed [32] and partially premixed combustion [19]) with different fuels such as methane [8], [7], [54], [10], [80], n-heptane [20], [12], n-decane [23], [13] as well as multi-component fuels [73].

For the coal combustion as well as for gaseous combustion such as in industrial furnaces, special attention on the reaction mechanisms should be paid. Combustion takes place in reaction chains. Chemical kinetic reaction mechanisms describe all the chemical processes during the combustion from fuel oxidation to pollutant formation. A chemical kinetic mechanism is thus the basis for a good simulation. The field of kinetics has been the object of scientific studies for a long time. However there still is a need to improve the existing data, especially under certain boundary conditions that were not used until now. Once validated against various experimental data, these detailed reaction mechanisms are introduced into complex multi-dimensional fluid dynamics codes for combustion simulations. Despite the increasing computational capacities, those detailed mechanisms may be too long for CFD simulations and then require too much calculation time. The reduction of reaction mechanisms is particularly attractive since it enables to reduce the

computational effort without losing much information.

A major objective of this work has been to develop and upgrade kinetic mechanisms for model fuels in order to simulate the complex physico-chemical interactions in practical combustion systems. The mechanisms, after they have been assembled, have been validated against a wide range of combustion regimes.

In chapter 2 the mathematical models for simulating the combustion are presented. Then the laminar flamelets are introduced and the RIF concept is described.

In chapter 3 a model to calculate three-dimensional combustion processes is explained. It is based on the flamelet model, which considers the chemical reaction kinetics isolated from the flow dynamics. This is made possible thanks to the assumption of the existence of very thin layers in which the chemical processes occur. These laminar thin layers in the turbulent flow are called flamelets. The flamelet model enables the calculation of ignition, heat release and pollutant formation under consideration of detailed and reduced chemical reaction kinetics. The consideration of combustion as an unsteady process is of particular interest. This is achieved by using unsteady flamelets. The flamelets are interactively calculated with a flow solver for a particular path of particles through the furnace. That is why these flamelets are called Representative Interactive Flamelets. The statistical path of a fluid particle through the furnace is described by the Eulerian transport equations.

The developed chemical mechanism for the description of the detailed reaction kinetics of methane is presented in chapter 4. The detailed mechanism for methane is composed of 143 elementary reactions with 35 species. Further to the reactions to describe the fuel decomposition, the mechanism also contains a detailed description of NO_x formation. This carefully validated mechanism was reduced by introduction of steady-state assumptions.

In chapter 4, the pyrolysis models used for the simulation of the coal combustion in chapter 5 are also described.

To validate the presented models and show the ability of a reduced mechanism to reproduce the results of a detailed numerical simulation of a *FLOX*[®] furnace is performed. Flameless oxidation (*FLOX*[®]) or flameless combustion is a well-known low- NO_x combustion technique for industrial furnaces. The FLOX concept was developed and patented in 1990 by WS [92]. Flameless combustion is based on the principle of internal flue gas recirculation in a combustor. If recirculation rates are high enough and flue gas, combustion

air and fuel are mixed prior to ignition, a diluted homogeneous volumetric combustion mode at a reduced partial pressure of oxygen is established. Distinct flame fronts, as they are typical for lean premixed flames, are replaced by a volume-type flame mode. This combustion mode is characterised by low NO_x emissions because local temperature peaks are avoided [21], [22]. Such a combustor is numerically investigated.

Finally these models were also implemented so as to simulate the coal combustion in a pressurised pulverized coal combustion facility. Special attention was paid to the gaseous phase. The results of the simulations are compared to experimental measurements for both cases.

Chapter 2

Mathematical Models

In this chapter the mathematical models used in the numerical calculations will be presented.

2.1 Conservation Equations

The flow field is described by a system of coupled, non-linear partial differential equations for mass, momentum and energy. In the case of reactive flows these are the so-called Navier-Stokes equations, the conservation equations for the chemical species as well as for the energy. For non-constant density flows the Navier-Stokes equations are formulated in the conservative form as follows:

$$\frac{\partial \rho}{\partial t} + \nabla \cdot (\rho \mathbf{v}) = 0 \quad (2.1)$$

for the continuity and for the momentum as:

$$\frac{\partial \rho \mathbf{v}}{\partial t} + \nabla \cdot (\rho \mathbf{v} \mathbf{v}) = -\nabla p + \nabla \cdot \tau + \rho \mathbf{g}. \quad (2.2)$$

In Eqs. (2.1) and (2.2) ρ denotes the density, \mathbf{v} the velocity vector and p the pressure. The Newton viscous stress tensor τ is defined by

$$\tau = \left[2\mu \mathbf{S} - \left(\frac{2}{3}\mu - \kappa \right) \nabla \cdot \mathbf{v} \mathbf{E} \right], \quad (2.3)$$

where \mathbf{E} is the identity matrix and

$$\mathbf{S} = \frac{1}{2} [\nabla \mathbf{v} + (\nabla \mathbf{v})^T]. \quad (2.4)$$

Here μ denotes the dynamic viscosity which is related to the kinematic viscosity by

$$\mu = \rho\nu. \quad (2.5)$$

The bulk viscosity κ is small compared to the dynamic viscosity and is therefore usually neglected. The term $\rho\mathbf{g}$ in Eq. (2.2) accounts for buoyancy effects.

Next to the Navier-Stokes equations for continuity and momentum other conservation equations are necessary for the simulation of combustion processes. These are the conservation equations for the chemical species and the energy.

The conservation equation for mass fraction Y_i of chemical species i is given by

$$\frac{\partial \rho Y_i}{\partial t} + \nabla \cdot (\rho \mathbf{v} Y_i) = -\nabla \cdot \mathbf{j}_i + \omega_i, \quad i = 1, 2, \dots, n_s, \quad (2.6)$$

where n_s represents the total number of species. \mathbf{j}_i denotes the molecular diffusion flux and ω_i is the chemical source term. The molecular diffusion flux is formally defined as

$$\mathbf{j}_i = \rho(\mathbf{v}_i + \mathbf{v}), \quad (2.7)$$

where \mathbf{v}_i is the mass average velocity of species i . A transport equation for \mathbf{v}_i can be derived (Williams [91]). But the additional effort to solve these equations is not desirable, especially in turbulent flows where the molecular diffusion flux is usually negligible compared to the turbulent transport. Therefore it is useful to consider simplified versions of the diffusive fluxes. Assuming binary diffusion of a species i in another one present in high concentration and according Fick's first law for binary diffusion, the diffusive flux can be described as

$$\mathbf{j}_i = -\rho D_i \nabla Y_i, \quad (2.8)$$

where D_i is the binary diffusion coefficient of species i with respect to an abundant species, for example N_2 .

The conservation equation for enthalpy is

$$\frac{\partial \rho h}{\partial t} + \nabla \cdot (\rho \mathbf{v} h) = \frac{Dp}{Dt} - \nabla \cdot \mathbf{j}_q + \dot{q}_r. \quad (2.9)$$

In this equation, h is the mass weighted sum of specific enthalpies h_i of species i :

$$h = \sum_{i=1}^{n_s} Y_i h_i. \quad (2.10)$$

The specific enthalpies are calculated with

$$h_i = \Delta h_{f,i}^0 + \int_{T^0}^T c_{pi} dT \quad (2.11)$$

as sum of the standard formation enthalpy $\Delta h_{f,i}^0$ taken at the reference temperature T^0 and the thermal enthalpy. The heat flux vector \mathbf{j}_q accounts for thermal diffusion by temperature gradients and enthalpy transport by species diffusion

$$\mathbf{j}_q = -\lambda \nabla T + \sum_{i=1}^{n_s} h_i \mathbf{j}_i, \quad (2.12)$$

where λ is the thermal conductivity. The last term in Eq. (2.9), \dot{q}_r , represents radiative heat loss. With the definition of the enthalpy in Eq. (2.10) an alternative formulation for the conservation of energy can be given. With the relation

$$dh = \frac{\partial h}{\partial T} dT + \sum_{i=1}^{n_s} \frac{\partial h}{\partial Y_i} dY_i = c_p dT + \sum_{i=1}^{n_s} h_i dY_i \quad (2.13)$$

this alternative formulation in the form of an energy equation is formulated with temperature:

$$\begin{aligned} \frac{\partial \rho T}{\partial t} + \nabla \cdot (\rho \mathbf{v} T) = \nabla \cdot \left(\frac{\lambda}{c_p} \nabla T \right) + \rho \frac{\lambda}{c_p^2} \left[\sum_{i=1}^{n_s} \frac{c_{pi}}{Le_i} \nabla Y_i + \nabla c_p \right] \nabla T \\ - \frac{1}{c_p} \left[\sum_{i=1}^{n_s} \omega_i h_i - \frac{Dp}{Dt} - \dot{q}_r \right]. \end{aligned} \quad (2.14)$$

c_p is the specific heat capacity at constant pressure. The Lewis numbers Le_i are defined by

$$Le_i = \frac{\lambda}{\rho D_i c_p} \quad (2.15)$$

and describe the ratio between thermal diffusion $a = \lambda/(\rho c_p)$ and effective diffusion. D_i represents the diffusion coefficient of species i . In order to take

the effects of differential diffusion (Pitsch et al. [74]) into account flamelet equations with additional correction terms for the differential diffusion velocities can be derived. In the cases considered here (i.e. if not specified) the differential diffusion is neglected and the Lewis number of species i is set equal to 1.

The system of equations is closed by the equation of state for a mixture of ideal gases

$$\frac{p}{\rho} = R_{gas} \sum_{i=1}^{n_s} \frac{Y_i}{W_i} T, \quad (2.16)$$

where R_{gas} is the universal gas constant and W_i denotes the molecular weight of species i .

2.2 Turbulence Modelling

When considering turbulent reactive flows, the characteristic properties of turbulence have to be taken into account in the equations that describe the physical relations. The Navier-Stokes equations for the momentum and continuity or the enthalpy equation to simulate turbulent non-premixed combustion processes in real geometries cannot be directly solved because of their complexity due to the stochastic nature of turbulence and thus the division in different time and length scales. That is the reason why such combustion processes are solved by statistical models.

The essential property of turbulent flows is the apparition of eddies with different orders of magnitude or length scales. The eddy of the large length scales are determined by the geometry of the considered problem. The dimension of this eddy is described as the integral length scale, which can be expressed by the turbulent kinetic energy k and the dissipation of the kinetic energy ϵ :

$$l_0 = \frac{k^{3/2}}{\epsilon}. \quad (2.17)$$

The corresponding integral time scale is defined by:

$$\tau_0 = \frac{k}{\epsilon} \quad (2.18)$$

and can be interpreted as the time that an eddy with the length l_0 and the velocity v_0 takes to rotate. The velocity v_0 is of the same order of magnitude as the mean velocity fluctuation v .

The integral length scale is of the order of magnitude of the geometry of the considered problem. The turbulent eddies produced by conversion of kinetic energy into shear turbulence decay according to the so-called eddy-cascade theory ([44]) under release of energy in smaller eddies until the smallest scale, the so-called Kolmogorov length, which is smaller than the integral length scale by many orders of magnitude. Then the statistical description of the movement on the small scales at high enough Reynolds numbers is possible thanks to the laminar kinematic viscosity ν and the dissipation rate ϵ , and the Kolmogorov length is defined as:

$$\eta = \left(\frac{\nu^3}{\epsilon} \right)^{1/4} \quad (2.19)$$

with the corresponding time scale

$$\tau_\eta = \left(\frac{\nu}{\epsilon} \right)^{1/2}. \quad (2.20)$$

Because of the molecular diffusion, eddies of the smallest scales are destroyed and the energy dissipates into thermal energy. That is why the smallest scales are also called dissipative scales. The dissipation rate are scaled according to [83] with

$$\epsilon = \frac{v'^3}{l_0}, \quad (2.21)$$

where v' and l_0 are the mean velocity fluctuation and the integral length scale. After introducing the turbulent Reynolds number

$$Re = \frac{v' l_0}{\nu} \quad (2.22)$$

and considering Eqs. (2.18) and (2.19) the ratio of the Kolmogorov length to the integral length scale can be given as a function of the Reynolds number:

$$\frac{\eta}{l_0} \sim Re^{-3/4}. \quad (2.23)$$

In the same way according to [75] for the velocities

$$\frac{v_n}{v_0} \sim Re^{-1/4} \quad (2.24)$$

and for the time scales

$$\frac{\tau_n}{\tau_0} \sim Re^{-1/2}. \quad (2.25)$$

Solving the equations for the description of a turbulent flow needs the resolution of the smallest time and length scales by using a very refined mesh as well as very small time steps in the numerical simulations. These so-called Direct Numerical Simulation (DNS) are possible at the moment, despite an increasing computational capacity, only for simple geometries and medium Reynolds numbers. From the Eqs. (2.23), (2.24) and (2.25), it is clear that the length, time and velocity scales in turbulent flows at high Reynolds numbers cover a large domain, which exceeds the possibility to resolve the smallest scales. In technical flows with high Reynolds numbers so-called statistical turbulence models are used to model the phenomenon on the small scales. For this purpose, an adequate averaging is to be performed for the variables. This will be explained in the next section.

2.2.1 Mean Values in Turbulent Flows

In turbulent flows with variable density, as they appear in combustion processes, it is useful to introduce a density-weighted averaging. This averaging $\tilde{\Phi}$ is denoted as the Favre averaging and is based on the separation of $\Phi(\mathbf{x}, t)$ into the mean value $\tilde{\Phi}(\mathbf{x}, t)$ and the fluctuation $\Phi''(\mathbf{x}, t)$ like:

$$\Phi(\mathbf{x}, t) = \tilde{\Phi}(\mathbf{x}, t) + \Phi''(\mathbf{x}, t). \quad (2.26)$$

The Favre averaging assumes that the average of the product of Φ'' and the density ρ , not the fluctuation Φ'' itself, equals zero

$$\overline{\rho\Phi''} = 0. \quad (2.27)$$

The definition for $\tilde{\Phi}$ can then be derived by multiplying Eq. (2.26) by the density ρ and averaging:

$$\overline{\rho\Phi} = \overline{\rho\tilde{\Phi}} + \overline{\rho\Phi''} = \tilde{\rho}\tilde{\Phi}. \quad (2.28)$$

The mean of the product $\rho\Phi$ is equal to the product of the mean value $\bar{\rho}$ and $\tilde{\Phi}$ since $\tilde{\Phi}$ is already a mean value defined by

$$\tilde{\Phi} = \frac{\overline{\rho\Phi}}{\bar{\rho}}. \quad (2.29)$$

The fluctuating component of the variable Φ is given by

$$\Phi'' = \frac{(\rho\Phi)'}{\bar{\rho}}. \quad (2.30)$$

From the simultaneous measurement of ρ and Φ , the averaging of the product $\rho\Phi$ and division by the mean value of the density, $\tilde{\Phi}$ can be obtained. The realisation of such measurements is not trivial, however the Favre averaging enables the simplification of the averaged Navier-Stokes equations. Thanks to the Favre averaging of Eqs (2.1) and (2.2) the Navier-Stokes equations result in

$$\frac{\partial \bar{\rho}}{\partial t} + \nabla \cdot (\bar{\rho} \tilde{\mathbf{v}}) = 0 \quad (2.31)$$

$$\frac{\partial \bar{\rho} \tilde{\mathbf{v}}}{\partial t} + \nabla \cdot (\bar{\rho} \tilde{\mathbf{v}} \tilde{\mathbf{v}}) = -\nabla \bar{p} + \nabla \cdot \bar{\tau} - \nabla \cdot \widetilde{(\bar{\rho} \mathbf{v}'' \mathbf{v}'')} + \bar{\rho} \mathbf{g}. \quad (2.32)$$

The last equation differs from Eq. (2.2) solely by the third term on the right hand side. This contains the expression $-\widetilde{\bar{\rho} \mathbf{v}'' \mathbf{v}''}$, which is the Reynolds stress tensor. This unknown term represents the first closure problem in the turbulence model. Even if it is possible to set up transport equations for the six components of the Reynolds stress tensor, these equations contain again different non-closed terms. The derived so-called Reynolds stress models for variable density were presented by Jones [38] and Jones and Kakhi [40]. In spite of the complete description of the physical behaviours these models are barely used in the simulation of turbulent combustion processes.

2.2.2 Turbulence Models

In most computer codes, the $k - \epsilon$ model is used to describe the turbulence. This model is based on the assumption to express the Reynolds stress tensor based on the turbulent viscosity and describes flows with isotropic turbulence. Since the $k - \epsilon$ model is based on equations that describe the turbulent transport as a diffusive process, this method is numerically easier

to convert than the Reynolds stress equations.

By introduction of the turbulent viscosity ν_t , often referred to as eddy viscosity, and modelling of the turbulent shear stress considering the product of the turbulent viscosity and the mean velocity gradient according to Boussinesq [16] the expression of the Reynolds stress equations can be simplified:

$$-\bar{\rho} \widetilde{\mathbf{v}'' \mathbf{v}''} = \bar{\rho} \nu_t \left[2\tilde{\mathbf{S}} - \frac{2}{3} \delta_{ij} \nabla \cdot \bar{\mathbf{v}} \right] - \frac{2}{3} \delta_{ij} \bar{\rho} \bar{k}. \quad (2.33)$$

Herein ν_t is the kinematic turbulent viscosity. This variable is not a material property. It is dependent on the local turbulence variables and can be understood as the product of a velocity scale and a length scale. The determination of these variables occurs by means of the applied turbulent model. With the additional needed equations for the determination of the apparent viscosity, the models that are used are splitted up. Prandtl [75] established the turbulent viscosity thanks to the so-called ansatz of the mixing length where the length scale corresponds to the mixing length l_m and the velocity scale to the contribution of the gradient of the mean average of the velocity in the flow field multiplied by the mixing length:

$$\nu_t = l_m^2 \left| \frac{\partial \bar{\mathbf{u}}}{\partial x} \right|. \quad (2.34)$$

Since no additional equation has to be solved, it is a zero-equation model for the determination of the turbulent viscosity. From this it follows that the turbulent viscosity becomes zero when the gradient of the averaged velocity disappears. However inside a free jet high values are found out by direct measurements, even if the gradient of the averaged velocity becomes zero. Hence Kolmogorov [45] and Prandtl [76] later suggested to determine the velocity scale from the turbulent kinetic energy. The mixing length is conserved as length scale and the turbulent viscosity becomes

$$\nu_t = ck^{1/2} l_m. \quad (2.35)$$

The turbulent kinetic energy can be determined with a transport equation according to Prandtl and Kolmogorov. This is then a one-equation model. In such models the length scale is empirically given, whereas in two-equations models the length scale is determined via two-points correlations or, like in the $k - \epsilon$ model, from the turbulent kinetic energy and the turbulent dissipation.

This model was first presented as the standard $k - \epsilon$ model by Jones and Launder [39] and based on condensed contributions [48]. Later on it was overworked with modified constants by Launder and Sharma [49]. Additionally to the introduction of the turbulent viscosity and the solution of the transport equation for the turbulent kinetic energy k , a transport equation for the turbulent dissipation ϵ is applied. The kinematic turbulent viscosity can be expressed by the Favre mean turbulent kinetic energy \tilde{k}

$$\tilde{k} = \frac{1}{2} \widetilde{\mathbf{v}'' \mathbf{v}''} \quad (2.36)$$

and its dissipation $\tilde{\epsilon}$ with the relation

$$\nu_t = c_\mu \frac{\tilde{k}^2}{\tilde{\epsilon}}, \quad c_\mu = 0.09. \quad (2.37)$$

The introduction of the Favre averaged variable \tilde{k} and $\tilde{\epsilon}$ needs modeled transport equations for these variables. These are in their elementariest form for the turbulent kinetic energy

$$\bar{\rho} \frac{\partial \tilde{k}}{\partial t} + \bar{\rho} \nabla \tilde{\mathbf{v}} \tilde{k} = \nabla \cdot \left(\frac{\bar{\rho} \nu_t}{Pr_k} \nabla \tilde{k} \right) - \bar{\rho} \widetilde{\mathbf{v}'' \mathbf{v}''} : \nabla \tilde{\mathbf{v}} - \bar{\rho} \tilde{\epsilon}, \quad (2.38)$$

and for the turbulent dissipation

$$\bar{\rho} \frac{\partial \tilde{\epsilon}}{\partial t} + \bar{\rho} \nabla \tilde{\mathbf{v}} \tilde{\epsilon} = \nabla \cdot \left(\frac{\bar{\rho} \nu_t}{Pr_\epsilon} \nabla \tilde{\epsilon} \right) - c_{\epsilon_1} \bar{\rho} \frac{\tilde{\epsilon}}{\tilde{k}} \widetilde{\mathbf{v}'' \mathbf{v}''} : \nabla \tilde{\mathbf{v}} - c_{\epsilon_2} \bar{\rho} \frac{\tilde{\epsilon}^2}{\tilde{k}}. \quad (2.39)$$

In these equations the terms on the left hand side describe the local time change and convection. The first term on the right hand side describes the turbulent transport, the second one represents the turbulent production term, and the third one the turbulent dissipation. When applying the standard $k - \epsilon$ model, the constants given in Table 2.1 are most of the time taken into account.

The dissipation rate ϵ has a decisive signification in the turbulence theory. The eddy-cascade theory interprets the dissipation as the energy transfer from the large to the small eddies. That is why it is unchanged in the initial domain of the turbulence. Then when considering this property for ϵ in the equation for the turbulent kinetic energy k , solutions independent of the

Pr_k	Pr_ϵ	$c_{\epsilon 1}$	$c_{\epsilon 2}$
1.0	1.3	1.44	1.92

Table 2.1: Constants used in the $k - \epsilon$ model.

Reynolds number can be found for free shear flows [66].

Because of its high robustness in numerical calculations, the concept of the eddy viscosity in relation with the $k - \epsilon$ model is widely spread, even if it is a highly simplified consideration of the complex properties of the turbulence, thus leading to restrictions.

2.3 Laminar Flamelets

Combustion phenomena are classified into two different major modes: the premixed and the non-premixed combustion. For the premixed systems the fuel and the oxidizer are already premixed before entering the combustion chamber. For the non-premixed systems, on the contrary, the fuel and the oxidizer enter separately into the combustion chamber initially non-premixed. Mixing then takes place by convection and diffusion. Only where fuel and oxidizer are mixed on the molecular level, chemical reactions can take place. This is why flames in non-premixed combustion are called diffusion flames. A classical example of a diffusion flame is a candle flame.

The concept of laminar flamelets in turbulent combustion is based on the assumption that the reaction zone is a thin layer which is smaller than the smallest turbulent scale, the Kolmogorov scale. The turbulent eddies can stretch the reaction zone but cannot intrude into the reaction zone. Therefore the laminar structure is preserved. Williams introduced the concept to view a turbulent diffusion flame as an ensemble of stretched laminar flames [90].

Burke and Schumann [17] realized that the structure of diffusion flames can be approximated by thin reacting layers separating broad inert diffusion zones. They introduced the so-called coupling functions that represent linear combinations of dependent variables and are conserved scalars. Liñán [53] derived conservation equations without convection terms for tempera-

ture and chemical species by introducing adequate coupling functions and expressing temperature and chemical species as functions of the coupling functions. Bilger [14] used a general form of coupling functions. For a system with two inlet streams he defined this general form of coupling functions by normalization onto the values of the inlet streams:

$$Z = \frac{\beta - \beta_2}{\beta_1 - \beta_2}, \quad (2.40)$$

where β is an arbitrary coupling function. This quantity Z is called the mixture fraction. It is a conserved scalar which will have the value 1 in stream 1 and the value 0 in stream 2, independently of the actual composition of the inlet streams.

2.3.1 Definition of the Mixture Fraction

Before defining the mixture fraction as in Eq. (2.40) an adequate coupling function has to be identified. Chemical species are consumed and produced during a chemical reaction, whereas chemical elements (like C, H, N or O) are unaffected. For the element mass fraction of a chemical element j given by

$$Z_j = \sum_{i=1}^{n_s} \frac{a_{ij}W_j}{W_i} Y_i \quad (2.41)$$

a conservation equation without chemical source term can be derived using Eq. (2.6).

W_i denotes the molecular weight of species i and a_{ij} is the number of atoms of element j in a molecule of species i and W_j is the molecular weight of that atom.

Introducing the definition of the operator \mathcal{L}

$$\mathcal{L} = \rho \frac{\partial}{\partial t} + \rho \mathbf{v} \cdot \nabla - \nabla(\rho D_Z \nabla) \quad (2.42)$$

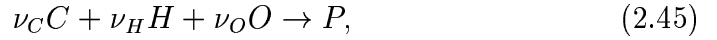
then yields

$$\mathcal{L}(Z_j) = -\nabla \left(\sum_j^{n_s} \frac{a_{ij}W_j}{W_i} (\rho D_Z \nabla Y_i + \mathbf{j}_i) \right) + \sum_i^{n_s} \frac{a_{ij}W_j}{W_i} \omega_i. \quad (2.43)$$

The last term on the right hand side represents the chemical production rate of element j . It is equal to zero, since chemical elements are neither produced nor consumed by chemical reactions among chemical species. If the molecular diffusion \mathbf{j}_i is given by Eq. (2.8) Fick's first law of binary diffusion and the diffusivities of the chemical species are all equal to D_Z , then the first term on the right hand side of Eq. (2.43) also cancels and it results

$$\mathcal{L}(Z_j) = 0. \quad (2.44)$$

For a global reaction among the chemical elements C, H and O with the reaction rate ω



where ν_j is the number of atoms of element j present in the mixture, a coupling function can be derived by applying Eq. (2.43) to each element j .

$$\mathcal{L}(Z_j) = -\nu_j W_j \omega. \quad (2.46)$$

When $\mathcal{L}(Z_C)$ and $\mathcal{L}(Z_H)$ are added and the chemical source term is eliminated using $\mathcal{L}(Z_O)$, the following relation is obtained

$$\mathcal{L}(\beta) \equiv \mathcal{L}\left(\frac{Z_C}{\nu_C W_C} + \frac{Z_H}{\nu_H W_H} - 2\frac{Z_O}{\nu_O W_O}\right) = 0. \quad (2.47)$$

Inserting the coupling function β into Eq. (2.40)

$$Z = \frac{Z_C/(\nu_C W_C) + Z_H/(\nu_H W_H) + 2(Z_{O,2} - Z_O)/(\nu_O W_O)}{Z_{C,1}/(\nu_C W_C) + Z_{H,1}/(\nu_H W_H) + 2Z_{O,2}/(\nu_O W_O)} \quad (2.48)$$

yields the mixture fraction Z . Here the fuel stream is denoted with the index 1 and the oxidizer stream with the index 2. For the transport equation of the mixture fraction, it follows under the assumption of equal diffusivities of all components:

$$\mathcal{L}(Z) = 0. \quad (2.49)$$

From Eq. (2.48), with the condition that the mass fractions of the reactants are zero, the stoichiometric mixture fraction is obtained as

$$Z_{st} = \frac{2Z_{O,2}/(\nu_O W_O)}{Z_{C,1}/(\nu_C W_C) + Z_{H,1}/(\nu_H W_H) + 2Z_{O,2}/(\nu_O W_O)}. \quad (2.50)$$

Since the mixture fraction represents a non reactive scalar and then a transport equation for this scalar in the physical space contains no chemical source

term, the classical assumptions for the turbulence modelling for non reactive scalars can be applied. By use of the Ansatz of the Presumed Shape Pdf, which will be described in section 2.4.1, the Pdf of the mixture fraction can be established. The required transport equations for the mean value and the variance of the mixture fraction are solved in the CFD-code. If the distribution of the Pdf of the mixture fraction is known, the probability to come across the reaction zone at a location \mathbf{x} at the time t in the flow field can be determined. After solving the flamelet equations, which will be described in the next section, turbulent mean values for the mass fractions of the chemical species Y_i can be calculated thanks to the Pdf.

2.3.2 Flamelet Equations

The laminar flamelet equations based on the mixture fraction as independent variable for steady state formulation have been derived independently by Peters in 1980 [63] and Kuznetsov in 1982 [47]. The unsteady formulation has been given by Peters in 1984 [64] and reviewed in 1986 [65]. This derivation is based on a local coordinate transformation and boundary layer arguments.

The combustion processes take mainly place in the vicinity of the surface where the mixture fraction is stoichiometric. Figure 2.3.2 represents the development of this surface by entrainment of the surrounding oxidizer in the fuel stream. The position of this surface where the mixture fraction has the value of stoichiometric mixture, that is to say $Z(\mathbf{x}, t) = Z_{st}$, can be described by a field equation inserting the operator \mathcal{L} given by Eq. (2.42) and the mixture fraction Z into Eq. (2.49):

$$\rho \frac{\partial Z}{\partial t} + \rho \mathbf{v} \cdot \nabla Z - \nabla(\rho D_Z \nabla Z) = 0. \quad (2.51)$$

A coordinate system is introduced, where one coordinate x_1 , which is to be replaced by the new coordinate Z , is locally normal to the isosurface of the stoichiometric mixture fraction, whereas the other two coordinates x_2 and x_3 are tangential to this isosurface. Using $Z_2 = x_2$, $Z_3 = x_3$, and $\tau = t$ as the

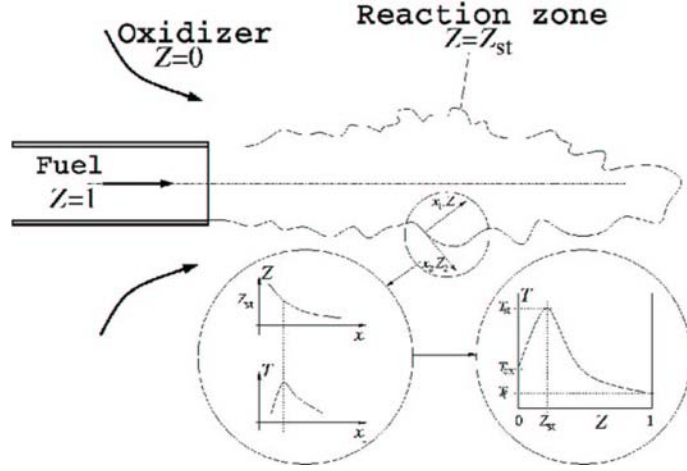


Figure 2.1: Mixing of the fuel and oxidizer in the reaction zone.

other independent variables the transformation rules are given as

$$\begin{aligned}\frac{\partial}{\partial t} &= \frac{\partial}{\partial \tau} + \frac{\partial Z}{\partial t} \frac{\partial}{\partial Z} \\ \frac{\partial}{\partial x_1} &= \frac{\partial}{\partial x_1} \frac{\partial}{\partial Z} \\ \frac{\partial}{\partial x_\beta} &= \frac{\partial}{\partial Z_\beta} + \frac{\partial Z}{\partial x_\beta} \frac{\partial}{\partial Z}, \quad \beta = 2, 3.\end{aligned}\tag{2.52}$$

Application of these transformation rules to Eqs. (2.6) and (2.14) and an asymptotic analysis of the resulting equations, where only leading order terms are retained, yields the flamelet equations for temperature

$$\begin{aligned}\rho \frac{\partial T}{\partial t} - \rho \frac{\chi}{2} \frac{\partial^2 T}{\partial Z^2} - \rho \frac{\chi}{2c_p} \left[\sum_i^{n_s} \frac{C_{p_i}}{Le_i} \frac{\partial Y_i}{\partial Z} + \frac{\partial c_p}{\partial Z} \right] \frac{\partial T}{\partial Z} \\ + \frac{1}{c_p} \left[\sum_i^{n_s} w_i h_i - \frac{\partial p}{\partial t} - \dot{q}_r \right] = 0,\end{aligned}\tag{2.53}$$

and species conservation

$$\rho \frac{\partial Y_i}{\partial t} - \rho \frac{\chi}{2Le_i} \frac{\partial^2 Y_i}{\partial Z^2} - \omega_i = 0.\tag{2.54}$$

In these equations n_s denotes the number of chemical species, c_{p_i} , ω_i , h_i , \dot{q}_r , Le_i are respectively the heat capacities at constant pressure, the chemical

rates, the enthalpies of the chemical species i , the radiative heat loss and the Lewis number of species i . The chemical source term ω_i in Eq. (2.54) and the radiative heat loss term \dot{q}_r in Eq. (2.53) are described in section 2.3.3. The Lewis numbers Le_i in Eqs. (2.53) and (2.54) have formally to be unity for the above given derivation. Furthermore, if a simple diffusion model like the binary diffusion model is used, the requirement that the sum of the diffusive fluxes adds to zero is violated. Pitsch et al. [74] have derived flamelet equations that account for differential diffusion and use a more accurate model for the diffusion fluxes which ensures that the requirement formulated above is fulfilled. Differential diffusion is the strongest in laminar hydrogen flames, because of the large deviation from unity of the Lewis number of hydrogen. For hydrocarbon fuels these effects are not so strong.

Another more general derivation of the flamelet equations is given by Peters (2000) [68]. This derivation is based on a two scale asymptotic expansion similar to that used by Keller and Peters [42]. The non-reactive scalar fields outside of the instantaneous reactive-diffusive structure is analysed by considering filtered fields of the reactive scalars and the mixture fraction. Introducing the normalized thickness of the diffusive layers in the vicinity of the flame surface as a small parameter in an asymptotic formulation, the filtered reactive scalars are then related to the filtered mixture fraction by a similar equation as in the flamelet equations, except that the chemical source term is missing. The one-dimensional equations for the non-reactive outer fields can be matched to the flamelet equations valid in the thin layer. This leads to one-dimensional equations in terms of Z in the entire domain.

The characteristic of Eqs. (2.53) and (2.54) is that the convective terms have disappeared after the transformation into mixture fraction space. Since all scalars are convected with the same velocity in physical space no relative convective velocities exist between the mixture fraction and the other scalars such as species mass fractions or temperature.

The coupling of the equations in mixture fraction space to the flow field in physical space occurs through the term $\partial p / \partial t$ and a particular parameter, the scalar dissipation rate defined by

$$\chi = 2D_Z(\nabla Z)^2. \quad (2.55)$$

The scalar dissipation rate represents instantaneous molecular diffusion and strain effects by the flow field [64] on the small length scales. The flamelet

model provides information of the flame structure on the smallest scales, which was lost by the Favre averaging. This is a great improvement compared to, for instance, the eddy dissipation models that lacks this information. The pdf methods can be applied in conjunction with the flamelet model. It reduces the dimensionality of the pdf dramatically, because only one scalar, the mixture fraction, is necessary to describe the composition.

2.3.3 Flamelet Parameters

As mentioned in the previous section, the coupling of the flamelet equations in mixture fraction space to the flow field in physical space occurs through the so-called flamelet parameters. These parameters that have to be modeled in Eqs. (2.53) and (2.54) are the pressure p and the scalar dissipation rate χ . In most low Mach number applications the pressure can be assumed to be spatially constant and therefore does not have to be described as a function of the mixture fraction. The Z -dependence of the scalar dissipation rate χ is taken from [64]

$$\chi(Z) = \frac{a_s}{\pi} \exp(-2[\operatorname{erfc}^{-1}(2Z)]^2) = \frac{a_s}{\pi} f_{\operatorname{erfc}}(Z). \quad (2.56)$$

With the assumption that this formulation is also valid for the conditional mean scalar dissipation rate, χ can be expressed in the flamelet equations by means of the formulation of the probability density function Pdf on χ_{st} with the Dirac delta function

$$f_{\chi_{st}}(\chi) = \delta(\chi_{st} - \chi) \quad (2.57)$$

as

$$\chi = \tilde{\chi}(Z, \mathbf{x}, t) = \tilde{\chi}_{st}(\mathbf{x}, t) \frac{f_{\operatorname{erfc}}(Z)}{f_{\operatorname{erfc}}(Z_{st})}. \quad (2.58)$$

The turbulent mean value of the scalar dissipation rate $\tilde{\chi}$ is modeled as (see Jones [41])

$$\tilde{\chi} = c_\chi \frac{\tilde{\epsilon}}{k} \widetilde{Z''^2}, \quad (2.59)$$

where $c_\chi = 2.0$.

Consequently the scalar dissipation rate is determined from the fluctuating variables χ_{st} and Z . If the statistical independence of these variables

is assumed, the turbulent mean value of the scalar dissipation rate can be calculated with

$$\tilde{\chi} = \int_{\chi'_{st}} \chi'_{st} \tilde{P}(\chi'_{st}) d\chi'_{st} \int_Z f(Z) \tilde{P}(Z) dZ. \quad (2.60)$$

The first integral in Eq. (2.60) represents the mean value of the scalar dissipation rate conditioned on Z_{st}

$$\tilde{\chi}_{st} = \sum_{\chi_{st}} \chi'_{st} \tilde{P}(\chi'_{st}) d\chi'_{st}. \quad (2.61)$$

According to Hellström [31] $\tilde{\chi}_{st}$ can be determined by equating the right hand side of Eq. (2.60) with the common formulation for the turbulent mean value of the scalar dissipation rate from Eq. (2.59) as

$$\tilde{\chi}_{st} = \frac{c_{\chi} \tilde{\epsilon} \widetilde{Z''^2}}{\int_0^1 \frac{Z^2}{Z_{st}^2} \frac{f_{erfc}(Z)}{f_{erfc}(Z_{st})} \tilde{P}(Z) dZ}. \quad (2.62)$$

Alternatively, the mixture fraction dependency can be specified similarly to Eq. (2.58) according to [69] with the following relation:

$$\chi = \tilde{\chi}(Z, \mathbf{x}, t) = \tilde{\chi}_{st}(\mathbf{x}, t) \frac{\ln Z}{\ln Z_{st}}. \quad (2.63)$$

With this modified form, Eq. (2.62) becomes

$$\tilde{\chi}_{st} = \frac{c_{\chi} \tilde{\epsilon} \widetilde{Z''^2}}{\int_0^1 \frac{Z^2}{Z_{st}^2} \frac{\ln Z}{\ln Z_{st}} \tilde{P}(Z) dZ}. \quad (2.64)$$

In CFD calculations, this variable is calculated for each cell and averaged over the considered physical space. The obtained mean value of the domain for the conditional scalar dissipation rate $\widehat{\chi_{st}}$ is weighted with the surface of the stoichiometric mixture per unit volume. Following [69] $\widehat{\chi_{st}}$ can be determined from this equation:

$$\widehat{\chi_{st}} = \frac{\int_V \bar{\rho}(\mathbf{x}) \tilde{\chi}_{st}^{3/2}(\mathbf{x}) \tilde{P}(Z_{st}) dV'}{\int_V \bar{\rho}(\mathbf{x}) \tilde{\chi}_{st}^{1/2}(\mathbf{x}) \tilde{P}(Z_{st}) dV'}. \quad (2.65)$$

The turbulent mean values of the mass fractions of the chemical species Y_i needed in the CFD code are determined for each time step with the help of a Pdf integration and the distribution of the species mass fractions in the mixture fraction space from the solution of the unsteady flamelets $Y_i(Z, \chi_{st})$. The procedure to evaluate the turbulent mean values and the numerical implementation will be explained in chapter 3.

Chemistry

The chemical source term is defined by the chemical elementary reactions

$$\omega_i = W_i \sum_{ir_1}^{n_r} (\nu''_{i,ir} - \nu'_{i,ir}) k_{ir} \prod_{j=1}^{n_s} c_j^{\nu'_{j,ir}}, \quad (2.66)$$

where W_i is the molecular weight of species i , n_r is the number of elementary reactions, $\nu''_{i,ir}$, $\nu'_{i,ir}$ are the stoichiometric coefficients of species i in reaction ir , and c_j is the concentration of species j . The reaction rate k_{ir} is given in Arrhenius form

$$k_{ir} = A_{ir} T^{n_{ir}} \exp \left[-\frac{E_{ir}}{R_{gas} T} \right], \quad (2.67)$$

where R_{gas} is the universal gas constant. The frequency factors A_{ir} , the temperature exponents n_{ir} and the activation energies E_{ir} are given in Appendix A.

Radiation in hydrocarbon flames is mainly due to two sources:

- Radiation of gases strongly depends on the wave length. They only emit and absorb in small ranges. H_2 , O_2 and N_2 are transmissive over the whole spectrum, whereas CO_2 , H_2O and hydrocarbons absorb in the infrared spectrum. Since hydrocarbons in most cases do not appear in high temperature regions it is sufficient to account for radiation of CO_2 and H_2O .
- Another source are soot particles. Soot is not considered in this work.

Assuming an optically thin gas the absorption can be neglected. Then only emission has to be taken into account. Following Stefan-Boltzmann [11] and

applying Kirchhoff's law, the radiation of a gray body can be derived

$$\dot{q}_r = 4\alpha_p\sigma_s T^4, \quad (2.68)$$

where $\sigma_s = 5.669 \cdot 10^{-8} \text{ W}/(\text{m}^2\text{K}^5)$ is the Stefan-Boltzmann constant and α_p is Planck's radiation coefficient defined by

$$\alpha_p = \alpha_{p,\text{CO}_2} p_{\text{CO}_2} + \alpha_{p,\text{H}_2\text{O}} p_{\text{H}_2\text{O}}, \quad (2.69)$$

with p_{CO_2} and $p_{\text{H}_2\text{O}}$ representing the partial pressures of CO_2 and H_2O . The coefficients α_{p,CO_2} and $\alpha_{p,\text{H}_2\text{O}}$ are taken from Müller [60]. The resulting heat loss term is then given by

$$\dot{q}_r = 4\sigma_s T^4 (\alpha_{p,\text{CO}_2} p_{\text{CO}_2} + \alpha_{p,\text{H}_2\text{O}} p_{\text{H}_2\text{O}}). \quad (2.70)$$

2.4 The Representative Interactive Flamelet (RIF) Model

The solution of the flamelet equations gives the distribution of the species mass fractions Y_i in the mixture fraction space. For the determination of the spatial distribution of the species, the so-called Presumed Shape Pdf ansatz is used. The distribution of the Pdf is supposed as known and will be explained in section 2.4.1. If the flamelets are solved steadily, the flamelet profiles can be calculated in advance and saved in adapted libraries. The allocation of the values in the libraries occurs via the flamelet parameters defined in section 3.2.1. Pressure and temperature follow the considered physical problem at the boundaries of the mixture fraction space and the chemical composition of the fuel and oxidizer stream is known at the beginning. The scalar dissipation rate is a changing parameter, that represents the dynamical influences of the flow. The evolution of the scalar dissipation rate is discussed as a particular flamelet parameter in section 2.4.2.

2.4.1 Presumed Shape Pdf Ansatz

When using this ansatz the distribution of an appropriate probability density function (Pdf) with two parameters is assumed to be known. This distribution was determined by Jones [41] by means of experimental data. Then the functional correlation of the Pdf depending on both parameters \tilde{Z} and \tilde{Z}''^2

can be established at each location of the flow field. Corresponding transport equations are solved for these parameters in the CFD code.

In a system with two inlet streams the mixture fraction Z varies between 0 and 1. That is why the β -function Pdf is often used to determine the Favre Pdf in simulation of turbulent non-premixed combustion. The β -function Pdf or β -Pdf has the following form:

$$\tilde{P}(Z; \mathbf{x}, t) = \frac{Z^{\alpha-1}(1-Z)^{\beta-1}\Gamma(\alpha+\beta)}{\Gamma(\alpha)\Gamma(\beta)} \quad (2.71)$$

In Eq. (2.71) Γ describes the gamma function. Both parameters α and β can be determined from the following relations for the Favre averaged values of the mixture fraction $\tilde{Z}(\mathbf{x}, t)$ and the variance of the mixture fraction $\widetilde{Z''^2}(\mathbf{x}, t)$:

$$\alpha = \tilde{Z}\gamma, \quad \beta = (1 - \tilde{Z})\gamma, \quad (2.72)$$

where γ is given as a function of $\tilde{Z}(\mathbf{x}, t)$ and $\widetilde{Z''^2}(\mathbf{x}, t)$:

$$\gamma = \frac{\tilde{Z}(1 - \tilde{Z})}{\widetilde{Z''^2}} - 1 \geq 0. \quad (2.73)$$

The β -Pdf is shown in Figure 2.4.1 as a function of Z for different combinations of the parameters \tilde{Z} and γ . For a very small variance of the mixture fraction $\widetilde{Z''^2}$ (large γ) the β -Pdf draws near the Gauss distribution. A singularity is formed at $Z = 0$ for $\alpha < 1$ and at $Z = 1$ for $\beta < 1$.

The profile of this Pdf is fixed by the turbulent mean value \tilde{Z} and the variance of the mixture fraction $\widetilde{Z''^2}$. Their spatial distribution is determined by

$$\frac{\partial(\bar{\rho}\tilde{Z})}{\partial t} + \nabla \cdot (\bar{\rho}\tilde{\mathbf{v}}\tilde{Z}) = \nabla \cdot \left[\frac{\mu_t}{Sc_{\tilde{Z}}} \nabla \tilde{Z} \right] \quad (2.74)$$

and

$$\frac{\partial(\bar{\rho}\widetilde{Z''^2})}{\partial t} + \nabla \cdot (\bar{\rho}\tilde{\mathbf{v}}\widetilde{Z''^2}) = \nabla \cdot \left[\frac{\mu_t}{Sc_{\widetilde{Z''^2}}} \nabla \widetilde{Z''^2} \right] + \frac{2\mu_t}{Sc_{\widetilde{Z''^2}}} (\nabla \tilde{Z})^2 - \bar{\rho}\tilde{\chi}. \quad (2.75)$$

Additional transport equations for these variables are solved in the CFD code. In these equations μ_t denotes the turbulent dynamic viscosity. For the turbulent Schmidt number $Sc_{\tilde{Z}}$ and $Sc_{\widetilde{Z''^2}}$ a constant value of 0.7 is mostly

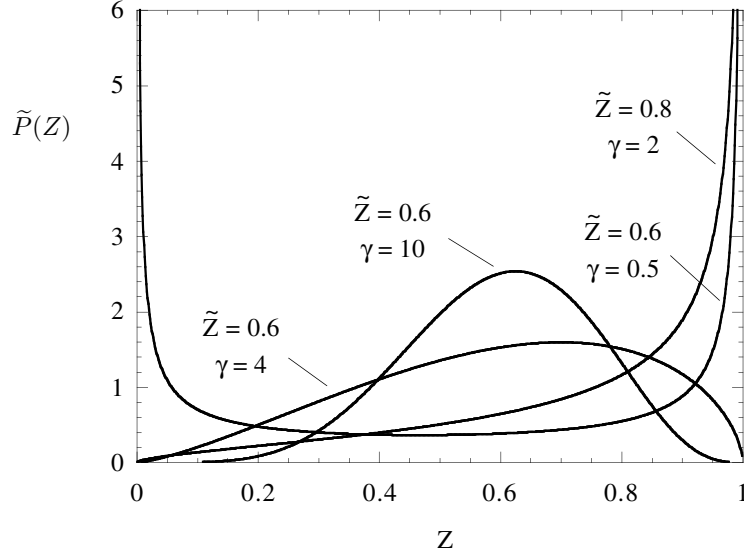


Figure 2.2: Profiles of the β -Pdf of different values of \tilde{Z} and γ .

chosen [25]. The energy conservation was integrated in the form of a modified equation for the turbulent mean value of the total enthalpy \tilde{h} in the CFD code:

$$\frac{\partial(\bar{\rho}\tilde{h})}{\partial t} + \nabla \cdot (\bar{\rho}\mathbf{v}\tilde{h}) = \frac{D\tilde{p}}{Dt} - \nabla \cdot \mathbf{j}_q + \bar{\rho}\tilde{\epsilon} + \dot{q}_r. \quad (2.76)$$

2.4.2 Temporal Change of the Flamelet Parameter

The influence of the temporal change of the scalar dissipation rate on the flamelet solution was investigated with numerical analysis of the flamelet equations [4, 55]. With a rapid change of χ , a steady solution slowly appears again, so that consecutive changes of the flamelet parameters cannot be reproduced with the help of steady flamelets. Especially when considering chemical processes such as ignition, extinction of pollutant formation, unsteady effects have to be taken into account.

Chemical time scales for the formation of the NO_x are significantly larger than those of the main combustion reactions, which are responsible for the heat release. When the flamelet parameters change with the time, the pollutant formation occurs comparatively slowly, whereas the combustion reac-

tions adapt themselves very fast to the modified conditions. This requires the use of an unsteady flamelet model, where the scalar dissipation rate represents the effects of the turbulent flow and mixing field inside the flamelet equations.

Local and temporal changes of the scalar dissipation rate along the path of the considered fluid particle influence the individual rates of pollutant formation. If this fluid particle is represented by a flamelet, it follows the dependence of the time and spatial solution of the flamelet on the path itself through the flow field. Because of the strong temperature diminution normal to the thin reaction zone and the high activation energy, these die down outside the reaction zone.

These models, together with the Eulerian Particle Flamelet Model presented in the next chapter, are used to perform the numerical simulation of a *FLOX*[®] combustor and to simulate the coal combustion in a pressurised pulverized coal combustion facility. The results are presented in chapter 5.

Chapter 3

Numerical Implementation

The numerical implementation occurs by using an interactive flamelet model, as described in section 2.4. The results presented in this work were obtained using the RIF code version 3.7 together with the CFD Code FLUENT (version 6.2). The CFD code is used to calculate the flow field. To simulate the turbulent reacting flow an extended version based on the CFD code is applied. The solver and the applied models are described in detail in the FLUENT Manual [1]. In the following the main properties as well as the extensions for the coupling with the RIF code developed at the Institut für Technische Verbrennung will be explained. Considering the equations to solve and the coupling of the CFD code and the RIF code, the numerical procedure of the unsteady calculations will be pointed up.

3.1 CFD code

With the implicit solver in sequential form first the momentum equations with pressure correction are solved. The coupling of the equations for the pressure, the momentum and the energy occurs via the SIMPLE algorithm [62]. Subsequently the equations for the scalars are solved. When using the RIF model the energy equation has a particular significance. Indeed this is implemented as an enthalpy equation under the modified form of the total enthalpy via user defined functions (udf). Therefore no chemical source terms appear and the temperature can be determined from the definition of the enthalpy when the species distribution is known. The steady solution of the flow and temperature field is calculated beforehand with simple combustion

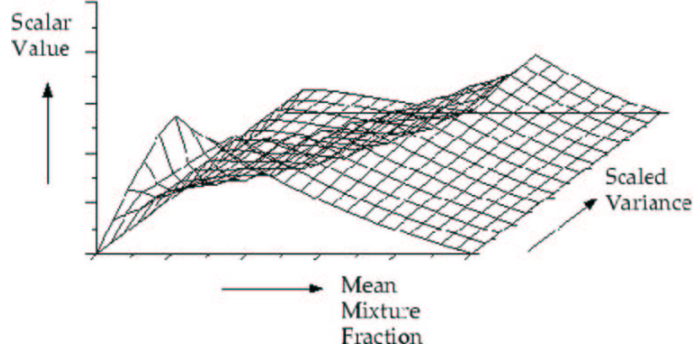


Figure 3.1: Look-Up Table for a scalar Φ as a function of the mean value and the variance of the mixture fraction in an adiabatic system.

models thanks to the ansatz of the pdf-mixture fraction integrated in the CFD code FLUENT. This will be presented in the following section. To describe the turbulence, the standard $\tilde{k}, \tilde{\epsilon}$ turbulence model is used.

3.1.1 Ansatz of the Pdf-mixture fraction

If the values of the species mass fractions Y_i , density ρ or temperature T are calculated as a function of the mean value and the variance of the mixture fraction by means of a preprocessor, turbulent mean values for these scalars can be determined in the CFD code FLUENT via so-called Look-Up Tables with the help of the Pdf integration presented in the section 2.4.1. In adiabatic systems, in which the instantaneous enthalpy is simply a function of the instantaneous mixture fraction, the scalars are readable from a two-dimensional Look-Up Table. An example is shown in Fig. 3.1. The parameters of the tabulation are the mixture fraction and the variance of the mixture fraction. The variance of the mixture fraction $\widetilde{Z''^2}$ is scaled with the maximal value of the variance:

$$\widetilde{Z''^2}_s = \frac{\widetilde{Z''^2}}{0.25\tilde{Z}(1 - \tilde{Z})}. \quad (3.1)$$

To produce the Look-Up Tables the preprocessor prePDF in FLUENT [1] is used. With this preprocessor the transformation of reactants into products for the non-premixed combustion is calculated with the methods described in section 3.1.2 and 3.1.3 or with the help of steady flamelets, however, that

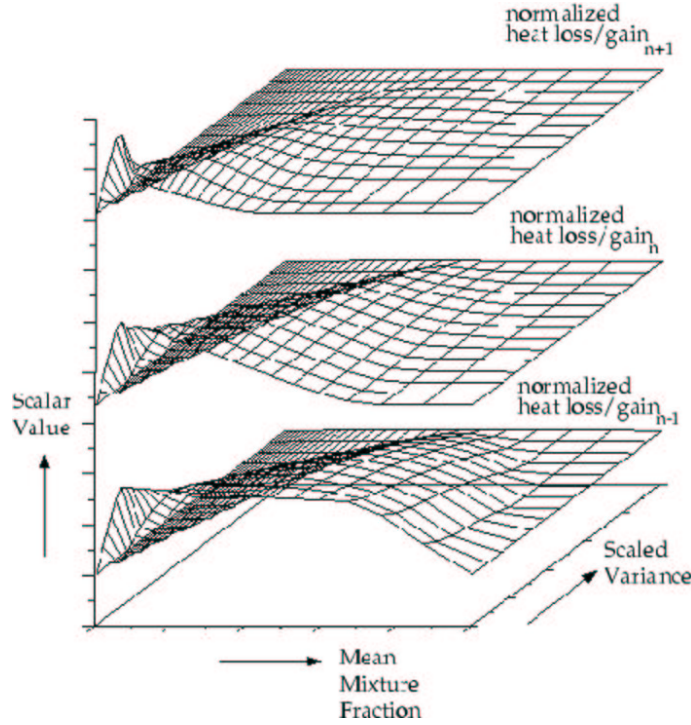


Figure 3.2: Three-dimensional Look-Up Table for a scalar Φ as a function of the mean value and the variance of the mixture fraction as well as the normalized heat fluxes in a non-adiabatic system.

are not applied here.

In non-adiabatic systems the enthalpy is not a linear function of the mixture fraction. Moreover, the heat loss via wall heat flux and radiation have to be taken into account. That is why a Look-Up Table is needed for each enthalpy value. It results a three-dimensional Look-Up Table, as shown in Fig. 3.2. Each plane in a such 3D-Look-Up Table corresponds to a normalized heat loss or gain. The lowest plane corresponds to the maximal heat loss, so that all entries are available at the minimal temperature defined in the problem. The highest plane represents the maximum heat gain. Therefore all entries are available at the temperature defined as the maximum value. The planes without heat loss or gain correspond to adiabatic conditions. The values for the scalars can then be interpolated thanks to the normalized heat transfer. This method is used in the calculations presented in Chapter 5.

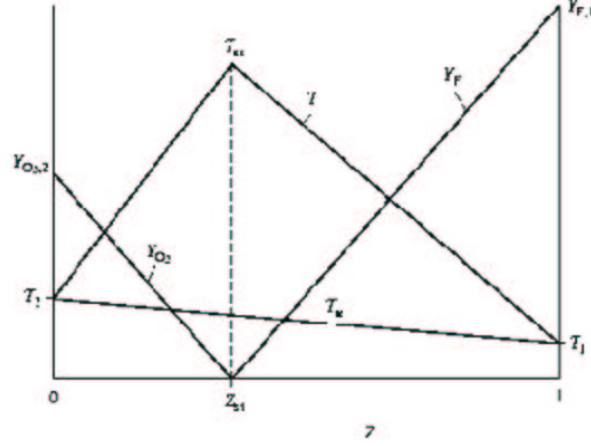


Figure 3.3: Burke-Schumann solution as function of the mixture fraction.

3.1.2 Burke-Schumann solution

With the assumption that the chemical transformation of reactants into products runs infinitely fast, the combustion can be described by an irreversible one-step reaction. The mass fractions of the chemical species Y_i can be directly determined from the stoichiometry of the reaction. The reaction rates of the part reaction or information about the chemical equilibrium are not necessary. In the limit of the infinitely fast irreversible one-step reaction, there exists according to [17] an infinitely thin surface of chemical nonequilibrium at $Z = Z_{st}$. Outside this surface the mass fractions of the fuel and oxidizer are either zero or they can be presented by linear functions of Z . For the mass fractions of the products corresponding dependencies can then be derived. Under certain requirements the temperature T can be expressed piecewise as a linear function of Z too, as plotted in Fig. 3.3. Since for an idealised form of the consideration of the chemical processes the complete transformation to products occurs at the moment of the mixture of fuel and oxidizer, this model is also described by the term "Mixed is Burned". In the unburnt state (subscript $_u$) the mass fractions of fuel and oxidizer as well as the temperature can be represented as a well-defined function of the mixture fraction if the diffusivity of all involved species is supposed to be the same. Because of the consideration of the kinetics in form of a one-step reaction

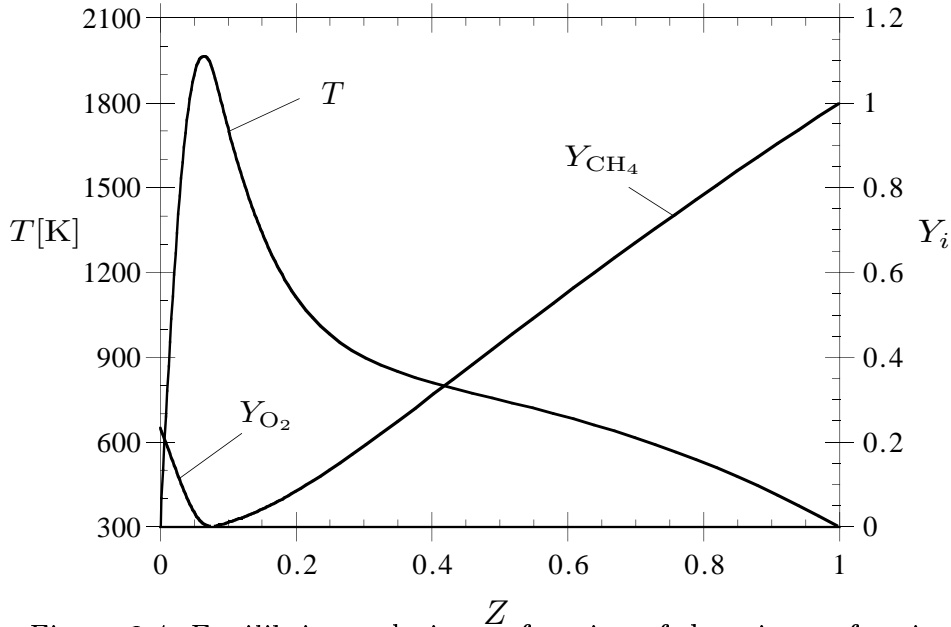


Figure 3.4: Equilibrium solution as function of the mixture fraction.

formation and dissociation effects of intermediate products are nevertheless neglected, so that no information about the mass fraction of the intermediate products is obtained. Furthermore the maximal temperature, especially in the domain of stoichiometric mixture, is most of the time overpredicted. That is the reason why the Burke-Schumann solution is not used in this work.

3.1.3 Chemical equilibrium

If the reactions are infinitely fast but also reversible (on the contrary of the Burke-Schumann solution), all species are in chemical equilibrium for each value of the mixture fraction. The species mole fractions X_i can be determined as a function of the mixture fraction Z by the means of an algorithm based on the minimisation of the Gibbs free energy [46]. All chemical species considered in the combustion and also all intermediate products are included, without needing the detailed chemical production rates. With the linear relation between enthalpy and mixture fraction when neglecting the loss terms in the mixture fraction space, the calculated equilibrium temperature corresponds to the adiabatic flame temperature for each value of the mixture fraction. This equilibrium solution is represented in Fig. 3.4. The main

disadvantage of this ansatz is the neglect of non-equilibrium effects. Since all chemical species corresponding to the mixture in chemical equilibrium are available, pollutants, with a slower formation rate than the main species, can not be correctly determined. The necessary considerations of unsteady effects needs, on top of the consideration of a detailed chemistry, also the consideration of the time-dependent processes during the combustion. However, the method of the chemical equilibrium is suitable when calculating the species involved in the heat release and therewith the spatial temperature distribution and the distribution of the significant species.

3.2 Coupling of the CFD and the RIF-Codes

In order to determine the parameters required for the solution of the flamelet equations as well as the mean species mass fractions from the flamelet solutions, additional equations are needed in the CFD code. An interface for the linking of own routines is necessary. It is provided in FLUENT by the user defined functions (udf).

Via udf equations for the turbulent mean value and the variance of the mixture fraction are implemented, as well as transport equations for the probability \tilde{I}_l to find a flamelet l . With a user defined function, which enables the access to external programs, the flamelet code RIF 3.7 is called. The flamelet code delivers at each time step of the flow simulation the solution of the flamelet equation in the mixture fraction space. The coupling of both codes is shown schematically in Fig. 3.5. After calculating one time step, the flamelet parameters are provided by the CFD code FLUENT. These are the scalar dissipation rate averaged on the domain $\widehat{\chi_{st}}$, conditioned on the stoichiometric mixture Z_{st} , the mean pressure \tilde{p} and the lowest and the highest limit values for the mixture fraction, Z_l resp. Z_r and the corresponding boundary conditions. These are normally the temperature and the chemical composition for $Z_l = 0$ and $Z_r = 1$ (Z on the left resp. right hand side of the domain).

3.2.1 Supply of the Flamelet Parameters

The scalar dissipation rate averaged over the entire domain is determined according to [72], where the surface integrals are transformed into volume integrals. Additionally the terms with the probability \tilde{I}_l to find a flamelet l

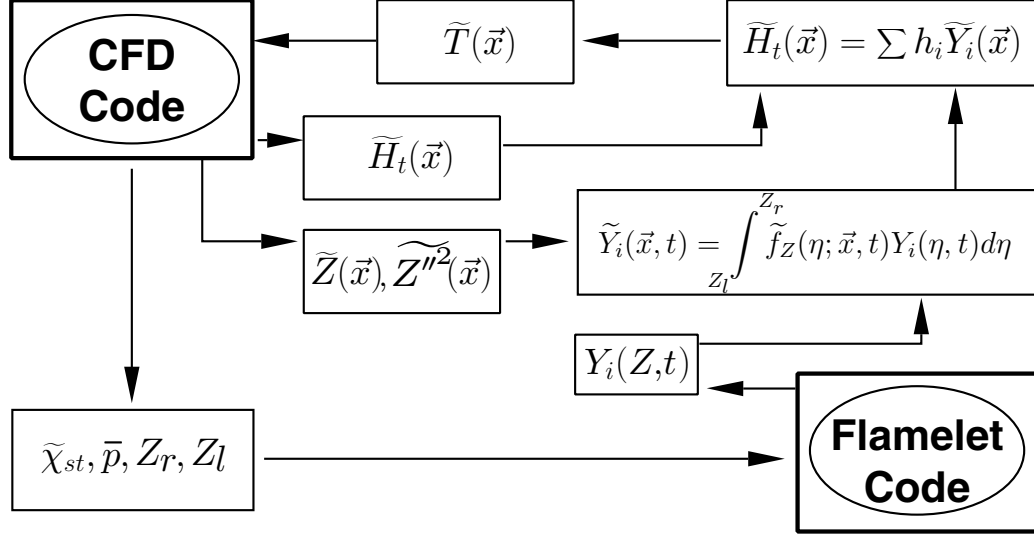


Figure 3.5: Coupling of the CFD code FLUENT and the flamelet code RIF.

are weighted. It follows the extended equation (2.65):

$$\widehat{\chi_{st}}(l) = \frac{\int_V \tilde{I}_l(\mathbf{x}) \bar{\rho}(\mathbf{x}) \tilde{\chi}_{st}^{3/2}(\mathbf{x}) \tilde{P}(Z_{st}) dV'}{\int_V \tilde{I}_l(\mathbf{x}) \bar{\rho}(\mathbf{x}) \tilde{\chi}_{st}^{1/2}(\mathbf{x}) \tilde{P}(Z_{st}) dV'}. \quad (3.2)$$

The scalar dissipation rate conditioned on the stoichiometric mixture $\tilde{\chi}_{st}$ given in the previous equation is determined as follows:

$$\tilde{\chi}_{st} = \frac{\tilde{\chi}(\tilde{Z})}{\int_0^1 \frac{Z^2}{Z_{st}^2} \frac{\ln Z}{\ln Z_{st}} \tilde{P}(Z) dZ}. \quad (3.3)$$

For each time step the flamelet equations are solved in the RIF code to supply the species mass fractions and the temperature as function of the mixture fraction and time. To determine the local turbulent mean values in the CFD code at the time t starting from the instantaneous species mass fractions, a Pdf integration is applied. Assuming that the mixture fraction dependence of the scalar dissipation rate is represented by Eq. (2.58), the flamelet solutions can be described with

$$Y_i = Y_i(Z, \chi_{st}). \quad (3.4)$$

The turbulent mean values of the mass fractions of the chemical species Y_i can be generally determined with the Pdf integration of the form

$$\tilde{Y}_i = \int_0^\infty \int_0^1 Y_i(Z) \tilde{P}(Z, \chi) dZ d\chi \quad (3.5)$$

and with Eq. (3.4) from the relation

$$\tilde{Y}_i = \int_0^\infty \int_0^1 Y_i(Z, \chi_{st}) \tilde{P}(Z, \chi_{st}) dZ d\chi_{st}. \quad (3.6)$$

The Pdf for the determination of Favre averaged values

$$\tilde{P}(Z, \chi_{st}) = \frac{\rho P(Z, \chi_{st})}{\bar{\rho}} \quad (3.7)$$

is the combined Pdf of Z and χ_{st} . This can be represented by

$$\tilde{P}(Z, \chi_{st}) = P(\chi_{st}|Z) \tilde{P}(Z) \quad (3.8)$$

with the conditioned Pdf of the scalar dissipation rate $P(\chi_{st}|Z)$ or with the assumption that χ_{st} and Z are statistically independent as

$$\tilde{P}(Z, \chi_{st}) = \tilde{P}(\chi_{st}) \tilde{P}(Z). \quad (3.9)$$

It can be assumed for example according to [52] for $\tilde{P}(Z)$ a logarithmic normal distribution with a variance of $\sigma = 1$ [24].

The functional correlation $Y_i(Z, \chi_{st})$ needed for the interpretation of Eq. (3.6) is given by the solution of the unsteady flamelets. Finally the relation for the mass fractions of the chemical species follows:

$$\tilde{Y}_i = \int_0^1 Y_i(Z, \widehat{\chi_{st}}) \tilde{P}(Z) dZ. \quad (3.10)$$

With the help of the so-called β -Pdf [52], which requires the mean value and the variance of the mixture fraction as function of the position in the CFD code as parameters, the mean species mass fractions for the current time step are calculated.

Starting from the turbulent mean values of the chemical species \tilde{Y}_i the temperature can be calculated using a Newton iteration from the definition of the total enthalpy

$$\tilde{h} = \sum_{i=1}^{n_s} \tilde{Y}_i h_i(\tilde{T}), \quad (3.11)$$

since its spatial distribution in the CFD code can be determined with the help of the additional transport equation (2.76). If the RIF model is applied interactive, a new density field for the current time step in the CFD code is obtained, and the resulting modifications require a new calculation of the flow field. Since the flow and temperature fields are calculated beforehand in the procedure applied here thanks to the combustion models available in the CFD code and only the pollutant distributions and emissions should be determined, the density field is kept constant, and only the unsteady modification of the flamelet distribution is updated.

3.3 The Eulerian Particle Flamelet Model

The pollutant formation during the combustion begins when a fluid particle passes the flame front in a turbulent steady diffusion flame. The chemical time scales for NO_x and soot are longer than those of the combustion reactions, which are responsible for the heat release. Whereas these reactions adapt themselves very fast to the local conditions, the pollutant formation proceeds slowly. That is why the use of unsteady flamelets is necessary. These were first applied by Mauss et al [56] for the simulation of ignition and quenching phenomena in turbulent free jet diffusion flames and for the numerical simulation of Diesel engines [5, 30, 70].

When using unsteady flamelets, the scalar dissipation rate represents the turbulence and mixture influences on the combustion and the modification of this parameter along the path of a fluid particle through the flow field influences the pollutant formation. The fluid particle is represented by a flamelet in this procedure. The development of the solution for this flamelet is dependent of the path covered by the fluid particle in the flow field. Under the assumption that different fluid particles cover statistically different paths through the flow field and thus experience different modifications of the flamelet parameter along the covered path, the use of many flamelets is wise.

The statistical path of the fluid particle is described by the Eulerian transport equations for the mass fraction of the particle at position \mathbf{x} . Next to the transport equations of the CFD code, transport equations for the probability $\tilde{I}_l(\mathbf{x}, t)$ to find a flamelet l at the location \mathbf{x} and time t have to be implemented, additionally to the equations for the turbulent mean value and the variance of the mixture fraction as well as the transport equation for the

total enthalpy.

In the Eulerian flow field the transport of the non-diffusive particles is described by the advection equation

$$\frac{\partial I_l}{\partial t} + \mathbf{v} \cdot \nabla I_l = 0. \quad (3.12)$$

By combining with Eq. (2.1) and multiplying with the density ρ , it follows

$$\frac{\partial \rho I_l}{\partial t} + \nabla \cdot (\rho \mathbf{v} I_l) = 0. \quad (3.13)$$

The turbulent mean values of the flamelet probabilities can be determined by a Favre averaging for the turbulent flow field from the convective-diffusive transport equations

$$\frac{\partial \bar{\rho} \tilde{I}_l}{\partial t} + \nabla \cdot (\bar{\rho} \tilde{\mathbf{v}} \tilde{I}_l) - \nabla \cdot \left(\frac{\mu_t}{Sc_t} \nabla \tilde{I}_l \right) = 0. \quad (3.14)$$

In this equation, Sc_t is the turbulent Schmidt number for the flamelet probability \tilde{I}_l , which is set to 0.7 corresponding to the turbulent Schmidt numbers for the mixture fraction and the variance of the mixture fraction.

3.3.1 Flamelet Initialization

Starting from the steady solution of the flow and temperature fields, the flamelets are initialized at the beginning of the unsteady flamelet calculations at the time $t_{res} = 0$ s. For the initial distribution of the particle, all cells of the calculation domain, where the fuel-rich conditions of the values $Z > Z_{st}$ for the mixture fraction are fulfilled and the temperature is in a certain range, are chosen. For the calculations of the MILD combustor, the range is between 600 and 1500 K. The initialization criterium can be formulated as follows:

$$\tilde{I}_l(\mathbf{x}) = \begin{cases} 1 & : Z_{st} < \tilde{Z}(\mathbf{x}), T_{min} < T < T_{max} \\ 0 & : else \end{cases} \quad (3.15)$$

The required temperature is calculated by a simple combustion model implemented in the CFD code, for example the mixture fraction/Pdf model [1], related to the model for the chemical equilibrium presented in section 3.1.3. Therefore it is ensured that the flamelets are initialized in a domain in the fuel stream where the pollutant concentrations are neglected because of the

upper limit for the temperature.

The subdivision of the flamelets occurs with the scalar dissipation rate. The initialization domain is subdivided, according to the number of flamelets, in subareas of the same mass in which the scalar dissipation rate is in a corresponding range (see section 5.1). For each flamelet l the conditioned averaged scalar dissipation rate $\widehat{\chi_{st}}(l)$ according to Eq. (3.2) is calculated by an additional weighting with the probability $\tilde{I}_l(l)$ to find a flamelet l .

3.3.2 Distribution of the Flamelet Parameter

Fig. 3.6 shows the distribution of the conditioned scalar dissipation rate in the vertical section plane at the outlet of the mixing nozzle of the MILD combustion chamber discussed in section 5.1. At the inlet of the combustion chamber, the gradients are quite high. The maximum values appear because of the significant turbulence at the inlet. The scalar dissipation rate conditioned on the stoichiometric mixture fraction is high in this region. Fig. 3.7 represents the distribution of the conditioned scalar dissipation rate in the vertical section plane at the outlet of the mixing nozzle as well as in the planes 5, 10, 15 and 20mm above it. This figure shows the expansion of the outlines. Thanks to the entrainment of the combustion air and the hot gas and thus the stream expansion, the outline is shifted outwards in the radial direction. The conditioned scalar dissipation rate is already half as high as at the outlet of the nozzle.

3.3.3 Temporal Evolution of the Flamelet Profile

Because of the temporal evolution of the flamelet parameter the flamelet solutions for the temperature and the species mass fractions as a function of the mixture fraction also experience modifications. The profiles of the evolution of the temperature in the mixture fraction space as well as the evolution of some species mass fractions are plotted in Fig. 3.8 and Figs. 3.9 and 3.10. In Fig. 3.8 not only the temperature but also the enthalpy is represented. The linear distribution makes clear that no lost terms appear. The temperature distribution is determined at the beginning by the initialization of the flamelets with the help of the Burke-Schumann solution. Subsequently the flamelet solution is determined corresponding to the high scalar dissipation rate at time $t = 0s$. Then the temperature is only insignificantly influenced due to the mostly constant scalar dissipation rate in the flamelet. The main

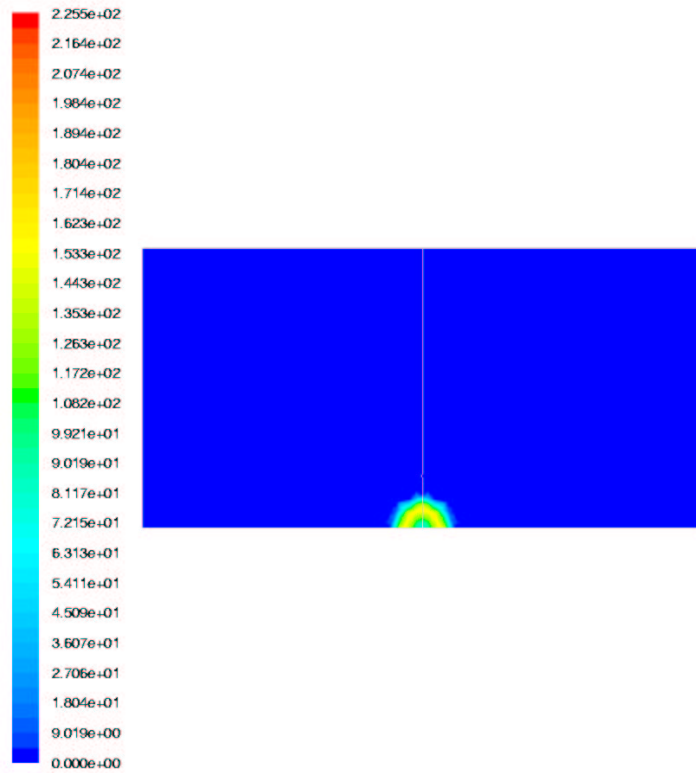


Figure 3.6: Distribution of the conditioned scalar dissipation rate in the plane at the outlet of the mixing nozzle (furnace investigated in section 5.1).

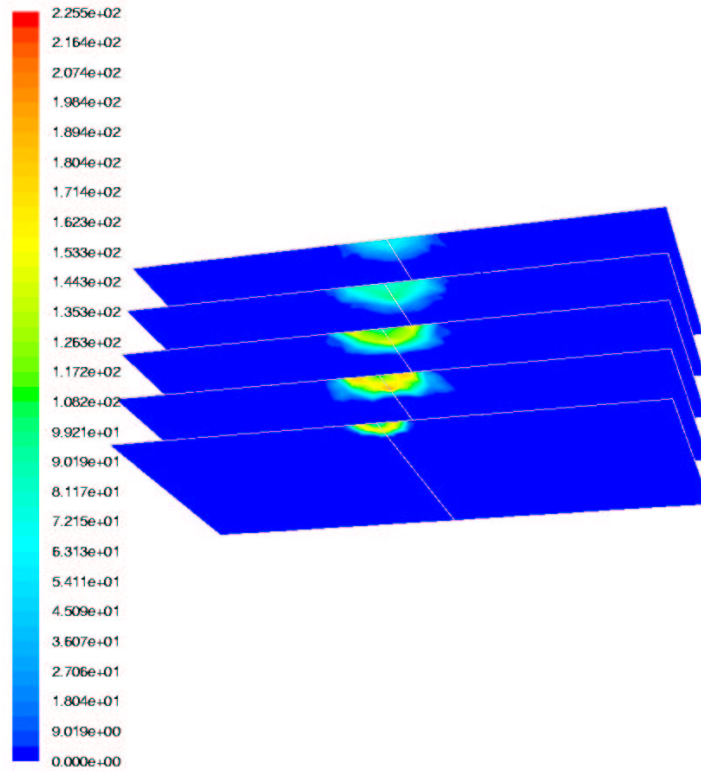


Figure 3.7: Distribution of the conditioned scalar dissipation rate in the plane at the outlet of the mixing nozzle and in the planes 5, 10, 15 and 20mm above (furnace investigated in section 5.1).

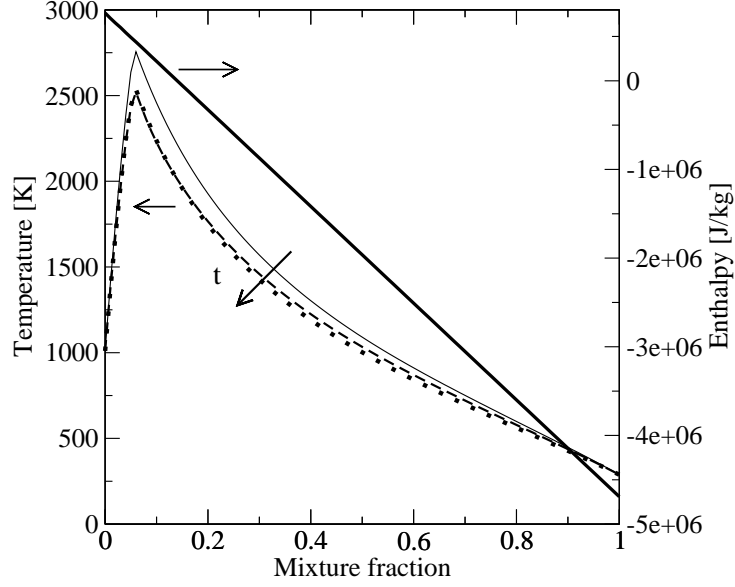


Figure 3.8: Temporal evolution of the temperature and the enthalpy as function of the mixture fraction.

species (fuel, O_2 , CO_2 , H_2O , N_2) are represented in Fig. 3.9. These main species are only slightly influenced by the modification of the scalar dissipation rate at the beginning of the flamelet calculation. It would have been possible to get the distribution of these species with steady flamelets.

Fig. 3.10 shows the temporal evolution of the mass fraction of NO in the mixture fraction space. The formation of NO_x is slow compared to the heat-releasing main reactions, that is why unsteady effects occur. Since nitrogen oxides are essentially formed in the domain of high temperatures because of the thermal formation according to Zel'dovich [93], the profile for NO increases at the beginning of the calculation. The values for NO are especially high at Z_{st} , that is to say in the region of stoichiometric mixture. This is where the temperatures are the highest in the flamelet.

In regions of rich mixture NO is formed with the Prompt-NO path (see section 4.2), since the required hydrocarbon radicals are present and the activation energy of the corresponding reactions is smaller than for the thermal NO. In regions of lean mixture NO can be formed with the Nitrous path.

The local steady species mass fractions are determined from the integration

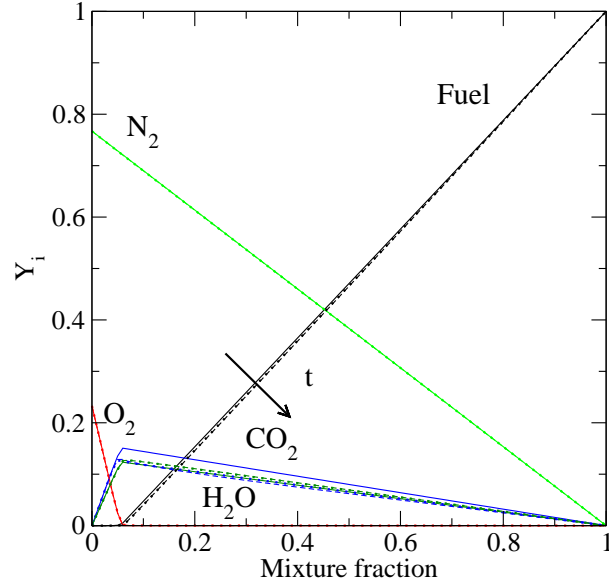


Figure 3.9: Temporal evolution of the mass fraction of the main species as function of the mixture fraction.

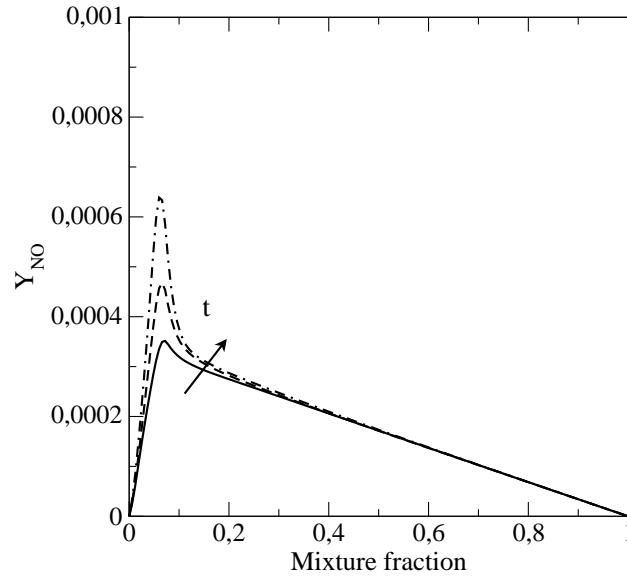


Figure 3.10: Temporal evolution of the mass fraction of nitrogen monoxide as function of the mixture fraction.

over the time, summation over the flamelet probability \tilde{I}_l , integration in the mixture fraction space and weighting with the temporal integration of the flamelet probability:

$$\tilde{Y}_i(\mathbf{x}) = \frac{\int_0^{t_{end}} \sum_l \tilde{I}_l(\mathbf{x}, t) \int_Z Y_{i,l}(Z, t) \tilde{P}_l(Z) dZ dt}{\int_0^{t_{end}} \sum_l \tilde{I}_l(\mathbf{x}, t) dt}. \quad (3.16)$$

Chapter 4

Chemical Mechanisms

Chemical kinetic mechanisms are very important in the numerical simulation of the combustion. They describe all chemical processes (decomposition of the fuel, formation and consumption of intermediate species, formation of NO_x and soot), which occur during the combustion.

Detailed and reduced mechanisms for the C_1 - C_2 kinetics are available in the literature.

In this work, a chemical kinetic mechanism for the C_1 - C_2 kinetics has been upgraded. Special attention is paid to the NO_x formation. For that purpose, the NO_x submechanism of Bollig [15] was added.

The obtained reaction mechanism was reduced by introducing steady state assumptions. Both detailed and reduced mechanisms were used for the numerical simulations in the MILD combustor and to simulate the gaseous phase in the pressurised pulverized coal combustion facility, as presented in chapter 5.

4.1 C_1 - C_2 Kinetics

4.1.1 Reaction paths

The oxidation of the C_1 - C_2 -species and the description of the hydrogen-oxygen system is similar to the mechanism presented in [12]. Some upgrades were performed and this new mechanism is validated against different experimental data from the literature.

The reaction mechanism is given in Appendix A, Table A1. The reaction

paths of the C₁-C₂-mechanism are represented in Fig. 4.1 (for a clarity purpose, only the main species are represented).

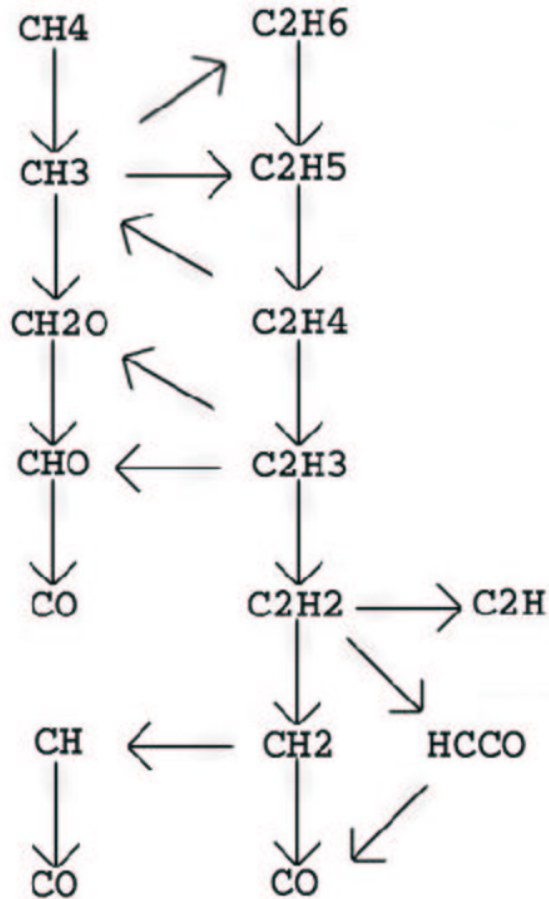
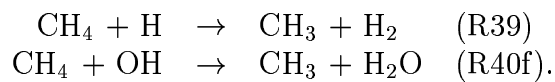


Figure 4.1: Reaction path for the methane oxidation.

For the methane flames, the C₁ and C₂ chains are necessary because the methane oxidation proceeds in two chains. The C₁-chain is the main chain for lean CH₄ oxidation. This means, for lean and stoichiometric combustion, the C₁ chain is sufficient, in particular since the rate-determining reactions are



But the bifurcation to the C₂-chain takes place thereafter through the competition of



and



Then under rich conditions the C₂-chain can lead to the formation of higher hydrocarbons. That is to say that 2 methyl radicals (CH₃) can form a molecule of ethane (C₂H₆), which lead to ethene (C₂H₄) and ethyne (C₂H₂). Those intermediate products are depleted to CO and CH₂ as shown in Fig. 4.1.

4.1.2 Validation

In the following, some validation calculations will be presented. Special care was paid to the ignition delay time and the burning velocity.

Ignition delay time

Figs. 4.3, 4.4, 4.5 (pages 53, 54 and 55) show the ignition delay time of a mixture of methane, oxygen and argon and of methane, ethane, oxygen, argon. The pressures are between 1.6 and 6.1 atm. The equivalence ratio is about 1.0. It can be seen that the simulation with the detailed mechanism reproduces the measured ignition delay time very well for the whole range of initial temperature.

Burning velocity

Fig. 4.7 represents the burning velocity of the mixture methane-air. The burning velocity is plotted against the equivalence ratio. The pressure is 1 atm and the unburnt temperature is 300 K. The calculated burning velocity with the detailed mechanism is in a good agreement with the measurements.

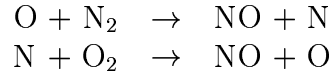
4.2 NO_x Model

The NO_x mechanism taken into account for the simulation of the pollutant was added to the C₁-C₂-mechanism described above. It considers the most important paths of NO_x formation and consumption.

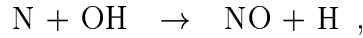
The NO_x submechanism takes the contribution of thermal NO, prompt NO and nitrogen oxide into account for the NO formation, as well as the NO_x-reburn by hydrocarbon radicals and amines (NH_x).

The detailed NO_x reaction mechanism was compiled by Bollig [15] and validated against experimental data for different flame structures. The main paths for the formation and consumption are identified by a reaction path analysis for a n-heptane diffusion flame [15]. They are shown in Fig. 4.2.

For combustion processes with temperatures higher than 1800 K the thermal NO mechanism of Zel'dovich is the most important formation path:



Lavoie [50] extended those two reactions with a third one:

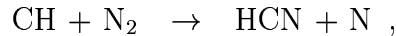


which contribution is very important.

This so-called "extended Zel'dovich" mechanism has a strong temperature dependance due to the high activation energy of 319 kJ/mol of the initial-ization reaction $\text{O} + \text{N}_2 \rightarrow \text{NO} + \text{N}$. Under diesel-engine relevant conditions these reactions represent the main formation path for NO_x. The NO_x formation by this path exceeds the formation by the other paths (prompt NO, nitrogen oxide, reburn-NO) of one order of magnitude.

With increasing exhaust gas recirculation the contribution of the prompt NO increases, however the thermal mechanism still remains the dominating one.

The prompt NO path, or Fenimore path, is initiated by the attack of an hydrocarbon radical, among which CH is the most effective:



Hereafter HCN reacts via CN or NCO to give N and finally forms NO.

The nitrous NO path is initiated by the following reactions:

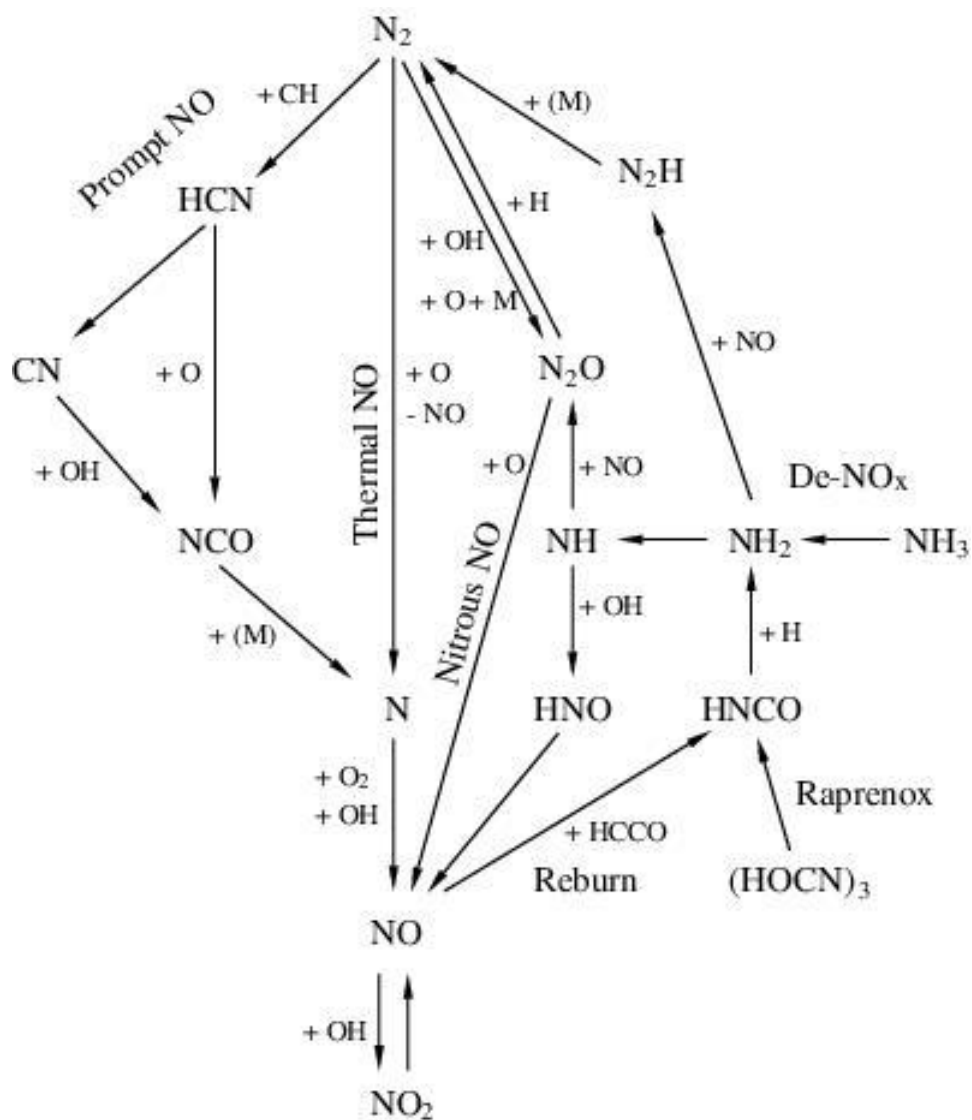
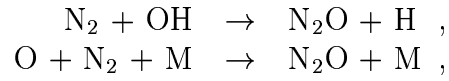
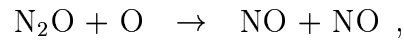


Figure 4.2: Reaction path analysis of hydrocarbon diffusion flame for $P = 40$ bar, taken from Bollig [15].



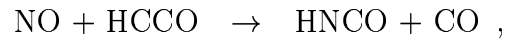
The trimolecular recombination $\text{O} + \text{N}_2 + \text{M} \rightarrow \text{N}_2\text{O} + \text{M}$ is more important for high pressures.

Under lean conditions N_2O reacts to NO :



Under rich conditions the paths via Imidogen (NH) are faster.

NO can also be reduced by the reburn path. It is initiated by the reaction:



Isocyanic acid HNCO reacts then to amidogen (NH_2). Amidogen and imidogen can reduce another NO to form N_2O or N_2H . Under rich conditions both paths can lead to molecular nitrogen. Both paths are used in technical processes to reduce NO_x .

4.3 Reduction of Chemical Mechanisms

Reducing complex kinetics schemes by the introduction of steady state assumptions has been known for a long time and successfully applied as it can be found in the literature.

Flame chemistry for most of the hydrocarbons proceeds in reaction chains. Each intermediate species is produced and consumed by only a few major reactions. Algebraic expressions for these species can be derived from their steady state relations.

Reduced mechanisms are useful because they reduce the computational effort in numerical calculations of flames by replacing the differential equations for those intermediate species that are assumed to be in steady state by algebraic relations.

4.3.1 Steady-State Assumptions for Radicals

The systematic reduction of reaction kinetics is described in details in [67] for hydrogen and methane flames. The same procedure of steady state approximations was applied here to reduce the detailed mechanism.

The term "steady state" was introduced because the time derivative of these species is set to zero

$$\frac{d[C_i]}{dt} = 0 = \sum_{k=1}^r \nu_{ik} w_k. \quad (4.1)$$

Here t denotes the time and w_k the reaction rate

$$w_k = k_f \prod_{j=1}^n [X_j]^{\nu_j'} - k_b \prod_{j=1}^n [X_j]^{\nu_j''} \quad (4.2)$$

where ν' is the stoichiometric coefficient of the reactants and ν'' the stoichiometric coefficient of the products.

A steady-state approximation for species i can be justified in physical terms. The rate at which species i is consumed is much faster than the rate by which it is produced. Then its concentration always stays much smaller than those of the initial reactants and the final products. Since the concentration always stays small, its time derivative also stays small compared to the time derivatives of the other species and we can set

$$\frac{d[C_i]}{dt} = 0. \quad (4.3)$$

In [67] the reduction of a hydrogen-oxygen mechanism involving only 8 reactions is illustrated and enables to understand the way to proceed. The main steps can be summarized as follows:

1. Choice of steady-state species
2. Choice of reactions that deplete these species
3. Truncation of steady-state relations
4. Apparition of partial equilibria as a consequence of truncation

For a short mechanism, those steps can easily be done per hand. However it becomes cumbersome when considering a larger mechanism. The use of a preprocessing programme of [71] makes it possible to treat all type of mechanisms and enables to get the expression of the concentration of the steady-states species depending on the concentration of the other remaining species.

In order to identify the influence of each individual reaction on the solution, sensitivity analysis is carried out. Furthermore this helps to choose the fast reactions that are to be eliminated later.

4.3.2 The Reduced Mechanism

To reduce the detailed reaction mechanism presented in sections 4.1 and 4.2, 12 steady-state assumptions were introduced. This leads to a reduced mechanism of 19 global reactions with 23 species. The global reaction mechanism is given in Table 4.1.

This reduced mechanism was validated by the means of comparisons with experimental data from the literature and comparison with the detailed mechanism.

Figures 4.3 and 4.4 represent the ignition delay time of a mixture of methane, oxygen and argon in an Arrhenius diagramm. The equivalence ratio is 1 (the mixture is stoichiometric) and the pressure is respectively 1.8 and 2.04 atm. The reduced mechanism reproduces exactly the same ignition delay time as the detailed mechanism does and is in agreement with the measurements from [79].

Number	Reaction		
I:	$\text{H} + \text{CH}_4$	$=$	$\text{H}_2 + \text{CH}_3$
II:	2CH_3	$=$	C_2H_6
III:	$2 \text{H} + \text{C}_2\text{H}_6$	$=$	$\text{H}_2 + 2 \text{CH}_3$
IV:	$\text{O}_2 + 2 \text{CH}_3$	$=$	$\text{H}_2 + \text{HO}_2 + \text{C}_2\text{H}_3$
V:	$\text{H} + \text{C}_2\text{H}_3$	$=$	$\text{H}_2 + \text{C}_2\text{H}_2$
VI:	$\text{O} + \text{C}_2\text{H}_2$	$=$	$\text{CO} + \text{CH}_2$
VII:	$\text{O}_2 + \text{CH}_3$	$=$	$\text{OH} + \text{CH}_2\text{O}$
VIII:	$2 \text{H} + \text{CH}_2\text{O}$	$=$	$2 \text{H}_2 + \text{CO}$
IX:	$\text{O}_2 + 2 \text{H} + \text{CH}_2$	$=$	$\text{O} + 2 \text{H}_2 + \text{CO}$
X:	$\text{OH} + \text{CO}$	$=$	$\text{H} + \text{CO}_2$
XI:	2HO_2	$=$	$\text{O}_2 + \text{H}_2\text{O}_2$
XII:	$\text{OH} + \text{H}_2\text{O}_2$	$=$	$\text{H}_2\text{O} + \text{HO}_2$
XIII:	$\text{O}_2 + \text{N}_2$	$=$	2NO
XIV:	$\text{CH}_3 + \text{NO}$	$=$	$\text{H}_2\text{O} + \text{HCN}$
XV:	$\text{O} + \text{HCN}$	$=$	$\text{H} + \text{NCO}$
XVI:	$\text{H} + \text{NCO}$	$=$	$\text{CO} + \text{NH}$
XVII:	$\text{O} + \text{NH}$	$=$	$\text{H} + \text{NO}$
XVIII:	$\text{H}_2\text{O} + \text{N}_2$	$=$	$\text{NH}_2 + \text{NO}$
XIX:	NH_2	$=$	$\text{H} + \text{NH}$

Table 4.1: The 19-step global reaction mechanism for methane. The corresponding global rates are given in Appendix B.

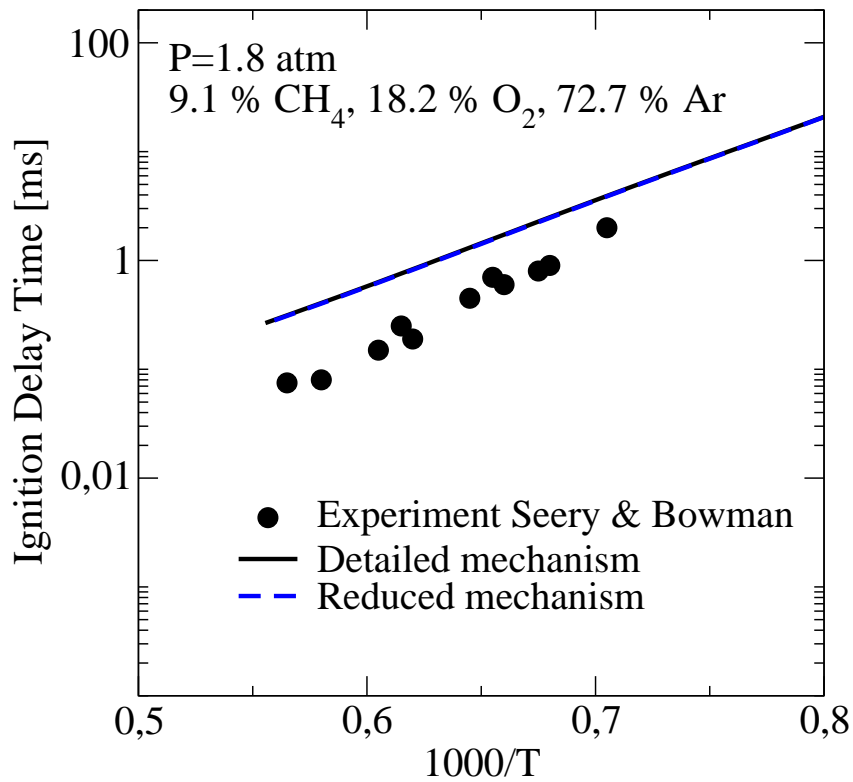


Figure 4.3: Comparison of computed (full line: detailed mechanism, dashed line: reduced mechanism) and experimental (from [79]) ignition delay time of a mixture of methane, oxygen and argon. $P = 1.8 \text{ atm}$, $\Phi = 1.0$.

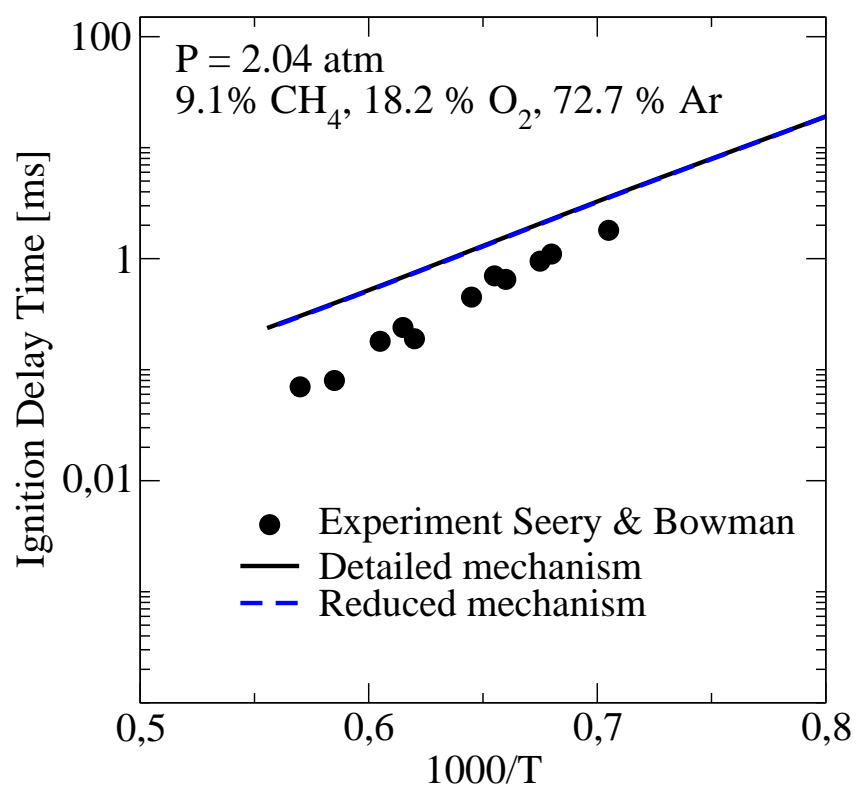


Figure 4.4: Comparison of computed (full line: detailed mechanism, dashed line: reduced mechanism) and experimental (from [79]) ignition delay time of a mixture of methane, oxygen and argon. $P = 2.04$ atm, $\Phi = 1.0$.

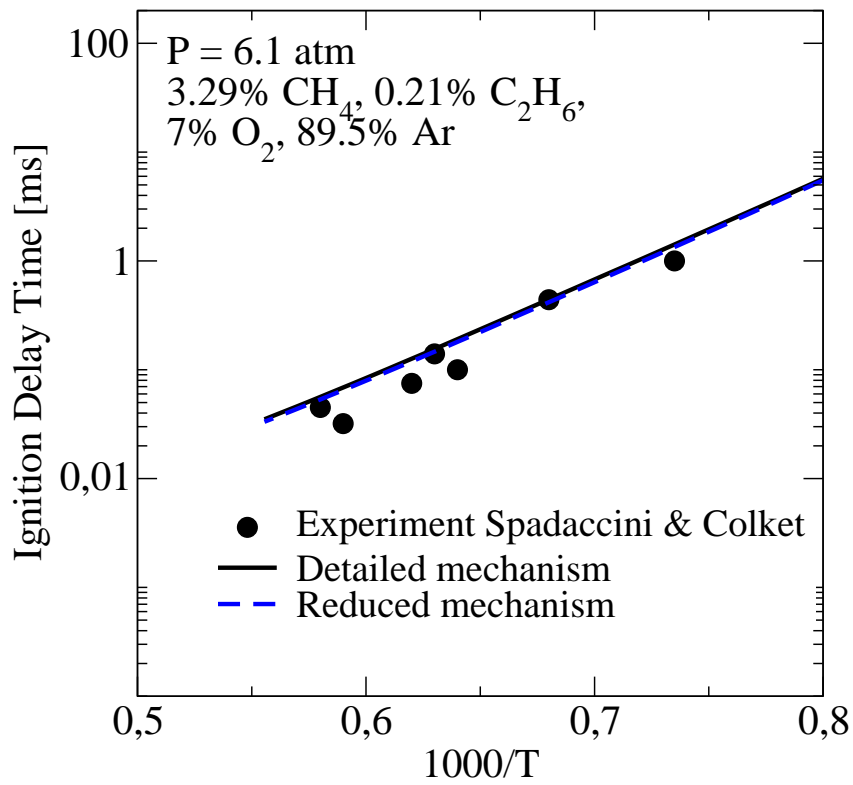


Figure 4.5: Comparison of computed (full line: detailed mechanism, dashed line: reduced mechanism) and experimental (from Spadaccini and Colket [81]) ignition delay time of a mixture of methane, ethane, oxygen and argon. $P = 6.1 \text{ atm}$, $\Phi = 1.045$.

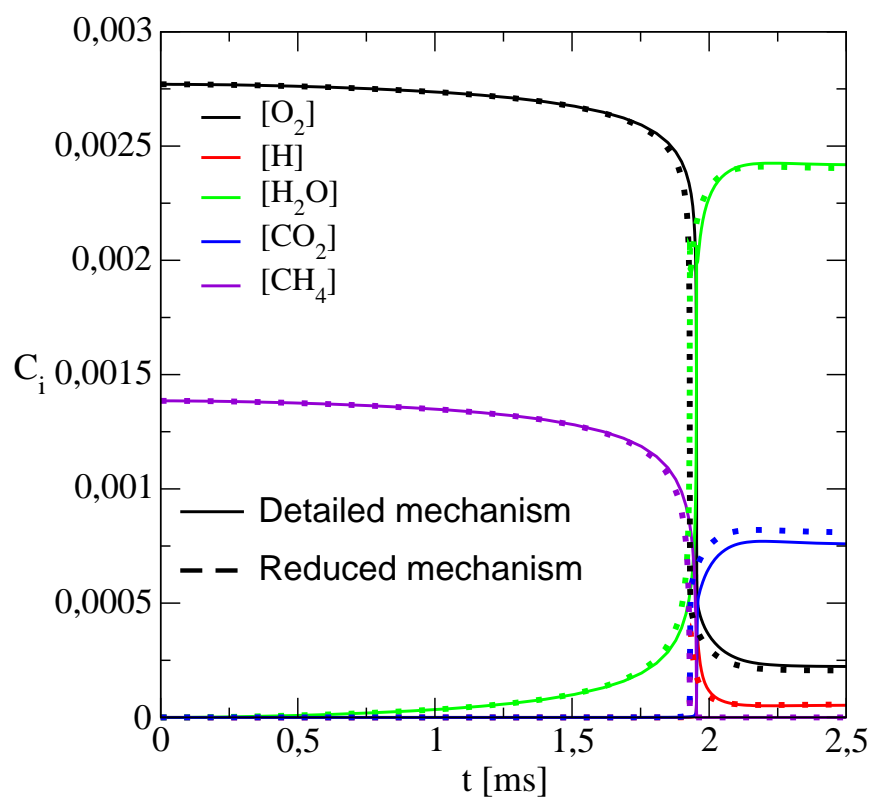


Figure 4.6: Comparison of computed (full line: detailed mechanism, dashed line: reduced mechanism) concentration of some main species depending on the time. $T_0 = 1500K$, $P = 6.1$ atm.

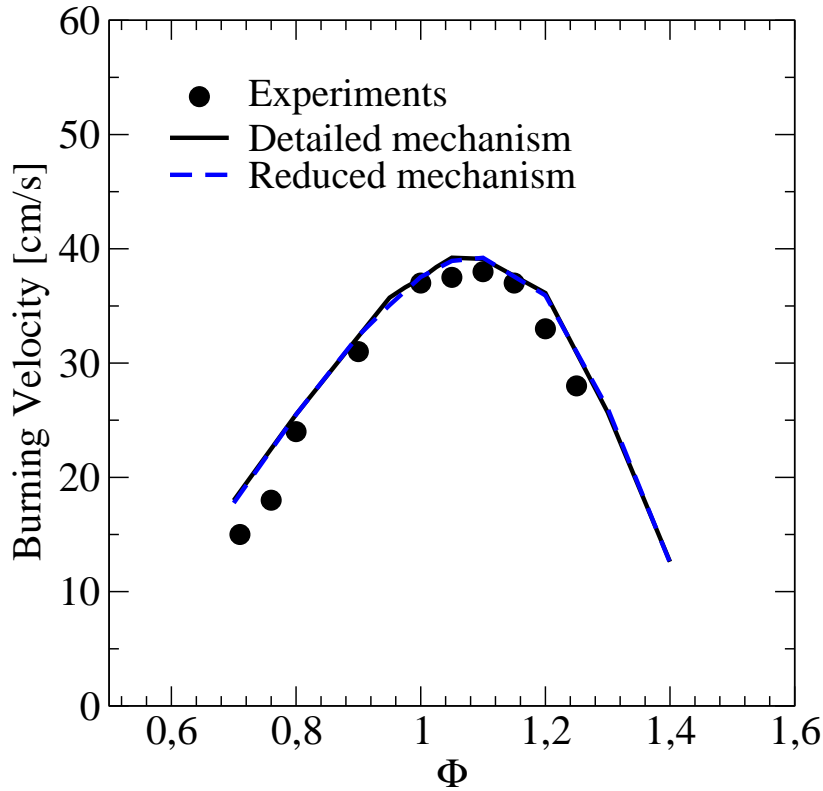


Figure 4.7: Comparison of computed (full line: detailed mechanism, dashed line: reduced mechanism) and experimental (from Vagelopoulos et al. [87]) burning velocity of the mixture methane-air. $P = 1$ atm, $T_u = 300$ K.

Another comparison between the reduced and the detailed mechanism is also to see in Fig. 4.5 that shows the ignition delay time of a mixture of methane, ethane, oxygen and argon for a pressure of 6.1 atm and an equivalence ratio of 1.045. Both detailed and reduced mechanisms predict an ignition delay time in total agreement with the experimental data from Spadaccini [81].

In Fig. 4.6, the boundary conditions are the same than those of Fig. 4.5. For an initial temperature of 1500K, the concentration of some main species are plotted against the time. Even if there are no experimental data to compare with, this kind of comparison is important to check whether the reduced mechanism can deliver the same concentration profiles as the detailed mechanism does. In this plot, it can be clearly seen that this is the case.

The burning velocity of the mixture methane-air at a pressure of 1 atm and an unburnt temperature of 300K is shown on Fig. 4.7 as a function of the equivalence ratio. The points represent the experimental data from [87], the full line is the representation of the burning velocity calculated with the detailed mechanism and the dashed line represents the burning velocity predicted by the reduced mechanism. For the whole range of equivalence ratios, both lines coincide, thus showing the total agreement between the two types of chemistry (detailed and reduced) and the measurements.

4.3.3 Concluding Remarks

Nowadays it is possible to develop kinetic mechanisms for various fuels. After they have been assembled, these mechanisms are validated against experiments for different configurations. Depending on the model fuel, the final reaction mechanism can be very long. The introduction of such mechanisms into complex multi-dimensional CFD simulations results in increased computational time. The use of a so-called reduced reaction mechanism is of particular interest since the number of reactions and species is smaller, the computational time is reduced and the precision is conserved.

4.4 Combustion of Solid Carbon Particles

In chapter 5.2, results of the simulation of coal combustion are presented. The main purpose of this work is to couple the Eulerian Particle Flamelet Model (see section 3.3) with the 3D CFD code FLUENT when considering solid particles, thus showing the ability of this model to describe the gaseous phase also in the solid/gas configuration.

This work concentrates on the kinetics of the gaseous phase described in section 4.1. The pyrolysis and burnout models for the combustion of solid carbon particles are taken from FLUENT [1] and described in the following.

When heating coal, gaseous components escape from the coal when the temperature exceeds 300 °C. This is the so-called coal pyrolysis in the course of which char and volatiles appear during the heating. If the temperature is high enough and there is oxygen in the vicinity, char burnout (the heterogeneous reaction of carbon in the char with the gaseous phase) and volatiles combustion (the homogeneous reaction of the volatiles in the gaseous phase) occur. The coal pyrolysis occurs one order of magnitude faster as the char burnout [2], hence these processes are considered, for simplification purposes, to take place consecutively, as represented on Fig. 4.8 [29].

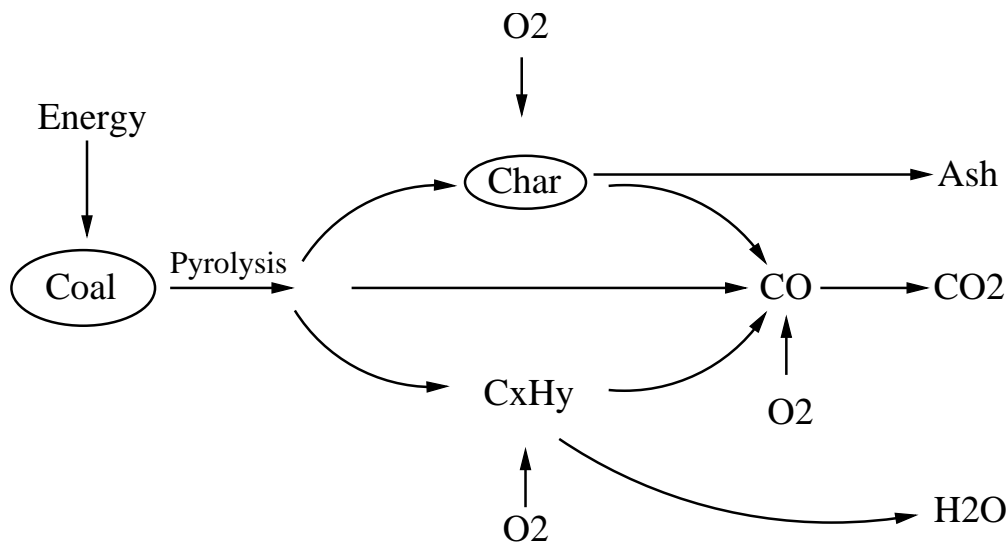


Figure 4.8: Schematised coal combustion model from Görner [29].

Further to CO and the volatiles containing hydrocarbons, symbolically represented by C_xH_y on Fig. 4.8, char appears during the pyrolysis. Afterwards, carbon in the char reacts with oxygen. For a complete burnout of the char, ash remains. And after some reactions in the gaseous phase, the main products of the coal combustion are formed (CO_2 , H_2O and ash).

4.4.1 Pyrolysis Model

By means of experiments, Kobayashi et al. [43] studied the pyrolysis behaviour of different coals, among them the brown coal Montana lignite. From these experimental results, parameters of the Arrhenius ansatz were derived for a one-step reaction, so that the rate of the mass reduction due to pyrolysis could be expressed as exact as possible for every coal. Doing so, the Arrhenius parameters were determined (frequency factor and activation energy). But a higher quantity of volatiles was noticed, mainly because of the high temperature. That is the reason why Kobayashi et al. suggested an empirical model with two competing reactions, in order to capture the modification of the volatiles quantity and the pyrolysis kinetics varying with the temperature. The two competing reactions are represented in Fig. 4.9.

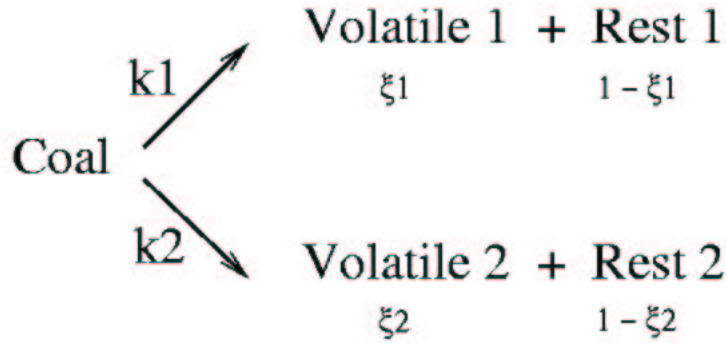


Figure 4.9: Model with two competing reactions from Kobayashi [43].

The parameters ξ_1 and ξ_2 represent the stoichiometric coefficients for the mass of the volatiles for each reaction path. The rate constants k_1 and k_2

are:

$$\begin{aligned} \mathbf{k}_1 &= \mathbf{A}_1 \cdot \exp\left(\frac{-\mathbf{E}_1}{RT}\right) \\ \mathbf{k}_2 &= \mathbf{A}_2 \cdot \exp\left(\frac{-\mathbf{E}_2}{RT}\right) \end{aligned} \quad (4.4)$$

A_1 and A_2 are the frequency factors, E_1 and E_2 the activation energies of reaction 1, respectively 2. The first reaction dominates for quite low temperatures and leads to relative volatiles yield of ξ_1 . For high temperatures, the second reaction becomes faster than the first one and leads to a higher quantity of volatiles with ξ_2 .

The parameter ξ_1 is determined thanks to low-temperature experiments. On the one hand, this two competing reactions model enables a better description of the pyrolysis kinetics, since there are 6 parameters. On the other hand, this model can lead to worse results if the values of the parameters are extrapolated for other heating rates and temperatures.

In the literature, the parameter values from Ubhayakar et al. [85] are preferred because the values from Kobayashi predict a too slow pyrolysis kinetics for high heating rates and temperatures (see [36]). The parameter values for the two competing rates are given in Table. 4.2. These data were obtained by adjustment of various experimental data from different authors, like [3].

	A_1 [s ⁻¹]	A_2 [s ⁻¹]	E_1 [kJ/mol]	E_2 [kJ/mol]	ξ_1 [-]	ξ_2 [-]
Ubhayakar et al. [85]	$1.34 \cdot 10^5$	$1.46 \cdot 10^{13}$	74	251	0.459	0.9

Table 4.2: Parameter values for the two competing rates Kobayashi model.

In section 5.2, the pyrolysis is calculated by FLUENT and the gaseous phase by the RIF code, which means that the combustion of the volatiles is simulated by the flamelet model. For that purpose, an assumption for the composition of the volatiles has to be made in order to initialize the RIF calculation. This step is explained in section 5.2.3.

4.4.2 Burnout Model

After the volatiles escape from the coal particle, the char burnout occurs. It is assumed that the carbon in the char reacts with the oxygen of the gaseous

phase and forms carbon monoxide (CO).

The kinetic/diffusion-limited rate model assumes that the surface reaction rate is determined either by kinetics or by diffusion rate.

The mass reduction of the carbon particle during the char burnout is determined by (see [9] and [26]):

$$\frac{dm_p}{dt} = -\pi d_p^2 \frac{\rho_g R T_\infty \xi_{O_2, \infty}}{M_{O_2}} \frac{k_{kin} k_{diff}}{k_{kin} + k_{diff}}, \quad (4.5)$$

where k_{kin} is the kinetical rate constant and k_{diff} the rate constant for the diffusion:

$$k_{kin} = A_{kin} \exp\left(-\frac{E_{kin}}{RT_p}\right) \quad (4.6)$$

and

$$k_{diff} = A_{diff} \frac{0.5(T_p + T_\infty)^{0.75}}{d_p}. \quad (4.7)$$

The values of the rate constants parameters are given in Table 4.3.

A_{kin} [kg/(m ² · Pa · s)]	E_{kin} [J/kmol]	A_{diff} [kg/(m · Pa · s · K ^{0.75})]
$2.0 \cdot 10^{-3}$	$7.9 \cdot 10^7$	$5.0 \cdot 10^{-12}$

Table 4.3: Parameter values for the kinetic/diffusion surface reaction rate model.

Chapter 5

Results and Discussions

5.1 Simulation of a MILD Combustor

The *FLOX*[®] combustor (described in the following) is investigated numerically using the Eulerian Particle Flamelet Model (EPFM). The flamelet code solves the unsteady flamelet equations and is coupled to an unstructured CFD code providing solutions for the flow and mixture field from which the flamelet parameters can be extracted. Flamelets are initialized in the fuel rich region close to the fuel jet inlets of the combustor. They are represented by marker particles which are convected through the flow field. Each flamelet takes a different pathway through the combustor leading to different histories for the flamelet parameters. Equations for the probability of finding a flamelet at a certain position and time are additionally solved in the CFD code (FLUENT).

The chemistry is solved in a one dimensional flamelet code calculating species and temperature profiles as functions of a conserved scalar, the mixture fraction. This solution procedure allows high resolution in time for the chemistry independent from the CFD calculations and therefore the usage of detailed chemical kinetics.

To model the chemical properties of the fuel, a detailed reaction mechanism for hydrocarbon fuels is used. It contains hydrocarbon species with up to 2 carbon elements. It includes a detailed NO_x submechanism as explained in the previous chapter. The detailed chemistry is needed to model transient

effects that are not covered by simple combustion models as applied in most CFD codes. This can be achieved by using the Eulerian Particle Flamelet Model (EPFM) which is an extension to the highly validated Representative Interactive Flamelet Model (RIF, described in 2.4). The latter is based on the laminar flamelet concept for non premixed combustion and has the advantage of separating the numerical effort associated with the resolution of the small chemical time and length scales from the CFD computation of the flow field. In this model, turbulent flames are treated as an ensemble of thin locally one dimensional laminar flamelets which are strained and stretched by the turbulent flow field. In a *FLOX*[®] combustor the smallest chemical time and length scales can be assumed to be smaller than those of the turbulence, ensuring that the laminar structure of the flame is disturbed but preserved.

The EPFM model was first applied to a gas turbine combustion chamber burning in a steady state using n-heptane as model fuel. Pollutant formation was investigated by introducing Eulerian particles transported unsteadily in the steady state flow field computed with a CFD code. Each particle represents an unsteady flamelet accounting for different pathways and thereby different histories of the flamelet parameters and different residence times for the flamelets. The same concept was successfully applied to a MILD combustor [78] and is now applied to the *FLOX*[®] combustor investigated here.

5.1.1 Experimental Set-up

The pressure vessel features a combustion chamber of 56 x 56 mm² cross section and 218 mm in height (Fig. 5.1). Optical access to the combustion chamber is through three windows (55 x 36 mm²) that cover one fourth of the combustion chamber that can be placed at four different heights to allow optical access to the whole length of the combustion chamber.

The pressure vessel is first heated with a premixed methane flame on the top of the combustion chamber. When the chamber temperature exceeds 900 °C (1173K), the premixed flame is turned off and air and fuel are injected below. The exhaust gases are used to preheat the air to the desired level.

The *FLOX*[®] pressure vessel is also represented on Fig. 5.2. The red surface is the exhaust. The details of the mixing nozzle can be seen on Fig. 5.3.

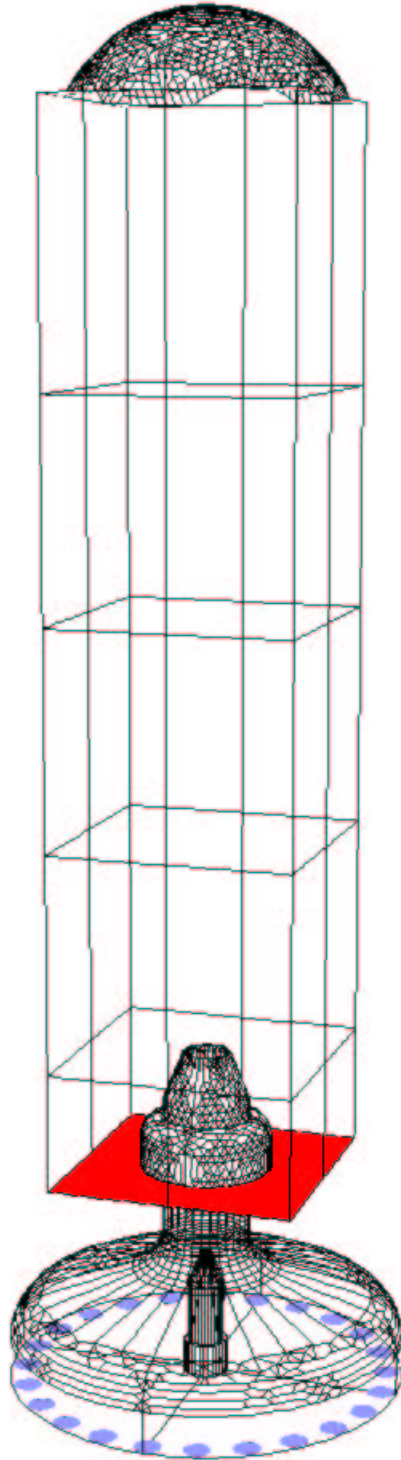


Figure 5.1: Representation of the furnace.

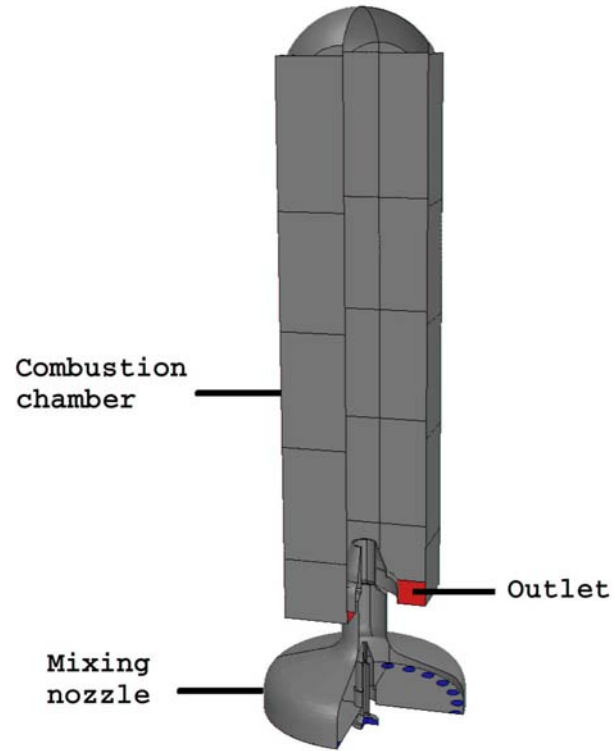


Figure 5.2: FLOX Furnace. The details of the mixing nozzle are shown in Fig. 5.3.

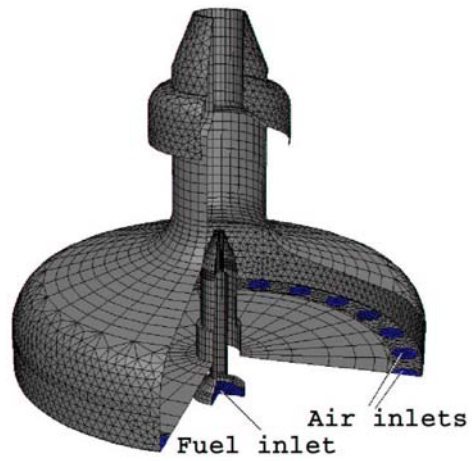


Figure 5.3: Mixing nozzle.

5.1.2 Computational Grid

Due to the symmetry of the combustor, only 1/4 of the chamber needs to be represented. The grid contains about 100000 cells and is delimited at the symmetry planes by the zones with corresponding symmetry boundary conditions. The profiles of the temperature, mixture fraction and chemical species are represented in this vertical cut plane.

The dimensions of the chamber grid (including the mixing geometry) are: 45.5 mm x 45.5 mm x 318 mm (length x width x height). It is showed on Fig. 5.1

The dimensions of the chamber are:

56 mm x 56 mm x 258 mm (length x width x height).

The mixing geometry is represented on Fig.5.3 with details of the inlets as well as the details of the mesh used for the computation. The fuel injector has a diameter of 2 mm. The 24 air injectors have a diameter of 6 mm. The injector at the inlet of the chamber (after the mixing of fuel and air) has a diameter of 10 mm.

5.1.3 Comparison with the Experimental Results

Measurements of chemical species and temperatures were performed in the FLOX[®] pressure vessel for a pressure of 5 bar, with varying air ratios [82]. The fuel used is methane and the oxidizer is air. Two cases are considered in this work, the sum-up of the boundary conditions is in Table 5.1.

	fuel	oxidizer	pressure [bar]	T_{fuel} [K]	T_{air} [K]	λ [-]	\dot{m}_{fuel} [kg/s]	\dot{m}_{air} [kg/s]
case 1	methane	air	5	288	804	2.76	9.95e-05	4.30e-03
case 2	methane	air	5	288	1010	3.07	9.95e-05	4.75e-03

Table 5.1: Boundary conditions of the combustion chamber.

The application of the Eulerian Particle Flamelet Model is based on a steady solution of the flow and temperature field, which is calculated with the model

integrated in the CFD code. The application of the criteria for the initialization of the domain explained in section 3.3.1 are used for the simulation of the MILD combustion chamber. The initialization is shown in Fig. 5.4.

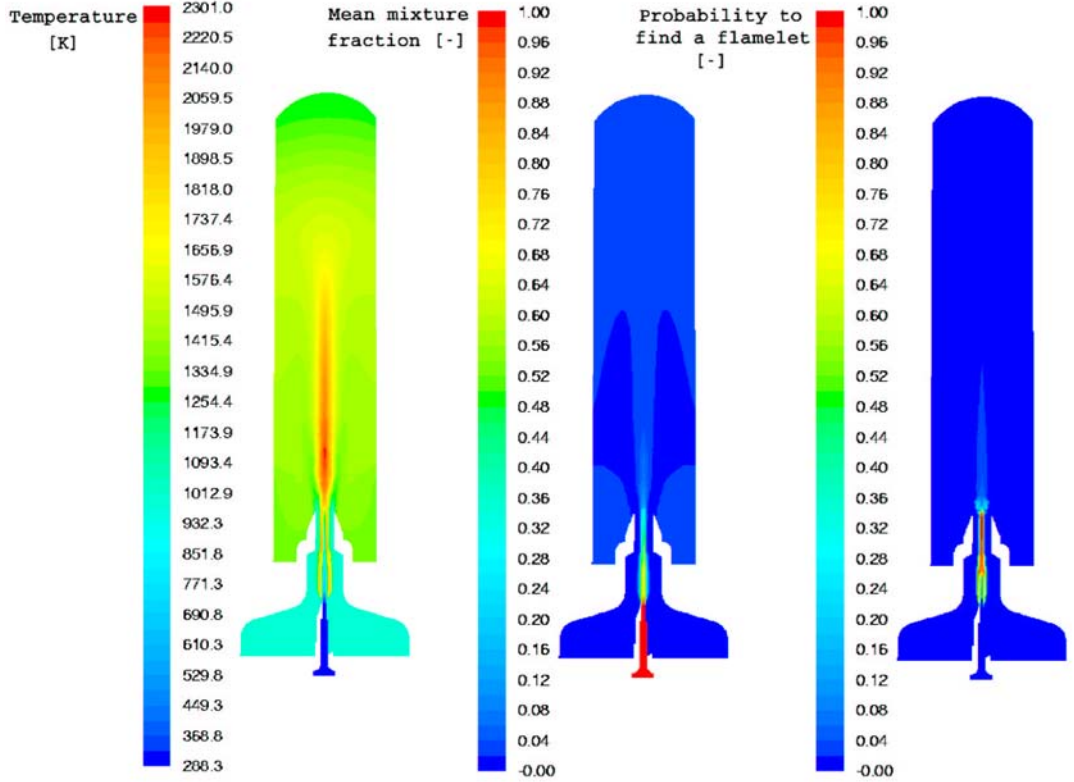


Figure 5.4: Temperature [K] (left), mean mixture fraction (middle) profiles and initial distribution of flamelets at $t = 0$ s (right).

Flow field

Fig. 5.5 shows the calculated flow field in a vertical cut-plane through the fuel inlet. The path lines are colored by the velocity magnitude. The flow is characterised by the strong exhaust gas recirculation.

The hot gases go to the top of the chamber and are deviated to the side walls, where the flow is led to the bottom of the chamber. Internal recirculation occurs there whereas the rest of the flow leaves the chamber through the exhaust. The thermal energy gained is used to warm up the combustion air.

On the sides, the flow is dominated by the formation of an eddy, inside of which long residence times are reached. This eddy is due to the inlet flow in the middle of the combustion chamber. The same effect was observed in a similar MILD combustor [77].

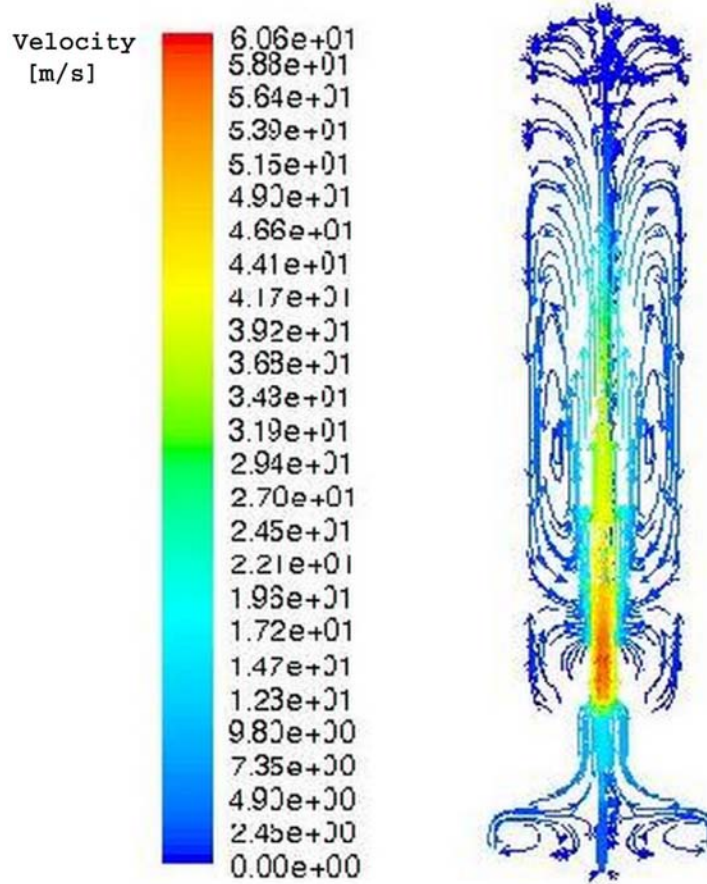


Figure 5.5: Pathlines colored by velocity [m/s], case 2.

Temperature and Nitrous Oxide

Figures 5.6 and 5.7 show the temperature and the nitrous oxide profiles in a vertical cut-plane through the fuel inlet, calculated with the detailed and the reduced mechanism. Two features can be noticed:

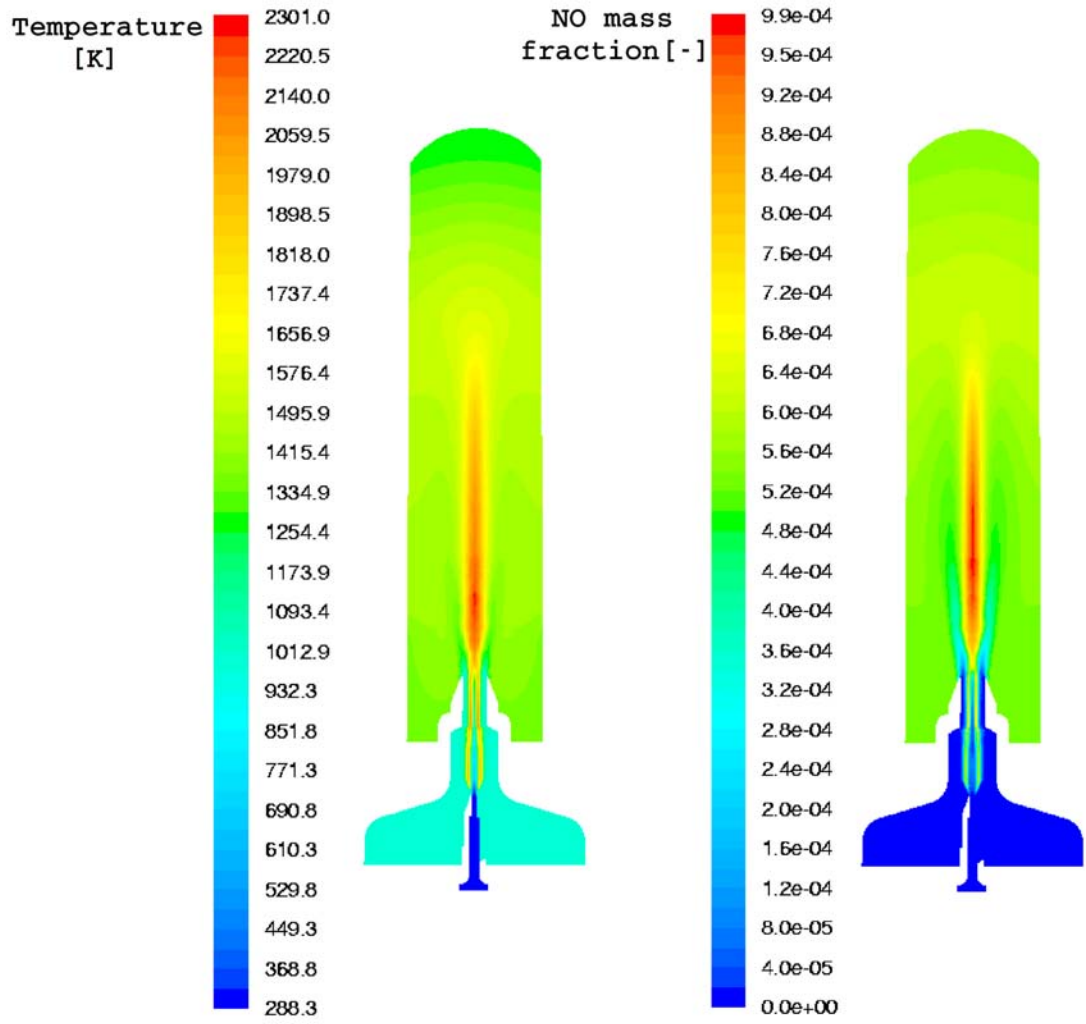


Figure 5.6: Temperature [K] (left) and NO mass fraction (right), case 2 (simulation with the detailed kinetics).

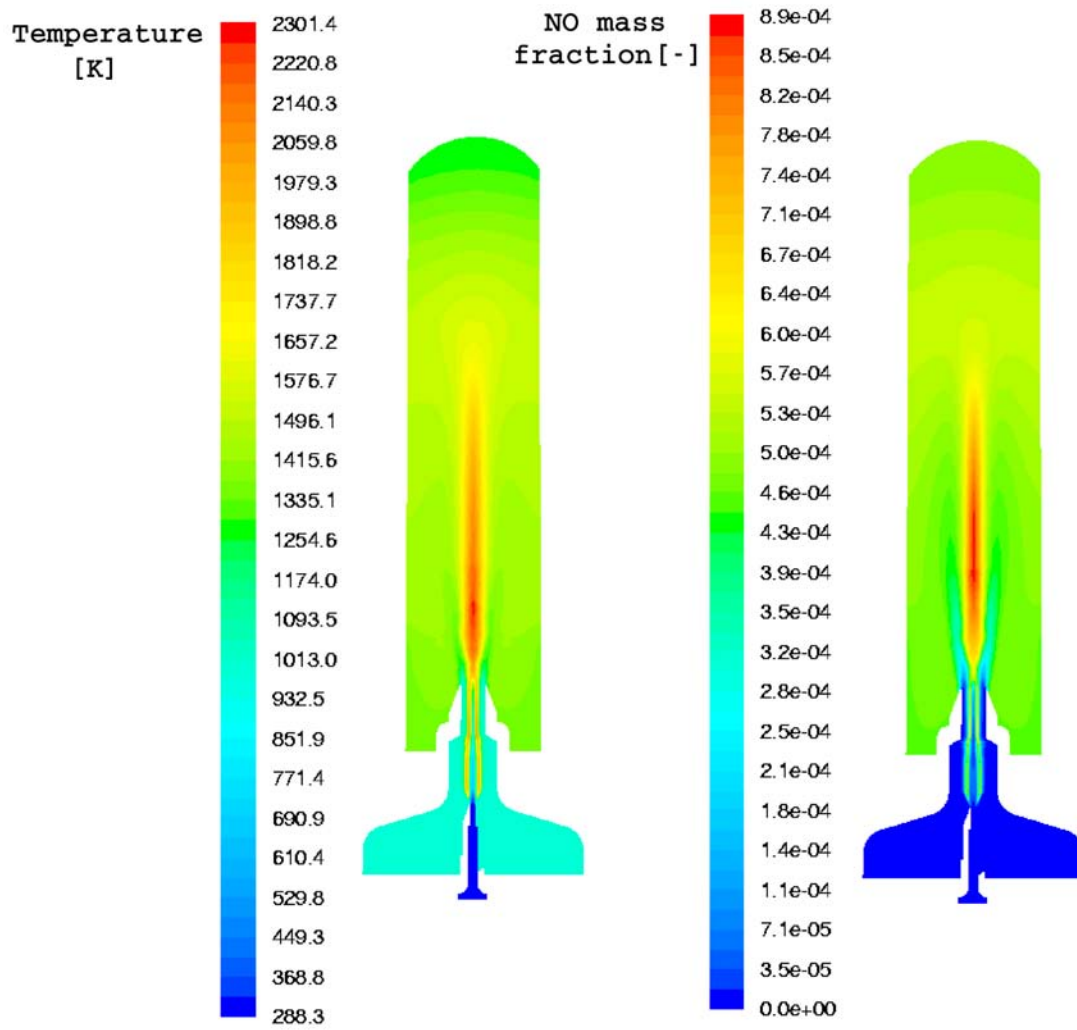


Figure 5.7: Temperature [K] (left) and NO mass fraction (right), case 2 (simulation with the reduced kinetics).

- The nitrous oxide profile correlates with that of the temperature. This is mainly due to the strong temperature dependence of the Zel'dovich mechanism for thermal production of NO [93] (N35f, N36f, N37f in Appendix A) because of the high activation energy of 313 kJ/mol of the initialization reaction $O + N_2 \rightleftharpoons NO + N$ (N37b). In [15], a relation for the temporal evolution of the concentration of NO was derived, by introducing a steady-state assumption for N. This relation depends on the temperature, pressure and concentration of stable species, thus making the high temperature dependence clear:

$$\frac{d[NO]}{dt} = 1.45 \cdot 10^{17} T^{-1/2} \exp(-69460 K / T(K)) * [O_2]_{eq}^{1/2} [N_2]_{eq} \quad (5.1)$$

This equation is not used in this work but shows that the high concentration of NO is to be found in the high temperature zone.

- When comparing the results of the simulations with the detailed and the reduced chemistry, it can be noticed that the general trend is the same. This agreement between both mechanisms underlines the fact that the reduced mechanism can be used in the CFD simulations in order to reduce the computational time, without losing any important information.

Measured and calculated values for the temperature, NO, O₂ and CO₂ are listed in Tables 5.2 and 5.3 for two different cases (boundary conditions are found in Table 5.1). The temperatures predicted by the simulation using the reduced chemistry are almost the same as the temperatures obtained by the simulation using the detailed chemistry. As can be seen by comparing with the measurements, the simulation slightly overpredicts the temperatures, but still leads to a good agreement with the experiments. The trend stays the same.

Due to a slightly higher temperature in the simulations, the NO emissions are also overpredicted since they strongly depend on temperature. However it is important to point out the ability of the model to predict these emissions in the right order of magnitude. Furthermore the values for O₂ and CO₂ are in good agreement with the measurements.

	T <i>top</i> <i>chamber</i> [K]	T <i>middle</i> <i>chamber</i> [K]	T <i>exhaust</i> [K]
case 1			
experiments [82]	1161	1258	1179
simulation, detailed	1235	1393	1334
simulation, reduced	1229	1388	1331
case 2			
experiments [82]	1279	1433	1301
simulation, detailed	1243	1447	1345
simulation, reduced	1243	1447	1345

Table 5.2: Comparison of the measurements and the simulations with detailed and reduced kinetics.

	NO [ppm]	O ₂ (%)	CO ₂ (%)
case 1			
experiments [82]	0	13.4%	4.3%
simulation, detailed	14.27	12.13	5.23
simulation, reduced	13.92	12.35	5.21
case 2			
experiments [82]	3	14.2%	3.9%
simulation, detailed	18.00	12.93	3.63
simulation, reduced	15.94	12.94	3.63

Table 5.3: Comparison of the measurements and the simulations with detailed and reduced kinetics.

Conclusions

The Eulerian Particle Flamelet Model is able to investigate combustion processes in furnaces with high internal exhaust gas recirculation leading to high residence times.

The detailed chemistry is needed to model transient effects that are not covered by simple combustion models. The results show a good agreement between the experiments and the simulations performed with a detailed and reduced mechanism. This is of particular interest since the reduction of chemical kinetic mechanisms enables to consider a detailed enough chemistry thus saving computational time without losing any important information.

5.2 Simulation of the Combustion in a Pressurised Pulverized Coal Combustion Facility

A test facility for pressurised pulverized coal combustion was constructed 1996 in Aachen by the Lehrstuhl für Wärmeübertragung und Klimatechnik, now Lehrstuhl für Wärme- und Stoffübertragung (Heat and Mass Transfer Institute) at the RWTH Aachen. This facility is used to investigate the coal combustion at different pressures as well as the design of burners and combustion chambers.

Since 1998 experimental investigations are performed in this test facility under various pressures and with different coals. The main focus concerned the processes in the vicinity of the burner like pyrolysis, burnout, gaseous phase reactions and pollutant formation.

The purpose of this work is to apply the Eulerian Particle Flamelet Model presented in section 3.3 and used in section 5.1 to calculate the gaseous phase of the coal combustion. The particularity of this configuration is the fact that the fuel enters the combustion chamber as a solid particle and not already in the gaseous phase as it was investigated with this model until now.

In the following, the experimental set-up and the computational grid will be presented. Afterwards the boundary conditions for the inlets will be given. The way to obtain the coal particle size distribution will also be explained. Finally, the results of the simulation will be compared with experimental data obtained at the Heat and Mass Transfer Institute (see also [2]).

5.2.1 Experimental Set-up

The pressurised pulverized coal combustion facility is presented in detail in [2]. The furnace is represented in Fig. 5.8.

The combustion chamber has a length of 2000mm and a diameter of 400mm. An annular gap between the burner plate and the combustion chamber has a diameter of 10mm. This annular gap is required because of the adjustable burner. A so-called sealing air is introduced through the annulus for cooling, sealing and scavenging.

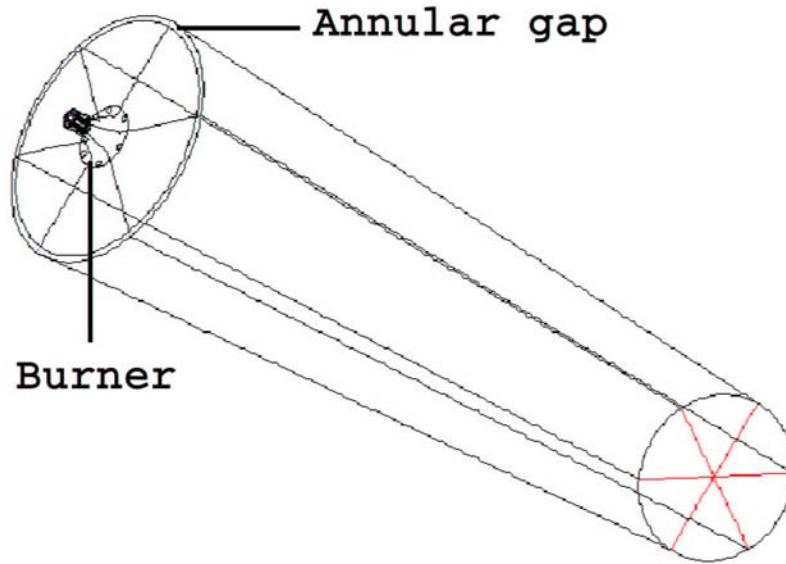


Figure 5.8: Furnace of the pressurised pulverized coal combustion facility.

The burner has three different inlets (see Fig. 5.10). Together with the primary air, a mass flow of 15 kg/h german lignite is fed. Data of the air inlets are given in Table 5.4.

5.2.2 Computational Grid

The three-dimensional mesh used for the simulation calculations represents one sixth of the whole furnace due to the symmetry. It is made of 300000 cells and is limited at the symmetry planes by zones with corresponding periodicity boundary conditions. The 60° sector is shown on Fig. 5.9. Details of the burner with primary, secondary and tertiary inlets can be seen on Fig. 5.10.

The measurements were performed in the plane between two tertiary inlets. It corresponds to the white cut-plane in Fig. 5.11. These measurements were performed at a distance of 30 and 100mm of the burner. It corresponds to the blue lines on Fig. 5.11.

	primary air	secondary air	tertiary air	sealing air
inside diameter [mm]	11	25	-	380
outside diameter [mm]	18	30	9.5	400
velocity axial [m/s]	18.75	21.6	25.51	0.07
velocity radial [m/s]	0	0	0	0
velocity tangential [m/s]	0	35.57	0	0
temperature [K]	313	323	313	313

Table 5.4: Data of the air inlets.

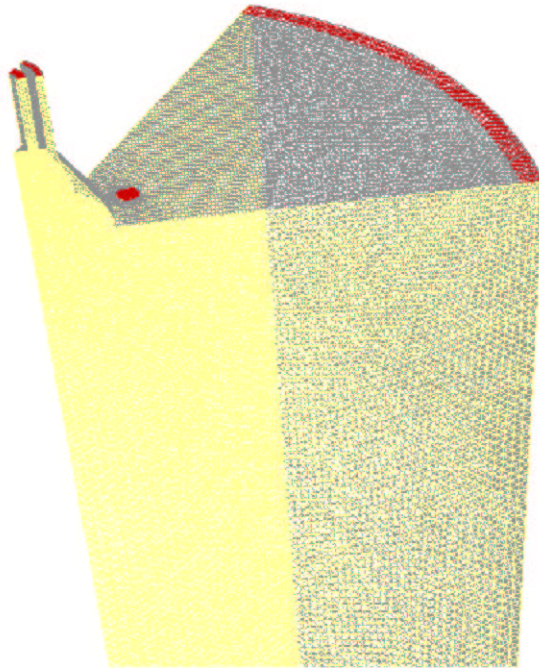


Figure 5.9: Mesh for the 60° sector of the furnace.

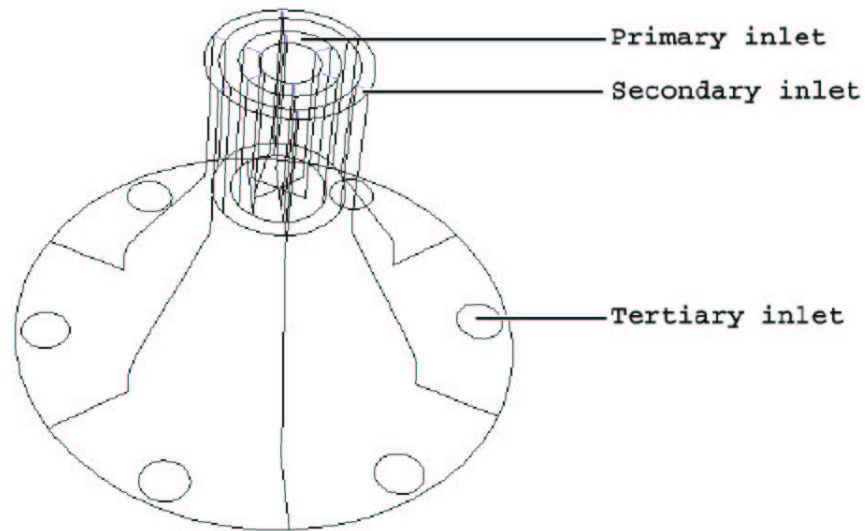


Figure 5.10: Details of the burner.

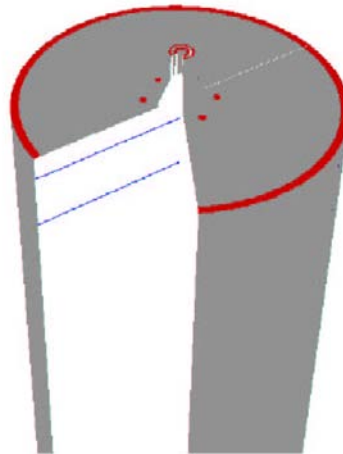


Figure 5.11: Furnace of the pressurised pulverized coal combustion facility. The white cut-planes (between two tertiary inlets) are the planes in which the results are shown. The measurements were performed at a distance of 30 and 100mm of the burner (blue lines).

5.2.3 Comparison with the Experimental Results

Discrete Phase Modeling

A discrete phase is included in FLUENT by defining the initial position, velocity, size and temperature of individual particles. These initial conditions are used to initiate the trajectory calculations that are based on the force balance on the particle using the local continuous phase conditions as the particle moves through the flow.

The general procedure to solve a steady-state discrete-phase problem consists of the following steps:

- Solving the continuous-phase flow
- Creating the discrete-phase injections
- Solving the coupled flow

Coal particle size distribution

For the surface injection, the size distribution is defined by inputting a diameter for the first and last points and the diameter of each particle stream has to be varied. For that purpose, the particle size distribution can be easily defined by fitting the size distribution data to the Rosin-Rammler equation. In this approach, the complete range of particle sizes is divided into a set of discrete size ranges, each to be defined by a single stream that is part of the injection. The particle size analysis is given in Table 5.5 and represented in Fig. 5.12.

The Rosin-Rammler distribution function is based on the assumption that an exponential relationship exists between the particule diameter, d , and the mass fraction of particles with diameter greater than d , Y_d :

$$Y_d = e^{-(d/\bar{d})^n}, \quad (5.2)$$

where \bar{d} is the mean diameter and n the spread diameter. To determine these input parameters, the given particle size data is processed (Table 5.5 and Fig. 5.12). The mean diameter has the value $19.19 \mu\text{m}$ and the spread diameter is 1.1. It follows the cumulative size distribution of particles shown in Fig. 5.13.

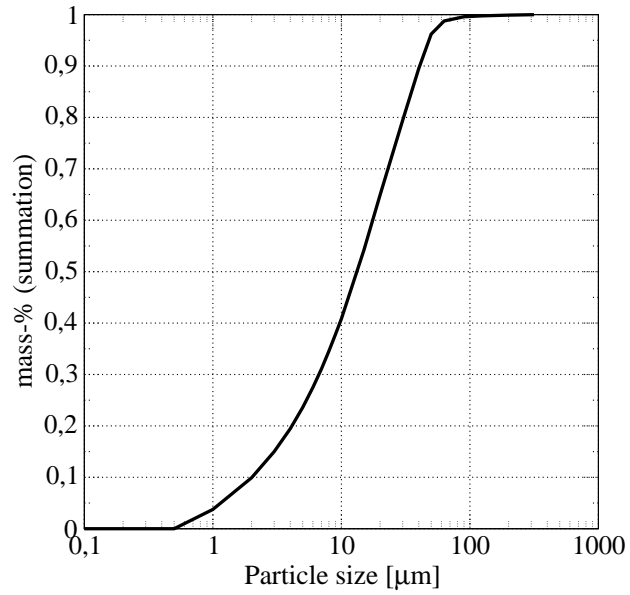


Figure 5.12: Particle size distribution.

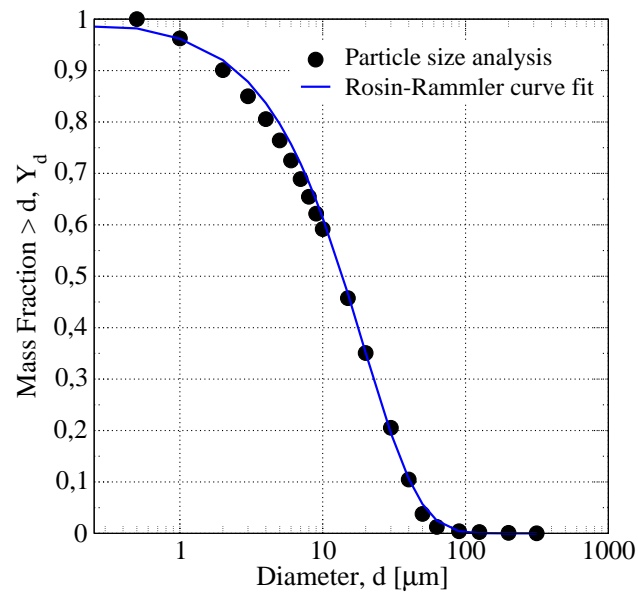


Figure 5.13: Rosin-Rammler cumulative size distribution of particles.

μm	mass.-%
0	0.0000
0.5	0.0000
1	0.0375
2	0.0992
3	0.1500
4	0.1945
5	0.2359
6	0.2748
7	0.3110
8	0.3455
9	0.3783
10	0.4083
15	0.5426
20	0.6493
30	0.7947
40	0.8953
50	0.9621
63	0.9875
90	0.9958
125	0.9975
200	0.9990
315	0.9999

Table 5.5: Particle size analysis (pulverized lignite)

The models presented in section 4.4 are applied for the calculation of the coal combustion (pyrolysis and burnout). These models are quite simplified but deliver good enough results. In order to achieve better results concerning the behaviour of the coal during combustion, more complex models are available (see [2]). The aim of this work was to include the flamelet concept into this configuration, it especially concentrates on the gaseous phase.

Devolatilization and Char Burnout

Fig. 5.14 shows that volatiles are released when the coal travels about one tenth of the combustion chamber length. The onset of devolatilization occurs when the coal temperature reaches the specified value of 400 K.

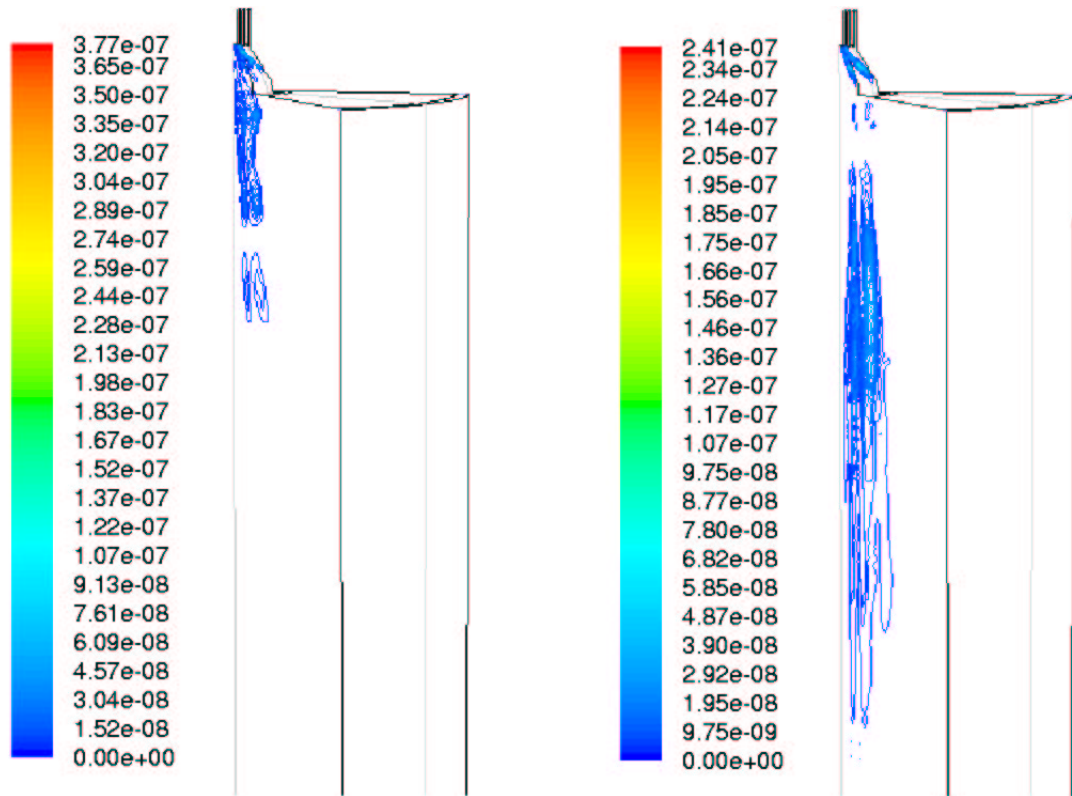


Figure 5.14: Devolatilization (l.h.s.) and char burnout rate (r.h.s.).

The char burnout occurs after complete devolatilization. Fig. 5.14 also shows that burnout is complete at about one third of the furnace length.

Fig. 5.15 shows the trajectories of the particle stream colored by particle residence time.

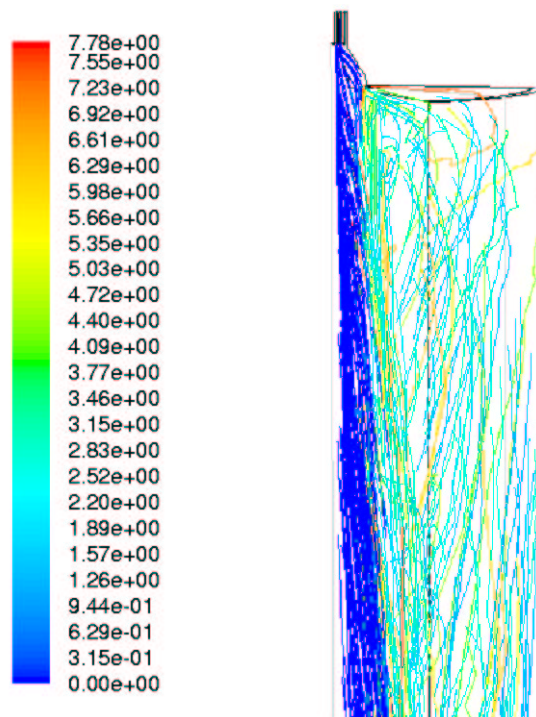


Figure 5.15: Trajectories of the particle stream colored by particle residence time.

Initialization of the calculation for the gaseous phase

Contrary to the usual initialization where the fuel is a gas with a well-defined composition, the fuel during the coal combustion first enters the combustion chamber as a solid coal particle, from which volatiles escape during the pyrolysis. The initialization of the Eulerian Particle Flamelet Model has to take these volatiles into account and the initialization of the (gaseous) fuel is not made at the fuel inlet anymore but in the combustion chamber where volatiles appear. However the composition of the volatiles is not well-defined: it depends on the coal and the boundary conditions (pressure for example). Some data can be found in the literature. Table 5.6 gives the composition of the volatiles escaped during the pyrolysis of the coal at 1 bar [57]. It will be used for the calculation (the calculations are performed at 3 bar; nevertheless, it was noticed in [2] that the increase of the pressure from 1 to 15 bar only slightly modifies the relative distribution of the released species). The initial mass fraction profiles are plotted on Fig. 5.16 in the mixture fraction space.

Species	Mole Fraction
CH ₄	0.19
H ₂	0.30
CO	0.22
CO ₂	0.29

Table 5.6: Composition of the volatiles escaped from the coal at 1 bar [57].

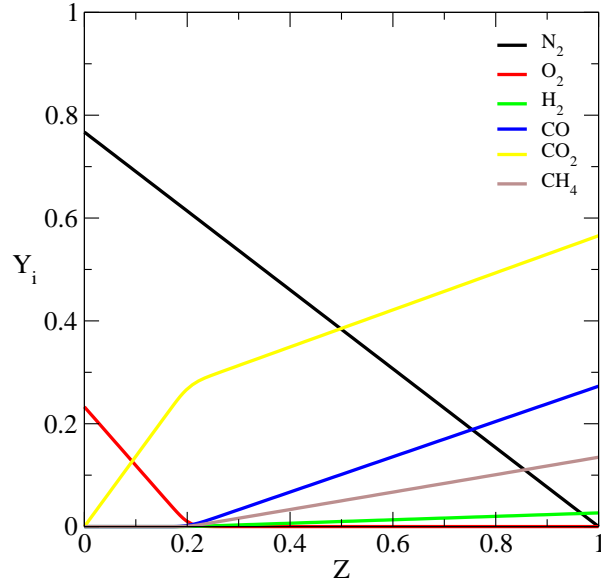


Figure 5.16: Initial mass fraction profiles in the mixture fraction space.

Velocity profiles

Figs. 5.18 and 5.19 show the axial velocity profiles at a distance of 30 and 100mm from the burner. The simulation gives a very good prediction of the axial velocity at both distances.

The tangential velocity at 30 and 100mm is represented on Figs. 5.20 and 5.21. The computed values are in agreement with the measurements. However the maximum of the tangential velocity at 30mm is underpredicted, due to the use of the $k - \epsilon$ model.

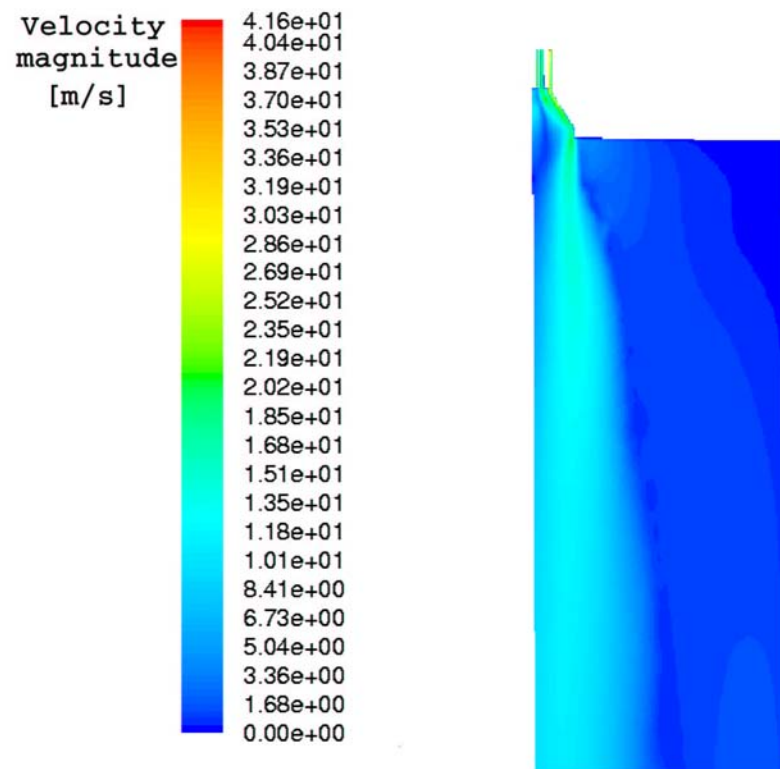


Figure 5.17: Velocity magnitude predicted by the simulation in the plane between two tertiary inlets.

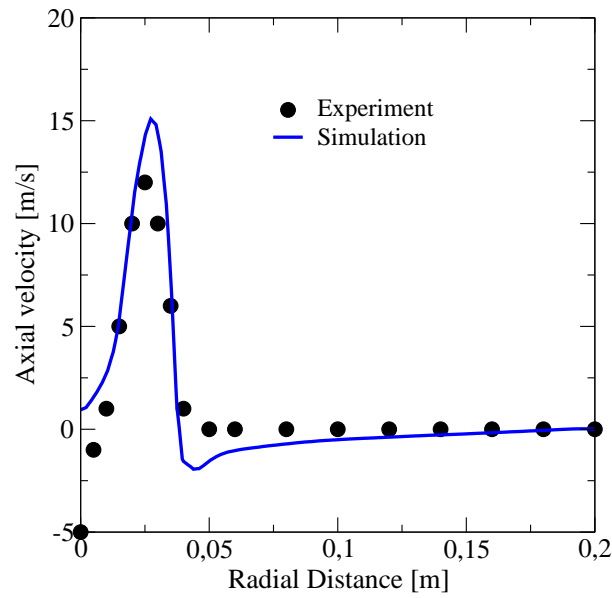


Figure 5.18: Comparison of the axial velocity predicted by the simulation with the experimental data at a distance of 30mm from the burner.

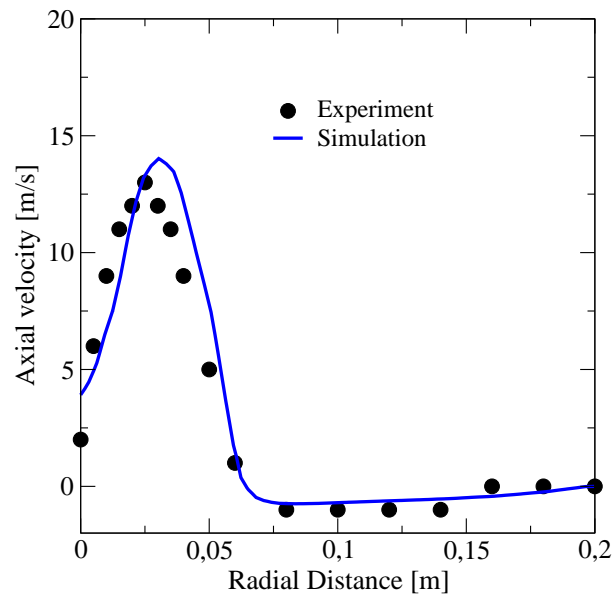


Figure 5.19: Comparison of the axial velocity predicted by the simulation with the experimental data at a distance of 100mm from the burner.

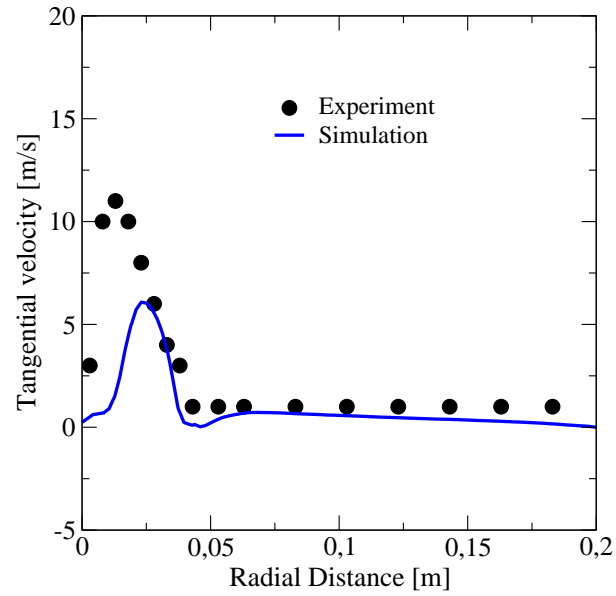


Figure 5.20: Comparison of the tangential velocity predicted by the simulation with the experimental data at a distance of 30mm from the burner.

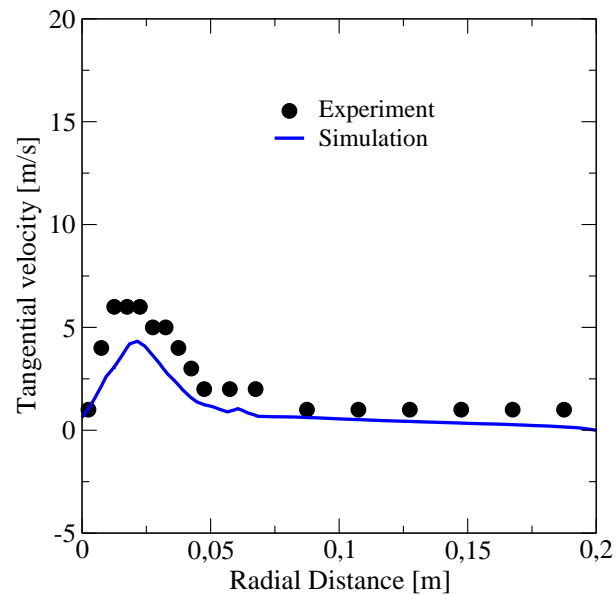


Figure 5.21: Comparison of the tangential velocity predicted by the simulation with the experimental data at a distance of 100mm from the burner.

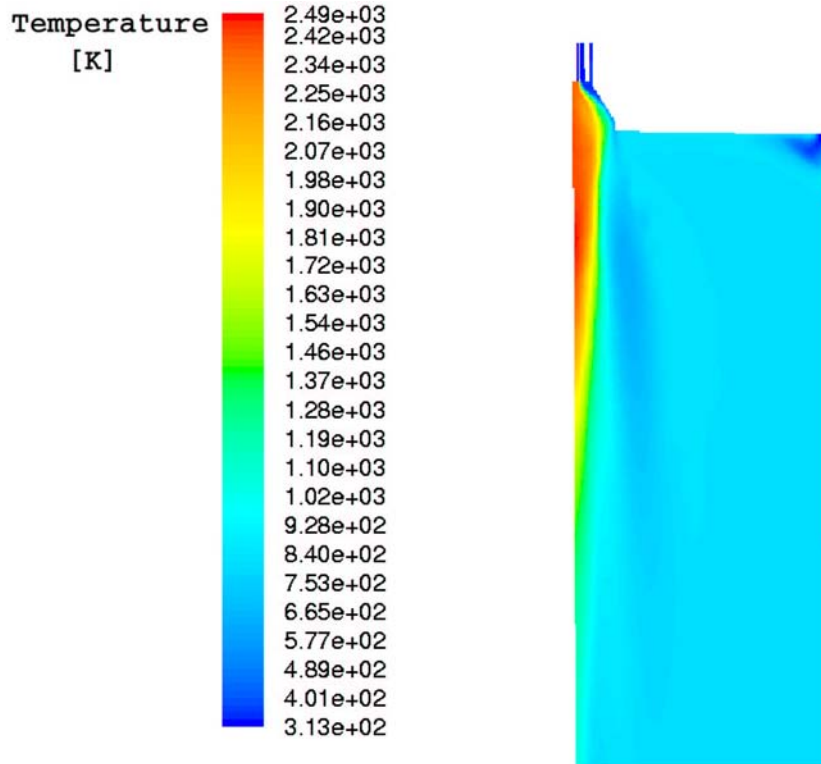


Figure 5.22: Temperature predicted by the simulation in the cut-plane between two tertiary inlets.

Temperature profiles

The temperature predicted by the simulation in the cut-plane between two tertiary inlets is shown in Fig. 5.22.

In order to be able to compare the temperature measured by a thermoelement at 30mm from the burner, the temperature profile was corrected in regard of the radiation (see [2]). The comparison between the calculated and measured temperature (Fig. 5.23) shows a quite good agreement, even if the simulation does not capture the influence of the cold tertiary air at about 45mm.

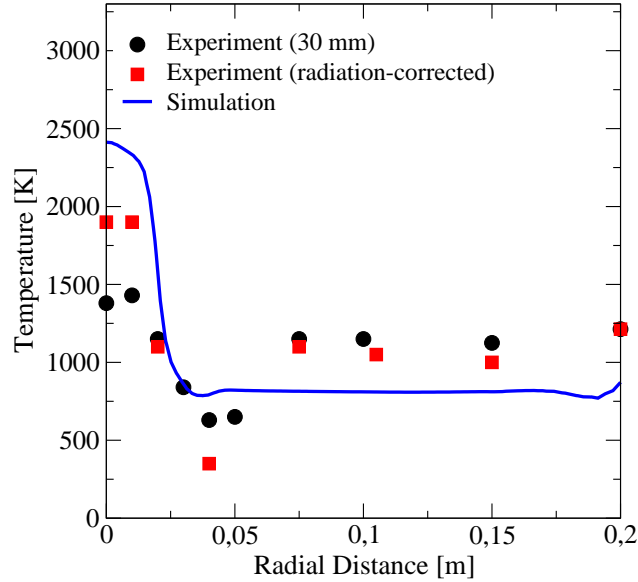


Figure 5.23: Comparison of the temperature predicted by the simulation with the experimental data at a distance of 30mm from the burner.

O₂ and CO₂ profiles

The profiles of the O₂ mole fraction are plotted on Figs. 5.24 and 5.25. The computed mole fraction has the same trend at both distances from the burner compared to the experimental data: it is underpredicted in the vicinity of the axis of the combustion chamber and higher than the measured values between 0.03 and 0.2 m. However, the results of the simulation are satisfactory.

Figs. 5.27 and 5.28 show the profiles of the CO₂ mole fraction at a distance of 30 and 100mm from the burner. The simulation delivers very good results compared to the experimental data. A small difference in the profiles can be noticed at about 40mm. This may be due to the influence of the cold air from the tertiary air that is not well captured by the simulation.

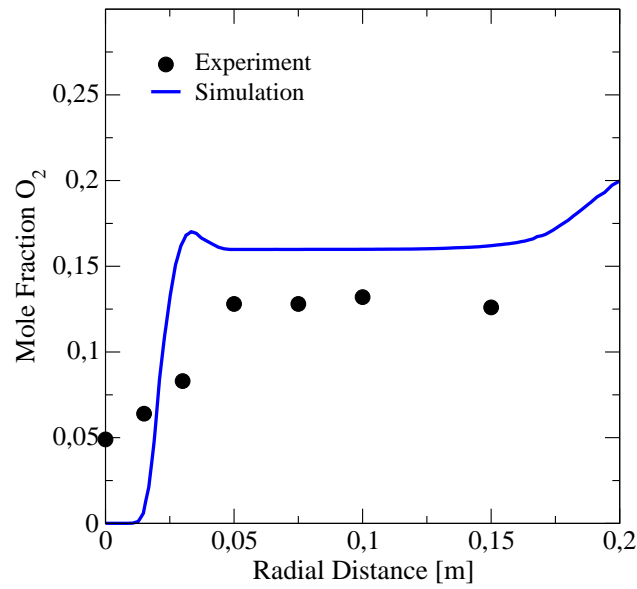


Figure 5.24: Comparison of the O_2 mole fraction predicted by the simulation with the experimental data at a distance of 30mm from the burner.

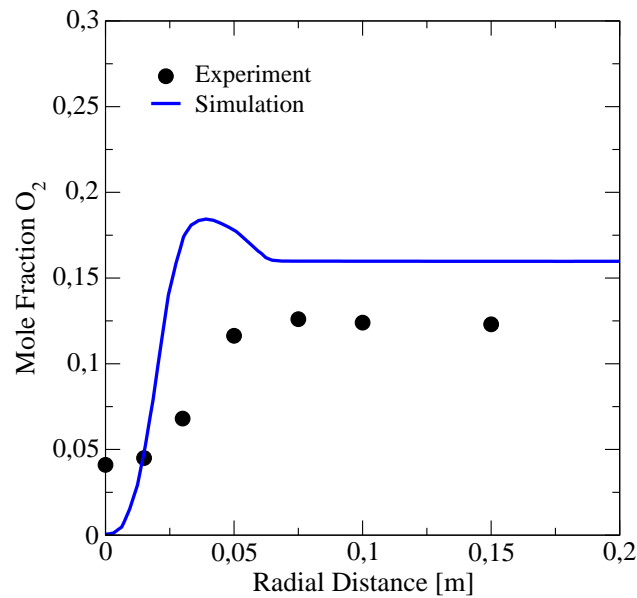


Figure 5.25: Comparison of the O_2 mole fraction predicted by the simulation with the experimental data at a distance of 100mm from the burner.

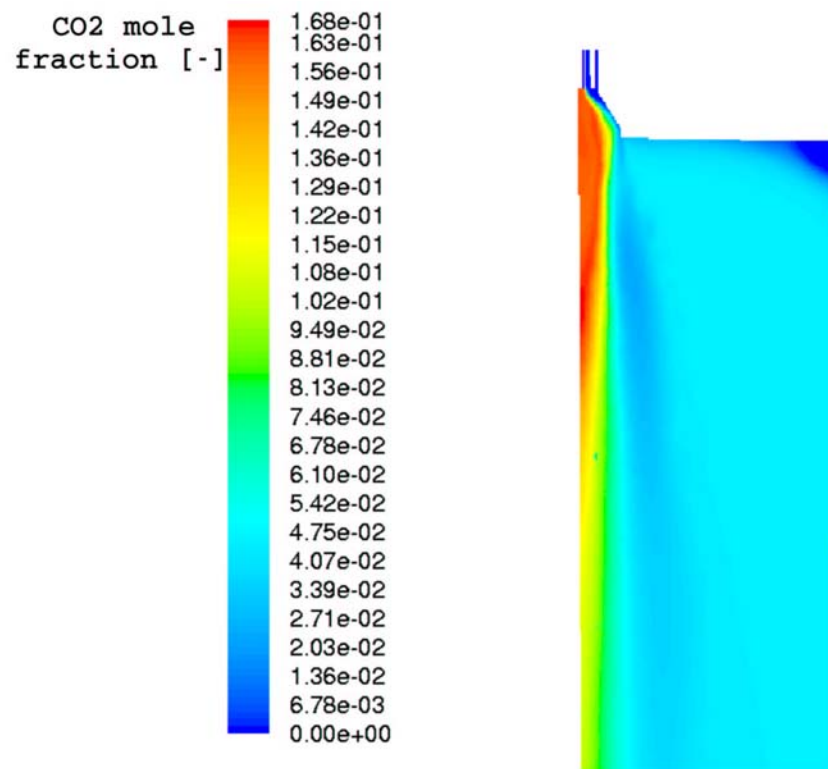


Figure 5.26: CO₂ mole fraction predicted by the simulation in the cut-plane between two tertiary inlets.

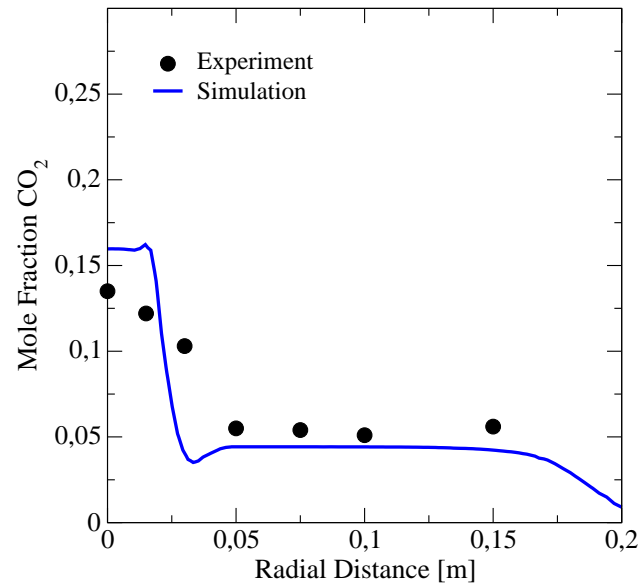


Figure 5.27: Comparison of the CO₂ mole fraction predicted by the simulation with the experimental data at a distance of 30mm from the burner.

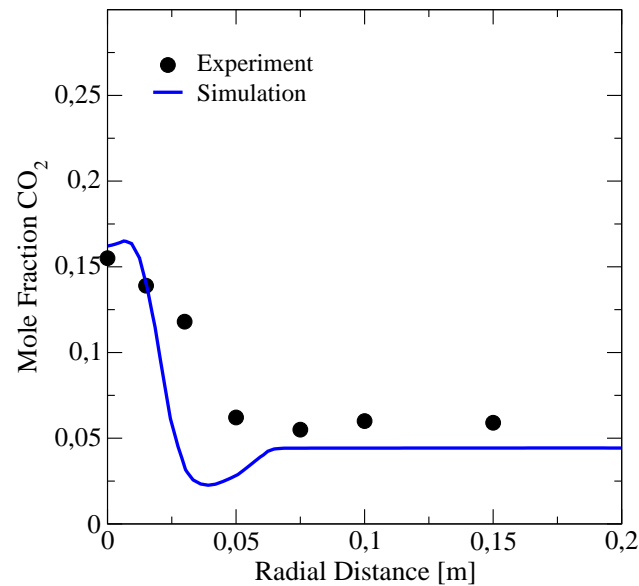


Figure 5.28: Comparison of the CO₂ mole fraction predicted by the simulation with the experimental data at a distance of 100mm from the burner.

Remark: In order to investigate the influence of the initial composition of the volatiles, further numerical simulations were performed with another initial composition of the volatiles (taken from the results of the simulation of [2], corresponding to the experimental data of [57] used above). The results comparing these two cases are shown in Appendix D and demonstrates that the choice of the initial composition of the volatiles does not have so much influence on the final results. The differences between the two cases are situated at the axis of the furnace, where the gaseous phase is initiated (for this burner configuration).

Simulation with Reduced Chemistry

The same numerical calculation was performed with the reduced mechanism developed in section 4.3.2 and applied in section 5.1. The aim of this section is to show that the Eulerian Particle Flamelet Model can be used with a reduced chemistry also to calculate the gaseous phase in the coal combustion. The results of this simulation are compared with the experimental data and with the simulation with the detailed chemistry. The comparisons for temperature, O_2 and CO_2 mole fractions at 30 and 100mm from the burner are shown in Figs. (5.29) to (5.33).

In all the cases, there is a total agreement between the results with the detailed and the reduced chemistry. Only for the mole fraction of CO_2 , a slight difference at the axis can be seen for the case at 30mm from the burner.

These results outline that the Eulerian Particle Flamelet Model can be applied in the numerical simulation of combustion processes with detailed chemistry required for the consideration of unsteady effects. The use of reduced chemistry is also possible and enables to produce good results and save computational time.

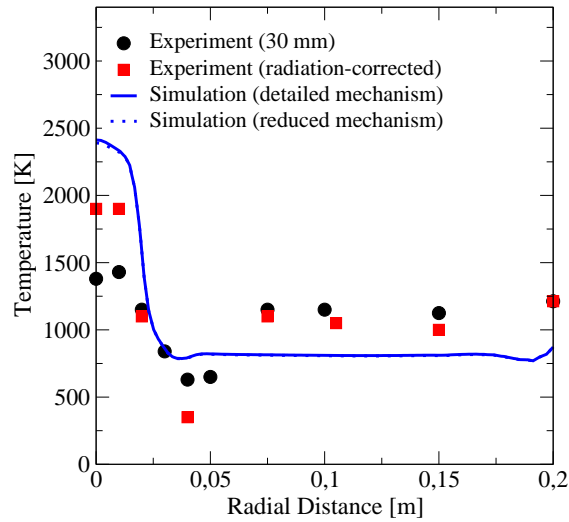


Figure 5.29: Comparison of the temperature predicted by the simulation (line = detailed chemistry; dotted line = reduced chemistry) with the experimental data at a distance of 30mm from the burner.

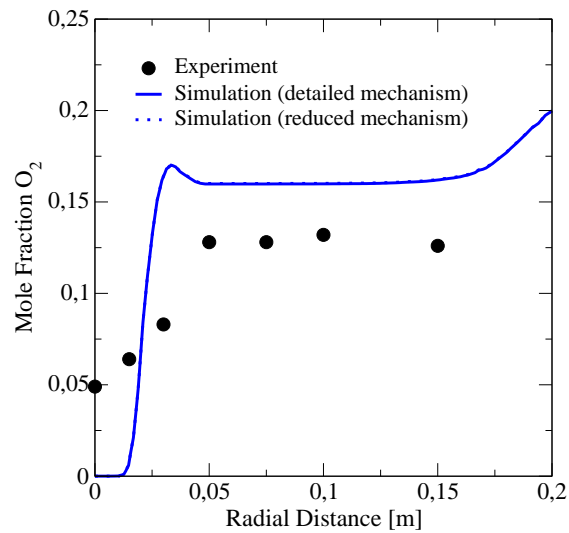


Figure 5.30: Comparison of the O₂ mole fraction predicted by the simulation (line = detailed chemistry; dotted line = reduced chemistry) with the experimental data at a distance of 30mm from the burner.

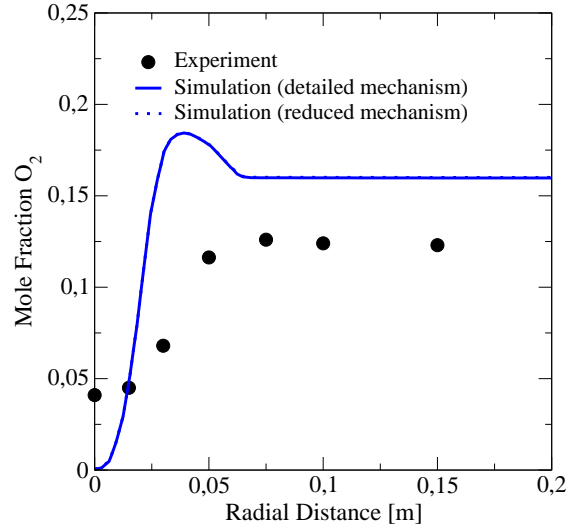


Figure 5.31: Comparison of the O_2 mole fraction predicted by the simulation (line = detailed chemistry; dotted line = reduced chemistry) with the experimental data at a distance of 100mm from the burner.

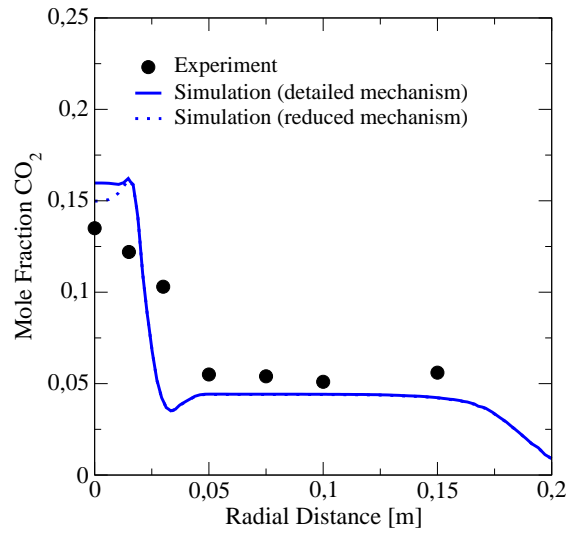


Figure 5.32: Comparison of the CO_2 mole fraction predicted by the simulation (line = detailed chemistry; dotted line = reduced chemistry) with the experimental data at a distance of 30mm from the burner.

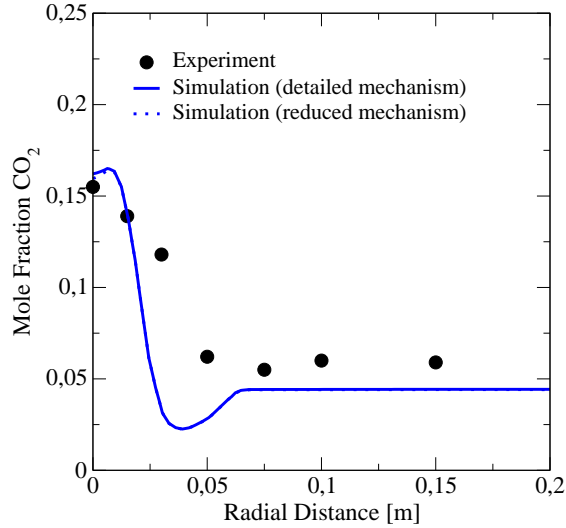


Figure 5.33: Comparison of the CO₂ mole fraction predicted by the simulation (line = detailed chemistry; dotted line = reduced chemistry) with the experimental data at a distance of 100mm from the burner.

Conclusions

It is well-known that the flamelet model delivers very good results in the simulation of combustion processes in the gaseous phase. In this work, the Eulerian Particle Flamelet Model was applied to the simulation of the gaseous phase during the coal combustion. Even if quite simplified models are used for the pyrolysis and the char burnout, the final results are in good agreement with the experimental data. In the case of 2 phases (solid coal particle and volatiles), the composition of the volatiles has to be assumed (such data are available in the literature).

The good results obtained in this work with the Eulerian Particle Flamelet Model confirms the ability of the flamelet model to simulate combustion processes.

Chapter 6

Summary and Conclusions

One of the purposes of numerical simulations of combustion processes consists in obtaining accurate predictions. For a good modelling accuracy of the chemistry, a detailed reaction mechanism is taken into account. Nevertheless this implies rather long computational times. A way to overcome this problem is the use of reduced chemical mechanisms enabling good simulation results in a shorter time without losing accuracy.

In this work, kinetic mechanisms for model fuels were developed in order to simulate the complex physico-chemical interactions in practical combustion systems. A methane mechanism with a detailed NO_x chemistry has been assembled and validated against a wide range of combustion regimes (laminar premixed flames, shock tube, ...). This detailed reaction mechanism was reduced by the traditional method of steady-state assumptions, explained as well. The obtained 19-step mechanism was also validated against experimental data from the literature and shows good agreement with these data and with the results obtained by using the detailed chemistry.

The Representative Interactive Flamelet (RIF) model and its expansion for the application of unsteady flamelets in steady processes were presented. Both detailed and reduced mechanisms for methane were implemented. This model was first applied to the numerical simulation of a MILD combustor. The use of a detailed and a reduced mechanism in the simulation led to about the same results and a good agreement with the experimental results could be obtained. The temperature-dependence of the NO_x formation could be noticed. The NO_x predictions were higher than the measurements

due to the slightly higher predicted temperature but nevertheless always in the right order of magnitude, either with the detailed or with the reduced chemistry, thus showing the advantage of reducing chemical mechanisms for CFD applications.

Numerical simulation of a pressurised pulverized coal combustion was then performed. The used pyrolysis and burnout models for the solid coal particle were presented. These quite simple models enable to capture the main features of the coal combustion (for a deeper understanding and description of these processes, there exist more complex models, but it is not the purpose of this work). Special attention was paid to the gaseous phase which was calculated with the Representative Interactive Flamelet model, applying here again the detailed and the reduced mechanisms. The results for the temperature and species concentrations are in agreement with the experimental results delivered by the Institute of Heat and Mass Transfer (Lehrstuhl für Wärme- und Stoffübertragung Aachen).

Those results underline the capability of simulating combustion processes with low-emission by using a detailed and/or a reduced mechanism.

Bibliography

- [1] Fluent Inc., FLUENT 6.2 Documentation, 2005.
- [2] A. Ayar. *Modellierung der Pyrolyse in einer Kohlenstaub-Druckfeuerung*. PhD thesis, RWTH Aachen, 2003.
- [3] S. Badzioch and P.G.W Hawskey. Kinetics of thermal decomposition of pulverized coal particles. *Ind. Eng. Chem. Process Des. Dev.*, 9:521–530, 1970.
- [4] R. S. Barlow and J.-Y. Chen. On transient flamelets and their relationship to turbulent methane-air jet flames. *Proc. Combust. Inst.*, 24:231–237, 1992.
- [5] H. Barths, C. Antoni, and N. Peters. Three-Dimensional Simulation of Pollutant Formation in a DI-Diesel Engine Using Multiple Interactive Flamelets. *Paper No. SAE 982459*, 1998.
- [6] H. Barths, H. Pitsch, and N. Peters. 3-D Simulation of DI Diesel Combustion and Pollutant Formation Using a Two-Component Reference Fuel. In *Oil & Gas and Technology-Rev*, volume 54, pages 23–244. IFP, 1999.
- [7] D. L. Baulch, C. J. Cobos, R. A. Cox, P. Frank, G. Hayman, Th. Just, J. A. Kerr, T. Murrells, M. J. Pilling, J. Troe, R. W. Walker, and J. Warnatz. Summary table of evaluated kinetic data for combustion modelling: Supplement. *Combust. Flame*, 98:59–79, 1994.
- [8] D. L. Baulch, C. J. Cobos, R. A. Cox, P. Frank, G. Hayman, Th. Just, J. A. Kerr, T. Murrells, M. J. Pilling, J. Troe, R. W. Walker, and J. Warnatz. Evaluated kinetic data for combustion modeling. *J. Phys. Chem. Ref. Data*, 21:411–429, 1992.

-
- [9] M. M. Baum and P.J. Street. Predicting the combustion behavior of coal particles. *Combustion Science and Technology*, 3:231–243, 1971.
 - [10] A.B. Bendtsen, P. Glarborg, and K. Dam-Johansen. *Combust. Sci. and Tech.*, 151:31–71, 2000.
 - [11] L. Bergmann, C. Schaefer, and H. Niedrig. *Lehrbuch der Experimentalphysik, Band 3, Optik und Atomphysik 1. Teil: Wellenoptik*. Gruyter, 1993.
 - [12] G. Bikas. *Kinetic Mechanisms for Hydrocarbon Ignition*. PhD thesis, RWTH Aachen, 2001.
 - [13] G. Bikas and N. Peters. Kinetic Modelling of n-Decane Combustion and Autoignition. *Combustion and Flame*, (126):1456–1475, 2001.
 - [14] R.W. Bilger. The structure of diffusion flames. *Combust. Sci. and Tech.*, 13:155–170, 1976.
 - [15] M. Bollig. *Berechnung laminarer Kohlenwasserstoffflammen im Hinblick auf die Stickoxidbildung in Verbrennungsmotoren*. PhD thesis, RWTH Aachen, 1998.
 - [16] J. Boussinesq. Théorie de l’écoulement tourbillant. *Mem. présentés par divers Savants Acad. Sci. Inst. Fr.*, 23:46–50, 1877.
 - [17] S.P. Burke and T.E.W. Schumann. Diffusion flames. In *Proc. Combust. Inst.*, volume 1, pages 2–11. The Combustion Institute, Pittsburgh, 1928.
 - [18] A. Cavaliere and M. de Joannon. Mild combustion. In *Proc. Energy Combust. Sci.*
 - [19] M. Chen. *Simulation of Flame Stabilization in Lifted Turbulent Jet Diffusion Flames*. PhD thesis, RWTH Aachen, 2000.
 - [20] H. J. Curran, P. Gaffuri, P. Pitz, and C. K. Westbrook. *Combust. Flame*, 114:149–177, 1998.
 - [21] B.B. Dally, A.N. Karpetis, and R.S. Barlow. Structure of turbulent non-premixed jet flames in a diluted hot coflow. *Proc. Comb. Inst.*, 29:1147–1154, 2002.

-
- [22] B.B. Dally, E. Riesmeier, and N. Peters. Effect of fuel mixture on mild combustion. *Comb. Flame*, 137:418:431, 2004.
- [23] C. Douté, J.-L. Delfau, R. Akrich, and C. Vovelle. Chemical structure of atmospheric pressure premixed n-decane and kerosene flames. *Combust. Sci. Technol.*, 103:153, 1995.
- [24] E. Effelsberg and N. Peters. Scalar dissipation rates in turbulent jets and jet diffusion flames. *Proc. Combust. Inst.*, 22:693–700, 1988.
- [25] G. M. Faeth. Evaporation and combustion of sprays. *Prog. Energy Combust. Sci.*, 9:1–76, 1983.
- [26] M. A. Field. Rate of combustion of size-graded fractions of char from a low rank coal between 1200-2000k. *Combust. Flame*, 13:237–252, 1969.
- [27] A. Frank, K. A. Bhaskaran, and Th Just. *Twenty-First Symposium (International) on Combustion*.
- [28] P. Glarborg, K. Dam-Johansen, J.A. Miller, and R.J. Kee. *Int. J. Chem. Kinetics*, 26:421–436, 1994.
- [29] K. Görner. *Technische Verbrennungssysteme, Grundlagen, Modellbildung, Simulation*. Springer Verlag, 1991.
- [30] C. Hasse, S. Vogel, and N. Peters. Modeling of a daimlerchrysler truck engine using an Eulerian spray model. In *13th International Multidimensional Engine Modeling User's Group Meeting*. Cray Inc, 2003.
- [31] T. Hellström. RIF implementation and testing. Technical Report 01.07.1996-31.12.1996, Diesel, Technical Report, 1997.
- [32] M. Herrmann. *Numerical Simulation of Premixed Turbulent Combustion Based on a Levet Set Flamelet Model*. PhD thesis, RWTH Aachen, 2001.
- [33] H. C. Hewson and M. Bollig. Reduced mechanisms for no_x emissions from hydrocarbon diffusion flames. In *Proc. Combust. Inst.*, volume 26, pages 2171–2180. The Combustion Institute, Pittsburgh, 1996.
- [34] J. C. Hewson. . PhD thesis, University of California at San Diego, 1997.
- [35] IEA. <http://www.iea.org>, 2007.

-
- [36] A. S. Jamaluddin, J.S. Truelove, and T. F. Wall. Modelling of coal devolatilization and its effect on combustion calculations. *Combust. Flame*, 62:85–89, 1985.
- [37] M. De Joannon, G. Langella, F. Beretta, A. Cavaliere, and C. Noviello. Mild combustion: Process features and technological constraints. In *Proceedings of the Mediterranean Combustion Symposium*, pages 347–360. Mediterranean Combustion Symposium, 1999.
- [38] W. P. Jones. Turbulence modeling and numerical solution methods for variable density and combustng flows. In P. A. Libby and F. A. Williams, editors, *Turbulent Reacting Flows*, pages 309–374. Academic Press, 1994.
- [39] W. P. Jones and B. E. Launder. The prediction of laminarization with a two-equation model of turbulence. *Int. J. Heat Mass Transfer*, pages 301–314, 1972.
- [40] W. P. Jones and Y. Prasetyo. Probability density function modeling of premixed turbulent opposed jet flames. *Proc. Combust. Inst.*, 26:275–282, 1996.
- [41] W. P. Jones and J. H. Whitelaw. Calculation Methods for Reacting Turbulent Flows: A Review. *Combust. Flame*, pages 1–26, 1982.
- [42] D. Keller and N. Peters. Transient pressure effects in the evolution equation for premixed turbulent flames. *Theoret. Comput. Fluid Dynamics*, 6:141–159, 1994.
- [43] H. Kobayashi, J. B. Howard, and A.F. Sarofim. Coal devolatilization at high temperatures. In *Proc. Combust. Inst.*, volume 16, pages 411–425. The Combustion Institute, Pittsburgh, 1976.
- [44] A. N. Kolmogorov. The local structure of turbulence in incompressible viscous fluids for very large reynolds numbers. *Doklady Akademii Nauk SSSR*, 30:301–305, 1941.
- [45] A. N. Kolmogorov. The equations of turbulent motion in an incompressible fluid. *Izvestia Acad. Sci. USSR Phys.*, 6:56–58, 1942.

-
- [46] K. K. Y. Kuo. Principles of combustion. *John Wiley and sons, New York*, 1986.
- [47] V. R. Kuznetsov. Effect of turbulence on the formation of large superequilibrium concentration of atoms and radicals in diffusion flames. *Mehan. Zhidkosti Gasa*, 6:3–9, 1982.
- [48] B. E. Launder and B. I. Sharma. *Lectures in Mathematical Models of Turbulence*. Academic Press, London, England, 1972.
- [49] B. E. Launder and B. I. Sharma. Application of the energy-dissipation model of turbulence to the calculation of flow near a spinning disc. *Lett. Heat Mass Transf.*, 1:131–138, 1974.
- [50] G.A. Lavoie, J.B. Heywood, and J.C. Keck. *Combust. Sci. Technol.*, 1:313–326, 1970.
- [51] K. M. Leung and R. P. Lindstedt. Detailed kinetic modeling of $C_1 - C_3$ alkane diffusion flames. *Combust. Flame*, 102:129–160, 1995.
- [52] S. K. Liew, K. N. C. Bray, and J. B. Moss. A stretched laminar flamelet model of turbulent nonpremixed combustion. *Combust. Flame*, 56:199–213, 1984.
- [53] A. Liñán. The asymptotic structure of counterflow diffusion flames for large activation energies. *Acta Astronautica*, 1:1007, 1974.
- [54] M.W. Markus, P. Roth, and Th. Just. *Int. J. Chem. Kinetics*, 28:171, 1996.
- [55] F. Maus. *Entwicklung eines kinetischen Modells der Rußbildung mit schneller Polymerisation*. PhD thesis, RWTH Aachen, 1997.
- [56] F. Mauss, D. Keller, and N. Peters. A lagrangian simulation of flamelet extinction and re-ignition in turbulent jet diffusion flames. In *Proc. Combust. Inst.*, volume 23, pages 693–698. The Combustion Institute, Pittsburgh, 1990.
- [57] C.J. Mill. *Pyrolysis of Fine Coal Particles at High Heating Rate and Pressure*. PhD thesis, University of New South Wales, Australia, 2000.

-
- [58] J. A. Miller and C. T. Bowman. *Prog. Energy Combust. Sci.*, 15:287–338, 1989.
- [59] J. A. Miller and C. F. Melius. Kinetic and thermodynamic issues in the formation of aromatic compounds in flames of aliphatic fuels. *Combust. Flame*, 91:21–39, 1992.
- [60] U. C. Müller. Der Einfluß von Strahlungsverlusten auf die thermische NO-bildung in laminaren CO-H₂-Diffusionsflammen. Master’s thesis, RWTH Aachen, 1989.
- [61] OXYCOAL-AC. <http://www.oxycoal.de>, 2007.
- [62] I.B. Özdemir and N. Peters. Characteristics of the reaction zone in a combustor operating at mild combustion. *Experiments in Fluids*, 30:683–695, 2001.
- [63] N. Peters. Local quenching of diffusion flamelets and non-premixed turbulent combustion. In *Spring Meeting*, Paper No. WSS 80-4 92-109. The Combustion Institute/Western States Section, Irvine, CA, 1980.
- [64] N. Peters. Laminar diffusion flamelet models in non-premixed turbulent combustion. *Prog. Energy Combust. Sci.*, 10:319–339, 1984.
- [65] N. Peters. Laminar flamelet concepts in turbulent combustion. *Proc. Combust. Inst.*, 21:1231–1250, 1986.
- [66] N. Peters. Length scales in laminar and turbulent flames. *IAA journal, Numerical Approaches to Combustion Modeling*, 135:155–182, 1991.
- [67] N. Peters. Fifteen Lectures on Laminar and Turbulent Combustion. Technical report, Ercoftac Summer School, RWTH Aachen, 1992.
- [68] N. Peters. *Turbulent Combustion*. Cambridge University Press, 2000.
- [69] H. Pitsch. *Modellierung der Zündung und Schadstoffbildung bei der dieselmotorischen Verbrennung mit Hilfe eines interaktiven Flamelet-Modells*. PhD thesis, RWTH Aachen, 1997.
- [70] H. Pitsch, H. Barths, and N. Peters. Three-Dimensional Modeling of NO_x and Soot Formation in DI-Diesel Engines Using Detailed Chemistry Based on the Interactive Flamelet Approach. *Paper No. SAE 962057*, 1996.

-
- [71] H. Pitsch, M. Bollig, J. Göttgens, P. Terhoeven, and G. Bikas. FlameMaster, A Computer Code for Homogeneous and One-Dimensional Laminar Flame Calculations. Technical report, Institut für Technische Mechanik, RWTH Aachen.
- [72] H. Pitsch, M. Chen, and N. Peters. Unsteady flamelet modeling of turbulent hydrogen-air diffusion flames. In *Proc. Combust. Inst.*, volume 27, pages 1057–1064. The Combustion Institute, Pittsburgh, 1998.
- [73] H. Pitsch and N. Peters. Reduced kinetics of multicomponent fuels to describe the auto-ignition, flame propagation and post flame oxidation of gasoline and Diesel fuels. Technical report, IDEA EFFECT, 1996.
- [74] H. Pitsch and N. Peters. A consistent flamelet formulation for non-premixed combustion considering differential diffusion effects. *Combust. Flame*, 114:26–40, 1998.
- [75] S. B. Pope. *Turbulent Flows*. Cambridge University Press, Cambridge, U. K., 2000.
- [76] L. Prandtl. Über die ausgebildete Turbulenz. *ZAMM*, 5:136–139, 1925.
- [77] E. Riesmeier. *Numerische Simulation der Verbrennungsprozesse in Gasturbinen- und MILD-Brennkammern*. PhD thesis, RWTH Aachen, 2004.
- [78] E. Riesmeier and N. Peters. Investigation of pollutant formation and stability effects in mild combustion using the eulerian particle flamelet model. *Proceedings of the European Combustion Meeting 2003*.
- [79] D. J. Seery and C. T. Bowman. *Combustion and Flame*, 14:37, 1970.
- [80] G. P. Smith, D. M. Golden, M. Frenklach, N. W. Moriarty, B. Eiteneer, M. Goldenberg, C. T. Bowman, R. K. Hanson, S. Song, W. C. Gardiner Jr., V. V. Lissianski, and Z. Qin. Gri-mech 3.0. Technical report, http://www.me.berkeley.edu/gri_mech, 1999.
- [81] L. J. Spadaccini and M. B. Colket. Ignition delays in $\text{ch}_4\text{-o}_2$ and $\text{ch}_4\text{-c}_2\text{h}_6\text{-o}_2$ mixtures. *Prog. Energy Combust. Sci.*, 20:431, 1994.

-
- [82] K.-D. Stoehr. Detailed Description of Interaction of Turbulence and Reaction for the FLOX[®] Combustion System. Technical report, Deliverable Report (D3), NGT, 2004.
- [83] H. Tennekes and J. L. Lumley. *A First Course in Turbulence*. MIT Press, 1972.
- [84] H. Tsuji. . *Prog. Energy Combust. Sci.*, 8:93, 1982.
- [85] S.K. Ubhayakar, D.B. Stickler, C.W.V. Rosenberg, and R.E. Gannon. Rapid devolatilization of pulverized coal in hot combustion gases. *16th Symposium (International) on Combustion, The Combustion Institute*, 16:427–436, 1977.
- [86] UNFCCC. http://unfccc.int/kyoto_protocol/items/2830.php.
- [87] C. N. Vagelopoulos and F. N. Egolfopoulos. Direct experimental determination of laminar flame speeds. Paper WSS/CI 97S-022. Combustion Institute Meeting/Western States Section, Livermore, CA, 1997.
- [88] J. Vandooren, J. Bian, and P.J. Tiggelen. *Combust. Flame*, 98:402–410, 1994.
- [89] J. Warnatz, U. Maas, and R. W. Dibble. *Combustion- Physical and Chemical Fundamentals, Modeling and Simulation, Experiments, Pollutant Formation-*. Springer-Verlag, Berlin, Heidelberg, 1996.
- [90] F. A. Williams. Recent advances in theoretical descriptions of turbulent diffusion flames. In S. N. B. Murthy, editor, *Turbulent Mixing in Non-reactive and Reactive Flows*, pages 189–208. Plenum Press, New York, 1975.
- [91] F. A. Williams. *Combustion Theory*. The Benjamin/Cummins Publishing Co., Menlo Park Ca., 1985.
- [92] J. A. Wüning and J. G. Wüning. Flameless oxidation to reduce thermal NO-formation. *Prog. Energy Combust. Sci.*, 23:81–94, 1997.
- [93] Y. B. Zel'dovich. The oxidation of nitrogen in combustion and explosions. *Acta Physiochim.*, 21, 1946.

Appendix A

Chemical Mechanism

Table A.1: Chemical mechanism used in this work. Rate constants are written as $AT^n \exp(-E/RT)$. The units are mol, cm^3 , s, kJ, K.

* refers to this work.

Number	Reaction	A	n	E	Ref.
1f	$\text{O}_2 + \text{H} \rightarrow \text{OH} + \text{O}$	2.000E+14	0.00	70.3	[67]
2f	$\text{H}_2 + \text{O} \rightarrow \text{OH} + \text{H}$	5.060E+04	2.67	26.3	[8]
3f	$\text{H}_2 + \text{OH} \rightarrow \text{H}_2\text{O} + \text{H}$	1.000E+08	1.60	13.8	[8]
4f	$2\text{OH} \rightarrow \text{H}_2\text{O} + \text{O}$	1.500E+09	1.14	0.42	[8]
5f	$\text{O}_2 + \text{H} + \text{M}' \rightarrow \text{HO}_2 + \text{M}'$	2.300E+18	-0.80	0	[67]
6	$\text{HO}_2 + \text{H} \rightarrow 2\text{OH}$	1.500E+14	0.00	4.2	[67]
7	$\text{HO}_2 + \text{H} \rightarrow \text{H}_2 + \text{O}_2$	2.500E+13	0.00	2.9	[67]
8	$\text{HO}_2 + \text{OH} \rightarrow \text{H}_2\text{O} + \text{O}_2$	6.000E+13	0.00	0	[67]
9	$\text{HO}_2 + \text{H} \rightarrow \text{H}_2\text{O} + \text{O}$	3.000E+13	0.00	7.2	[8]
10	$\text{HO}_2 + \text{O} \rightarrow \text{OH} + \text{O}_2$	1.800E+13	0.00	-1.7	[67]
11	$2\text{HO}_2 \rightarrow \text{H}_2\text{O}_2 + \text{O}_2$	2.500E+11	0.00	-5.2	[67]
12f	$2\text{OH} + \text{M}' \rightarrow \text{H}_2\text{O}_2 + \text{M}'$	3.250E+22	-2.00	0	[67]
13	$\text{H}_2\text{O}_2 + \text{H} \rightarrow \text{H}_2\text{O} + \text{OH}$	1.000E+13	0.00	15	[8]
14f	$\text{H}_2\text{O}_2 + \text{OH} \rightarrow \text{H}_2\text{O} + \text{HO}_2$	5.400E+12	0.00	4.2	[34]
15	$2\text{H} + \text{M}' \rightarrow \text{H}_2 + \text{M}'$	1.800E+18	-1.00	0	[89]
16	$\text{OH} + \text{H} + \text{M}' \rightarrow \text{H}_2\text{O} + \text{M}'$	2.200E+22	-2.00	0	[89]
17	$2\text{O} + \text{M}' \rightarrow \text{O}_2 + \text{M}'$	2.900E+17	-1.00	0	[89]
18f	$\text{CO} + \text{OH} \rightarrow \text{CO}_2 + \text{H}$	3.500E+06	1.50	-3.1	[*]
19	$\text{CH} + \text{O}_2 \rightarrow \text{CHO} + \text{O}$	3.000E+13	0.00	0	[67]
20	$\text{CO}_2 + \text{CH} \rightarrow \text{CHO} + \text{CO}$	3.400E+12	0.00	2.9	[67]
21	$\text{CHO} + \text{H} \rightarrow \text{CO} + \text{H}_2$	2.000E+14	0.00	0	[67]
22	$\text{CHO} + \text{OH} \rightarrow \text{CO} + \text{H}_2\text{O}$	1.000E+14	0.00	0	[8]
23	$\text{CHO} + \text{O}_2 \rightarrow \text{CO} + \text{HO}_2$	3.000E+12	0.00	0	[8]
24f	$\text{CHO} + \text{M}' \rightarrow \text{CO} + \text{H} + \text{M}'$	7.100E+14	0.00	70.3	[89]
25f	$\text{CH}_2 + \text{H} \rightarrow \text{CH} + \text{H}_2$	8.400E+09	1.50	1.4	[67]
26	$\text{CH}_2 + \text{O} \rightarrow \text{CO} + 2\text{H}$	8.000E+13	0.00	0	[67]
27	$\text{CH}_2 + \text{O}_2 \rightarrow \text{CO} + \text{OH} + \text{H}$	6.500E+12	0.00	6.3	[67]
28	$\text{CH}_2 + \text{O}_2 \rightarrow \text{CO}_2 + 2\text{H}$	6.500E+12	0.00	6.3	[67]

Table A.1: (continued)

Number	Reaction	A	n	E	Ref.
29	$\text{CH}_2\text{O} + \text{H} \rightarrow \text{CHO} + \text{H}_2$	2.500E+13	0.00	16.7	[67]
30	$\text{CH}_2\text{O} + \text{O} \rightarrow \text{CHO} + \text{OH}$	3.500E+13	0.00	14.6	[67]
31	$\text{CH}_2\text{O} + \text{OH} \rightarrow \text{CHO} + \text{H}_2\text{O}$	3.000E+13	0.00	5	[67]
32	$\text{CH}_2\text{O} + \text{M}' \rightarrow \text{CHO} + \text{H} + \text{M}'$	1.400E+17	0.00	320	[67]
33f	$\text{CH}_3 + \text{H} \rightarrow \text{CH}_2 + \text{H}_2$	1.800E+14	0.00	63	[67]
34	$\text{CH}_3 + \text{H} \rightarrow \text{CH}_4$	k_0 6.257E+23	-1.80	0	[67]
		k_∞ 2.108E+14	0.00	0	
35	$\text{CH}_3 + \text{O} \rightarrow \text{CH}_2\text{O} + \text{H}$	7.000E+13	0.00	0	[67]
36f	$2\text{CH}_3 \rightarrow \text{C}_2\text{H}_6$	k_0 1.272E+41	-7.00	11.6	[51]
		k_∞ 1.813E+13	0.00	0	
37	$\text{CH}_3 + \text{O}_2 \rightarrow \text{CH}_2\text{O} + \text{OH}$	3.400E+11	0.00	37.4	[67]
38f	$\text{CH}_4 + \text{H} \rightarrow \text{CH}_3 + \text{H}_2$	2.200E+04	3.00	36.6	[67]
39	$\text{CH}_4 + \text{O} \rightarrow \text{CH}_3 + \text{OH}$	1.200E+07	2.10	31.9	[67]
40f	$\text{CH}_4 + \text{OH} \rightarrow \text{CH}_3 + \text{H}_2\text{O}$	1.600E+06	2.10	10.3	[67]
a40f	$\text{CH}_4 + \text{O}_2 \rightarrow \text{CH}_3 + \text{HO}_2$	3.970E+13	0.00	238	[8]
41f	$\text{C}_2\text{H} + \text{H}_2 \rightarrow \text{C}_2\text{H}_2 + \text{H}$	1.100E+13	0.00	12	[67]
42	$\text{C}_2\text{H} + \text{O}_2 \rightarrow \text{CHCO} + \text{O}$	5.000E+13	0.00	6.3	[67]
43f	$\text{CHCO} + \text{H} \rightarrow \text{CH}_2 + \text{CO}$	3.000E+13	0.00	0	[67]
44	$\text{CHCO} + \text{O} \rightarrow 2\text{CO} + \text{H}$	1.000E+14	0.00	0	[27]
45	$\text{C}_2\text{H}_2 + \text{O} \rightarrow \text{CH}_2 + \text{CO}$	4.100E+08	1.50	7.1	[67]
46	$\text{C}_2\text{H}_2 + \text{O} \rightarrow \text{CHCO} + \text{H}$	4.300E+14	0.00	50.7	[67]
47f	$\text{C}_2\text{H}_2 + \text{OH} \rightarrow \text{C}_2\text{H} + \text{H}_2\text{O}$	1.000E+13	0.00	29.3	[67]
49	$\text{C}_2\text{H}_3 + \text{H} \rightarrow \text{C}_2\text{H}_2 + \text{H}_2$	3.000E+13	0.00	0	[67]
50	$\text{C}_2\text{H}_3 + \text{O}_2 \rightarrow \text{C}_2\text{H}_2 + \text{HO}_2$	5.400E+11	0.00	0	[67]
51f	$\text{C}_2\text{H}_3 \rightarrow \text{C}_2\text{H}_2 + \text{H}$	k_0 1.187E+42	-7.50	190	[67]
		k_∞ 2.000E+14	0.00	166	
52f	$\text{C}_2\text{H}_4 + \text{H} \rightarrow \text{C}_2\text{H}_3 + \text{H}_2$	1.500E+14	0.00	42.7	[67]
53	$\text{C}_2\text{H}_4 + \text{O} \rightarrow \text{CH}_3 + \text{CO} + \text{H}$	1.600E+09	1.20	3.1	[67]
54f	$\text{C}_2\text{H}_4 + \text{OH} \rightarrow \text{C}_2\text{H}_3 + \text{H}_2\text{O}$	3.000E+13	0.00	12.6	[67]

Table A.1: (continued)

Number	Reaction	A	n	E	Ref.
55	$\text{C}_2\text{H}_4 + \text{M}' \rightarrow \text{C}_2\text{H}_2 + \text{H}_2 + \text{M}'$	2.500E+17	0.00	320	[67]
56f	$\text{C}_2\text{H}_5 + \text{H} \rightarrow 2\text{CH}_3$	3.000E+13	0.00	0	[67]
57	$\text{C}_2\text{H}_5 + \text{O}_2 \rightarrow \text{C}_2\text{H}_4 + \text{HO}_2$	2.000E+12	0.00	20.9	[67]
58f	$\text{C}_2\text{H}_5 \rightarrow \text{C}_2\text{H}_4 + \text{H}$	k_0	0.00	126	[34]
		k_∞	0.00	167	
59	$\text{C}_2\text{H}_6 + \text{H} \rightarrow \text{C}_2\text{H}_5 + \text{H}_2$	5.400E+02	3.50	21.8	[67]
60	$\text{C}_2\text{H}_6 + \text{O} \rightarrow \text{C}_2\text{H}_5 + \text{OH}$	3.000E+07	2.00	21.4	[67]
61	$\text{C}_2\text{H}_6 + \text{OH} \rightarrow \text{C}_2\text{H}_5 + \text{H}_2\text{O}$	6.300E+06	2.00	2.7	[67]
N.1 NH_3 Verbrauch					
N2f	$\text{NH}_3 + \text{H} \rightarrow \text{NH}_2 + \text{H}_2$	6.400E+05	2.39	42.6	[33]
N.2 NH_2 Verbrauch					
N6f	$\text{NH}_2 + \text{H} \rightarrow \text{NH} + \text{H}_2$	4.000E+13	0.00	15.3	[33]
N7f	$\text{NH}_2 + \text{O} \rightarrow \text{HNO} + \text{H}$	9.900E+14	-0.50	0	[84]
N9f	$\text{NH}_2 + \text{OH} \rightarrow \text{NH} + \text{H}_2\text{O}$	4.000E+06	2.00	4.19	[33]
N14f	$\text{NH}_2 + \text{NO} \rightarrow \text{N}_2 + \text{H}_2\text{O}$	9.300E+11	0.00	0	[88]
N.3 NH Verbrauch					
N17f	$\text{NH} + \text{O} \rightarrow \text{NO} + \text{H}$	9.200E+13	0.00	0	[33]
N18f	$\text{NH} + \text{OH} \rightarrow \text{HNO} + \text{H}$	4.000E+13	0.00	0	[84]
N19f	$\text{NH} + \text{OH} \rightarrow \text{N} + \text{H}_2\text{O}$	5.000E+11	0.50	8.37	[28]
N24xf	$\text{NH} + \text{NO} \rightarrow \text{N}_2\text{O} + \text{H}$	2.940E+14	-0.40	0	[59]
N24y	$\text{NH} + \text{NO} \rightarrow \text{N}_2\text{O} + \text{H}$	-2.200E+13	-0.23	0	[59]
N.5 N Verbrauch					
N35f	$\text{N} + \text{O}_2 \rightarrow \text{NO} + \text{O}$	6.400E+09	1.00	26.3	[33]
N36f	$\text{N} + \text{OH} \rightarrow \text{NO} + \text{H}$	3.800E+13	0.00	0	[33]
N37f	$\text{N} + \text{NO} \rightarrow \text{N}_2 + \text{O}$	3.300E+12	0.30	0	[33]
N.7 N_2O Verbrauch					
N45f	$\text{N}_2\text{O} + \text{M5} \rightarrow \text{N}_2 + \text{O} + \text{M5}$	4.000E+14	0.00	235	[33]
N46yf	$\text{N}_2\text{O} + \text{H} \rightarrow \text{N}_2 + \text{OH}$	4.400E+14	0.00	80.6	[33]
N47f	$\text{N}_2\text{O} + \text{O} \rightarrow 2\text{NO}$	2.900E+13	0.00	96.9	[33]
N49f	$\text{N}_2\text{O} + \text{OH} \rightarrow \text{N}_2 + \text{HO}_2$	2.000E+12	0.00	41.8	[33]

Table A.1: (continued)

Number	Reaction	A	n	E	Ref.
N.14 NO ₂ Bildung und Verbrauch					
N84f	NO ₂ + M8 → NO + O + M8	7.000E+14	0.00	222	[58]
N85f	NO + HO ₂ → NO ₂ + OH	2.100E+12	0.00	-2.01	[33]
N87f	NO ₂ + H → NO + OH	3.500E+14	0.00	6.28	[33]
N88f	NO ₂ + O → NO + O ₂	1.000E+13	0.00	2.51	[33]
N.15 HNCO Verbrauch					
N60f	HNCO + M7 → NH + CO + M7	1.100E+16	0.00	360	[33]
N61f	HNCO + H → NH ₂ + CO	2.200E+07	1.70	15.9	[33]
N.15 NCO Verbrauch					
N70f	NCO + M7 → N + CO + M7	3.100E+16	-0.50	201	[33]
N71f	NCO + H → CO + NH	5.000E+13	0.00	0	[33]
N72f	NCO + O → NO + CO	4.700E+13	0.00	0	[33]
N.16 N ₂ Verbrauch					
N110	N ₂ + CH → HCN + N	4.400E+12	0.00	92	[33]
N.17 NO Verbrauch					
N111	NO + CH ₃ → HCN + H ₂ O	8.300E+11	0.00	67.3	[33]
N112	NO + ₃ -CH ₂ → HNCO + H	2.900E+12	0.00	-2.5	[33]
N113	NO + CH → HCN + O	1.100E+14	0.00	0	[33]
N.18 HCN Verbrauch					
N120	HCN + O → NCO + H	1.400E+06	2.10	25.6	[33]
N.19 CN Verbrauch					
N130f	CN + H ₂ → HCN + H	3.600E+08	1.55	12.6	[33]
N134	CN + OH → NCO + H	4.200E+13	0.00	0	[33]

Third-body efficiencies are:

$$\begin{aligned}
[M'] &= 6.5[CH_4] + 6.5[H_2O] + 1.5[CO_2] + 0.75[CO] + \\
&\quad 0.4[O_2] + 0.4[N_2] + 1.0[OTHER]. \\
[M_5] &= 1.5[N_2] + 1.5[O_2] + 10.0[H_2O] + 1.0[OTHER]. \\
[M_7] &= 1.5[N_2] + 1.5[O_2] + 18.6[H_2O] + 1.0[OTHER]. \\
[M_8] &= 1.5[N_2] + 10.0[H_2O] + 1.0[OTHER].
\end{aligned}$$

Appendix B

Global Rates

The global rates of the 19-step chemical reaction mechanism for methane and NO_x derived in section 4.3.2 are listed below.

$$wI = -w34 + w38f - w38b + w39 + w40f - w40b + wa40f - wa40b$$

$$\begin{aligned} wII = & -0.5 w1f + 0.5 w1b - 0.5 w3f + 0.5 w3b - 0.5 w4f + 0.5 w4b \\ & + 0.5 w5f - 0.5 w5b + 0.5 w7 - 0.5 w9 + 0.5 w10 + 0.5 w12f - 0.5 w12b \\ & + w15 + 0.5 w16 + 1.5 w17 + 0.5 w20 - 0.5 w22 - 0.5 w23 - w24f \\ & + w24b - 0.5 w26 - w27 - w28 - 0.5 w31 - w32 + w34 + 0.5 w35 \\ & + w36f - w36b - 0.5 w40f + 0.5 w40b - 0.5 wa40f + 0.5 wa40b \\ & + 0.5 w41f - 0.5 w41b - 0.5 w44 - w47f + w47b - 0.5 w50 - w51f \\ & + w51b - w53 - 0.5 w54f + 0.5 w54b - w55 - 0.5 w58f + 0.5 w58b \\ & - 0.5 w61 + wn6f - wn6b + wn7f - wn7b + 0.5 wn9f - 0.5 wn9b - wn19f \\ & + wn19b - 1.5 wn24xf + 1.5 wn24xb - 1.5 wn24y + 0.5 wn36f - 0.5 wn36b \\ & + wn46yf - wn46yb + 1.5 wn47f - 1.5 wn47b + wn49f - wn49b - wn84f \\ & + wn84b + 0.5 wn88f - 0.5 wn88b - 1.5 wn70f + 1.5 wn70b + 0.5 wn110 \\ & - 0.5 wn112 + 0.5 wn113 \end{aligned}$$

$$\begin{aligned}
w_{III} = & -0.5 w_{1f} + 0.5 w_{1b} - 0.5 w_{3f} + 0.5 w_{3b} - 0.5 w_{4f} + 0.5 w_{4b} \\
& + 0.5 w_{5f} - 0.5 w_{5b} + 0.5 w_7 - 0.5 w_9 + 0.5 w_{10} + 0.5 w_{12f} \\
& - 0.5 w_{12b} + w_{15} + 0.5 w_{16} + 1.5 w_{17} + 0.5 w_{20} - 0.5 w_{22} \\
& - 0.5 w_{23} - w_{24f} + w_{24b} - 0.5 w_{26} - w_{27} - w_{28} - 0.5 w_{31} \\
& - w_{32} + w_{34} + 0.5 w_{35} - 0.5 w_{40f} + 0.5 w_{40b} - 0.5 w_{a40f} \\
& + 0.5 w_{a40b} + 0.5 w_{41f} - 0.5 w_{41b} - 0.5 w_{44} - w_{47f} + w_{47b} \\
& - 0.5 w_{50} - w_{51f} + w_{51b} - w_{53} - 0.5 w_{54f} + 0.5 w_{54b} - w_{55} \\
& - 0.5 w_{58f} + 0.5 w_{58b} + w_{59} + w_{60} + 0.5 w_{61} + w_{n6f} - w_{n6b} \\
& + w_{n7f} - w_{n7b} + 0.5 w_{n9f} - 0.5 w_{n9b} - w_{n19f} + w_{n19b} \\
& - 1.5 w_{n24xf} + 1.5 w_{n24xb} - 1.5 w_{n24y} + 0.5 w_{n36f} - 0.5 w_{n36b} \\
& + w_{n46yf} - w_{n46yb} + 1.5 w_{n47f} - 1.5 w_{n47b} + w_{n49f} - w_{n49b} \\
& - w_{n84f} + w_{n84b} + 0.5 w_{n88f} - 0.5 w_{n88b} - 1.5 w_{n70f} \\
& + 1.5 w_{n70b} + 0.5 w_{n110} - 0.5 w_{n112} + 0.5 w_{n113} \\
\\
w_{IV} = & -0.25 w_{1f} + 0.25 w_{1b} - 0.5 w_{2f} + 0.5 w_{2b} + 0.25 w_{3f} - 0.25 w_{3b} \\
& + 0.75 w_{4f} - 0.75 w_{4b} + 0.25 w_{5f} - 0.25 w_{5b} - w_6 - 0.25 w_7 \\
& - 0.25 w_9 - 0.75 w_{10} + 1.25 w_{12f} - 1.25 w_{12b} - w_{13} + 0.25 w_{16} \\
& - 0.25 w_{17} + 0.25 w_{20} + 0.25 w_{22} + 0.25 w_{23} - 0.25 w_{26} \\
& - 0.5 w_{27} - 0.5 w_{28} - 0.5 w_{30} + 0.25 w_{31} + 0.5 w_{33f} - 0.5 w_{33b} \\
& + 0.25 w_{35} - 0.5 w_{39} + 0.25 w_{40f} - 0.25 w_{40b} + 0.25 w_{a40f} \\
& - 0.25 w_{a40b} - 0.25 w_{41f} + 0.25 w_{41b} - 0.25 w_{44} + 0.5 w_{47f} \\
& - 0.5 w_{47b} + 0.25 w_{50} - 0.5 w_{53} + 0.25 w_{54f} - 0.25 w_{54b} \\
& + w_{57} + 0.75 w_{58f} - 0.75 w_{58b} - 0.5 w_{60} + 0.25 w_{61} \\
& + 0.25 w_{n9f} - 0.25 w_{n9b} + 0.5 w_{n18f} - 0.5 w_{n18b} + 0.5 w_{n19f} \\
& - 0.5 w_{n19b} + 0.25 w_{n24xf} - 0.25 w_{n24xb} + 0.25 w_{n24y} \\
& + 0.25 w_{n36f} - 0.25 w_{n36b} - 0.5 w_{n46yf} + 0.5 w_{n46yb} \\
& - 0.25 w_{n47f} + 0.25 w_{n47b} + 0.5 w_{n49f} - 0.5 w_{n49b} + 0.5 w_{n84f} \\
& - 0.5 w_{n84b} - w_{n85f} + w_{n85b} + 0.25 w_{n88f} - 0.25 w_{n88b} \\
& + 0.25 w_{n70f} - 0.25 w_{n70b} - 0.25 w_{n110} - 0.25 w_{n112} \\
& - 0.25 w_{n113} + 0.5 w_{n134} \\
\\
w_V = & -0.25 w_{1f} + 0.25 w_{1b} - 0.5 w_{2f} + 0.5 w_{2b} + 0.25 w_{3f} - 0.25 w_{3b} \\
& + 0.75 w_{4f} - 0.75 w_{4b} + 0.25 w_{5f} - 0.25 w_{5b} - w_6 - 0.25 w_7 \\
& - 0.25 w_9 - 0.75 w_{10} + 1.25 w_{12f} - 1.25 w_{12b} - w_{13} + 0.25 w_{16} \\
& - 0.25 w_{17} + 0.25 w_{20} + 0.25 w_{22} + 0.25 w_{23} - 0.25 w_{26} \\
& - 0.5 w_{27} - 0.5 w_{28} - 0.5 w_{30} + 0.25 w_{31} + 0.5 w_{33f} - 0.5 w_{33b} \\
& + 0.25 w_{35} - 0.5 w_{39} + 0.25 w_{40f} - 0.25 w_{40b} + 0.25 w_{a40f}
\end{aligned}$$

$$\begin{aligned}
& - 0.25 \text{ wa40b} - 0.25 \text{ w41f} + 0.25 \text{ w41b} - 0.25 \text{ w44} + 0.5 \text{ w47f} - 0.5 \text{ w47b} \\
& + \text{ w49} + 1.25 \text{ w50} + \text{ w51f} - \text{ w51b} + 0.5 \text{ w53} + 0.25 \text{ w54f} - 0.25 \text{ w54b} \\
& + \text{ w55} - 0.25 \text{ w58f} + 0.25 \text{ w58b} - 0.5 \text{ w60} + 0.25 \text{ w61} + 0.25 \text{ wn9f} \\
& - 0.25 \text{ wn9b} + 0.5 \text{ wn18f} - 0.5 \text{ wn18b} + 0.5 \text{ wn19f} - 0.5 \text{ wn19b} \\
& + 0.25 \text{ wn24xf} - 0.25 \text{ wn24xb} + 0.25 \text{ wn24y} + 0.25 \text{ wn36f} \\
& - 0.25 \text{ wn36b} - 0.5 \text{ wn46yf} + 0.5 \text{ wn46yb} - 0.25 \text{ wn47f} + 0.25 \text{ wn47b} \\
& + 0.5 \text{ wn49f} - 0.5 \text{ wn49b} + 0.5 \text{ wn84f} - 0.5 \text{ wn84b} - \text{ wn85f} + \text{ wn85b} \\
& + 0.25 \text{ wn88f} - 0.25 \text{ wn88b} + 0.25 \text{ wn70f} - 0.25 \text{ wn70b} - 0.25 \text{ wn110} \\
& - 0.25 \text{ wn112} - 0.25 \text{ wn113} + 0.5 \text{ wn134}
\end{aligned}$$

$$\begin{aligned}
\text{wVI} = & - 0.25 \text{ w1f} + 0.25 \text{ w1b} - 0.5 \text{ w2f} + 0.5 \text{ w2b} + 0.25 \text{ w3f} \\
& - 0.25 \text{ w3b} + 0.75 \text{ w4f} - 0.75 \text{ w4b} + 0.25 \text{ w5f} - 0.25 \text{ w5b} - \text{ w6} - 0.25 \text{ w7} \\
& - 0.25 \text{ w9} - 0.75 \text{ w10} + 1.25 \text{ w12f} - 1.25 \text{ w12b} - \text{ w13} + 0.25 \text{ w16} \\
& - 0.25 \text{ w17} + 0.25 \text{ w20} + 0.25 \text{ w22} + 0.25 \text{ w23} - 0.25 \text{ w26} - 0.5 \text{ w27} \\
& - 0.5 \text{ w28} - 0.5 \text{ w30} + 0.25 \text{ w31} + 0.5 \text{ w33f} - 0.5 \text{ w33b} + 0.25 \text{ w35} \\
& - 0.5 \text{ w39} + 0.25 \text{ w40f} - 0.25 \text{ w40b} + 0.25 \text{ wa40f} - 0.25 \text{ wa40b} \\
& - 1.25 \text{ w41f} + 1.25 \text{ w41b} - 0.25 \text{ w44} + \text{ w45} + \text{ w46} + 1.5 \text{ w47f} - 1.5 \text{ w47b} \\
& + 0.25 \text{ w50} + 0.5 \text{ w53} + 0.25 \text{ w54f} - 0.25 \text{ w54b} - 0.25 \text{ w58f} + 0.25 \text{ w58b} \\
& - 0.5 \text{ w60} + 0.25 \text{ w61} + 0.25 \text{ wn9f} - 0.25 \text{ wn9b} + 0.5 \text{ wn18f} - 0.5 \text{ wn18b} \\
& + 0.5 \text{ wn19f} - 0.5 \text{ wn19b} + 0.25 \text{ wn24xf} - 0.25 \text{ wn24xb} + 0.25 \text{ wn24y} \\
& + 0.25 \text{ wn36f} - 0.25 \text{ wn36b} - 0.5 \text{ wn46yf} + 0.5 \text{ wn46yb} - 0.25 \text{ wn47f} \\
& + 0.25 \text{ wn47b} + 0.5 \text{ wn49f} - 0.5 \text{ wn49b} + 0.5 \text{ wn84f} - 0.5 \text{ wn84b} - \text{ wn85f} \\
& + \text{ wn85b} + 0.25 \text{ wn88f} - 0.25 \text{ wn88b} + 0.25 \text{ wn70f} - 0.25 \text{ wn70b} \\
& - 0.25 \text{ wn110} - 0.25 \text{ wn112} - 0.25 \text{ wn113} + 0.5 \text{ wn134}
\end{aligned}$$

$$\begin{aligned}
\text{wVII} = & 0.75 \text{ w1f} - 0.75 \text{ w1b} + 0.5 \text{ w2f} - 0.5 \text{ w2b} - 0.75 \text{ w3f} + 0.75 \text{ w3b} \\
& - 1.25 \text{ w4f} + 1.25 \text{ w4b} - 0.75 \text{ w5f} + 0.75 \text{ w5b} + 2 \text{ w6} + 0.75 \text{ w7} \\
& + 0.75 \text{ w9} + 1.25 \text{ w10} - 2.75 \text{ w12f} + 2.75 \text{ w12b} + 2 \text{ w13} - 0.75 \text{ w16} \\
& - 0.25 \text{ w17} - 0.75 \text{ w20} - 0.75 \text{ w22} - 0.75 \text{ w23} - 0.25 \text{ w26} + 0.5 \text{ w27} \\
& + 0.5 \text{ w28} + 0.5 \text{ w30} - 0.75 \text{ w31} + 0.5 \text{ w33f} - 0.5 \text{ w33b} + 0.25 \text{ w35} \\
& + \text{ w37} + 0.5 \text{ w39} - 0.75 \text{ w40f} + 0.75 \text{ w40b} - 0.75 \text{ wa40f} + 0.75 \text{ wa40b} \\
& - 0.25 \text{ w41f} + 0.25 \text{ w41b} - 0.25 \text{ w44} - 0.5 \text{ w47f} + 0.5 \text{ w47b} - 0.75 \text{ w50} \\
& - 0.5 \text{ w53} - 0.75 \text{ w54f} + 0.75 \text{ w54b} + 0.75 \text{ w58f} - 0.75 \text{ w58b} + 0.5 \text{ w60} \\
& - 0.75 \text{ w61} - 0.75 \text{ wn9f} + 0.75 \text{ wn9b} - 0.5 \text{ wn18f} + 0.5 \text{ wn18b} - 0.5 \text{ wn19f} \\
& + 0.5 \text{ wn19b} + 0.25 \text{ wn24xf} - 0.25 \text{ wn24xb} + 0.25 \text{ wn24y} - 0.75 \text{ wn36f} \\
& + 0.75 \text{ wn36b} + 0.5 \text{ wn46yf} - 0.5 \text{ wn46yb} - 0.25 \text{ wn47f} + 0.25 \text{ wn47b} \\
& - 1.5 \text{ wn49f} + 1.5 \text{ wn49b} - 0.5 \text{ wn84f} + 0.5 \text{ wn84b} + 2 \text{ wn85f} - 2 \text{ wn85b} \\
& - 0.75 \text{ wn88f} + 0.75 \text{ wn88b} + 0.25 \text{ wn70f} - 0.25 \text{ wn70b} - 0.25 \text{ wn110} \\
& - 0.25 \text{ wn112} - 0.25 \text{ wn113} - 0.5 \text{ wn134}
\end{aligned}$$

$$\begin{aligned}
wVIII = & 0.75 w1f - 0.75 w1b + 0.5 w2f - 0.5 w2b - 0.75 w3f + 0.75 w3b \\
& - 1.25 w4f + 1.25 w4b - 0.75 w5f + 0.75 w5b + 2 w6 + 0.75 w7 \\
& + 0.75 w9 + 1.25 w10 - 2.75 w12f + 2.75 w12b + 2 w13 \\
& - 0.75 w16 - 0.25 w17 - 0.75 w20 - 0.75 w22 - 0.75 w23 - 0.25 w26 \\
& + 0.5 w27 + 0.5 w28 + w29 + 1.5 w30 + 0.25 w31 + w32 \\
& + 0.5 w33f - 0.5 w33b - 0.75 w35 + 0.5 w39 - 0.75 w40f + 0.75 w40b \\
& - 0.75 w40f + 0.75 w40b - 0.25 w41f + 0.25 w41b - 0.25 w44 \\
& - 0.5 w47f + 0.5 w47b - 0.75 w50 - 0.5 w53 - 0.75 w54f + 0.75 w54b \\
& + 0.75 w58f - 0.75 w58b + 0.5 w60 - 0.75 w61 - 0.75 wn9f \\
& + 0.75 wn9b - 0.5 wn18f + 0.5 wn18b - 0.5 wn19f + 0.5 wn19b \\
& + 0.25 wn24xf - 0.25 wn24xb + 0.25 wn24y - 0.75 wn36f \\
& + 0.75 wn36b + 0.5 wn46yf - 0.5 wn46yb - 0.25 wn47f + 0.25 wn47b \\
& - 1.5 wn49f + 1.5 wn49b - 0.5 wn84f + 0.5 wn84b + 2 wn85f \\
& - 2 wn85b - 0.75 wn88f + 0.75 wn88b + 0.25 wn70f - 0.25 wn70b \\
& - 0.25 wn110 - 0.25 wn112 - 0.25 wn113 - 0.5 wn134
\end{aligned}$$

$$\begin{aligned}
wIX = & - 0.25 w1f + 0.25 w1b - 0.5 w2f + 0.5 w2b + 0.25 w3f - 0.25 w3b \\
& + 0.75 w4f - 0.75 w4b + 0.25 w5f - 0.25 w5b - w6 - 0.25 w7 \\
& - 0.25 w9 - 0.75 w10 + 1.25 w12f - 1.25 w12b - w13 + 0.25 w16 \\
& - 0.25 w17 + 0.25 w20 + 0.25 w22 + 0.25 w23 + w25f - w25b \\
& + 0.75 w26 + 0.5 w27 + 0.5 w28 - 0.5 w30 + 0.25 w31 - 0.5 w33f \\
& + 0.5 w33b + 0.25 w35 - 0.5 w39 + 0.25 w40f - 0.25 w40b \\
& + 0.25 w40f - 0.25 w40b - 0.25 w41f + 0.25 w41b + 0.75 w44 \\
& + 0.5 w47f - 0.5 w47b + 0.25 w50 + 0.5 w53 + 0.25 w54f \\
& - 0.25 w54b - 0.25 w58f + 0.25 w58b - 0.5 w60 + 0.25 w61 \\
& + 0.25 wn9f - 0.25 wn9b + 0.5 wn18f - 0.5 wn18b + 0.5 wn19f \\
& - 0.5 wn19b + 0.25 wn24xf - 0.25 wn24xb + 0.25 wn24y \\
& + 0.25 wn36f - 0.25 wn36b - 0.5 wn46yf + 0.5 wn46yb - 0.25 wn47f \\
& + 0.25 wn47b + 0.5 wn49f - 0.5 wn49b + 0.5 wn84f - 0.5 wn84b \\
& - wn85f + wn85b + 0.25 wn88f - 0.25 wn88b + 0.25 wn70f \\
& - 0.25 wn70b - 0.25 wn110 + 0.75 wn112 - 0.25 wn113 + 0.5 wn134
\end{aligned}$$

$$wX = w18f - w18b - w20 + w28$$

$$\begin{aligned}
\text{wXI} = & - 0.25 \text{ w1f} + 0.25 \text{ w1b} - 0.5 \text{ w2f} + 0.5 \text{ w2b} + 0.25 \text{ w3f} \\
& - 0.25 \text{ w3b} + 0.75 \text{ w4f} - 0.75 \text{ w4b} - 0.75 \text{ w5f} + 0.75 \text{ w5b} + 0.75 \text{ w7} \\
& + \text{ w8} + 0.75 \text{ w9} + 0.25 \text{ w10} + \text{ w11} + 0.25 \text{ w12f} - 0.25 \text{ w12b} + 0.25 \text{ w16} \\
& - 0.25 \text{ w17} + 0.25 \text{ w20} + 0.25 \text{ w22} - 0.75 \text{ w23} - 0.25 \text{ w26} - 0.5 \text{ w27} \\
& - 0.5 \text{ w28} - 0.5 \text{ w30} + 0.25 \text{ w31} + 0.5 \text{ w33f} - 0.5 \text{ w33b} + 0.25 \text{ w35} \\
& - 0.5 \text{ w39} + 0.25 \text{ w40f} - 0.25 \text{ w40b} - 0.75 \text{ wa40f} + 0.75 \text{ wa40b} \\
& - 0.25 \text{ w41f} + 0.25 \text{ w41b} - 0.25 \text{ w44} + 0.5 \text{ w47f} - 0.5 \text{ w47b} - 0.75 \text{ w50} \\
& - 0.5 \text{ w53} + 0.25 \text{ w54f} - 0.25 \text{ w54b} + 0.75 \text{ w58f} - 0.75 \text{ w58b} - 0.5 \text{ w60} \\
& + 0.25 \text{ w61} + 0.25 \text{ wn9f} - 0.25 \text{ wn9b} + 0. \text{ wn18f} - 0.5 \text{ wn18b} + 0.5 \text{ wn19f} \\
& - 0.5 \text{ wn19b} + 0.25 \text{ wn24xf} - 0.25 \text{ wn24xb} + 0.25 \text{ wn24y} + 0.25 \text{ wn36f} \\
& - 0.25 \text{ wn36b} - 0.5 \text{ wn46yf} + 0.5 \text{ wn46yb} - 0.25 \text{ wn47f} + 0.25 \text{ wn47b} \\
& - 0.5 \text{ wn49f} + 0.5 \text{ wn49b} + 0.5 \text{ wn84f} - 0.5 \text{ wn84b} + 0.25 \text{ wn88f} \\
& - 0.25 \text{ wn88b} + 0.25 \text{ wn70f} - 0.25 \text{ wn70b} - 0.25 \text{ wn110} - 0.25 \text{ wn112} \\
& - 0.25 \text{ wn113} + 0.5 \text{ wn134}
\end{aligned}$$

$$\begin{aligned}
\text{wXII} = & - 0.25 \text{ w1f} + 0.25 \text{ w1b} - 0.5 \text{ w2f} + 0.5 \text{ w2b} + 0.25 \text{ w3f} \\
& - 0.25 \text{ w3b} + 0.75 \text{ w4f} - 0.75 \text{ w4b} - 0.75 \text{ w5f} + 0.75 \text{ w5b} + 0.75 \text{ w7} \\
& + \text{ w8} + 0.75 \text{ w9} + 0.25 \text{ w10} - 0.75 \text{ w12f} + 0.75 \text{ w12b} + \text{ w13} + \text{ w14f} \\
& - \text{ w14b} + 0.25 \text{ w16} - 0.25 \text{ w17} + 0.25 \text{ w20} + 0.25 \text{ w22} - 0.75 \text{ w23} \\
& - 0.25 \text{ w26} - 0.5 \text{ w27} - 0.5 \text{ w28} - 0.5 \text{ w30} + 0.25 \text{ w31} + 0.5 \text{ w33f} \\
& - 0.5 \text{ w33b} + 0.25 \text{ w35} - 0.5 \text{ w39} + 0.25 \text{ w40f} - 0.25 \text{ w40b} - 0.75 \text{ wa40f} \\
& + 0.75 \text{ wa40b} - 0.25 \text{ w41f} + 0.25 \text{ w41b} - 0.25 \text{ w44} + 0.5 \text{ w47f} - 0.5 \text{ w47b} \\
& - 0.75 \text{ w50} - 0.5 \text{ w53} + 0.25 \text{ w54f} - 0.25 \text{ w54b} + 0.75 \text{ w58f} - 0.75 \text{ w58b} \\
& - 0.5 \text{ w60} + 0.25 \text{ w61} + 0.25 \text{ wn9f} - 0.25 \text{ wn9b} + 0.5 \text{ wn18f} - 0.5 \text{ wn18b} \\
& + 0.5 \text{ wn19f} - 0.5 \text{ wn19b} + 0.25 \text{ wn24xf} - 0.25 \text{ wn24xb} + 0.25 \text{ wn24y} \\
& + 0.25 \text{ wn36f} - 0.25 \text{ wn36b} - 0.5 \text{ wn46yf} + 0.5 \text{ wn46yb} - 0.25 \text{ wn47f} \\
& + 0.25 \text{ wn47b} - 0.5 \text{ wn49f} + 0.5 \text{ wn49b} + 0.5 \text{ wn84f} - 0.5 \text{ wn84b} \\
& + 0.25 \text{ wn88f} - 0.25 \text{ wn88b} + 0.25 \text{ wn70f} - 0.25 \text{ wn70b} - 0.25 \text{ wn110} \\
& - 0.25 \text{ wn112} - 0.25 \text{ wn113} + 0.5 \text{ wn134}
\end{aligned}$$

$$\begin{aligned}
\text{wXIII} = & 0.5 \text{ w1f} - 0.5 \text{ w1b} + 0.5 \text{ w3f} - 0.5 \text{ w3b} + 0.5 \text{ w4f} - 0.5 \text{ w4b} \\
& + 0.5 \text{ w5f} - 0.5 \text{ w5b} - 0.5 \text{ w7} + 0.5 \text{ w9} - 0.5 \text{ w10} + 0.5 \text{ w12f} - 0.5 \text{ w12b} \\
& + 0.5 \text{ w16} - 0.5 \text{ w17} - 0.5 \text{ w20} + 0.5 \text{ w22} + 0.5 \text{ w23} - 0.5 \text{ w26} + 0.5 \text{ w31} \\
& - 0.5 \text{ w35} + 0.5 \text{ w40f} - 0.5 \text{ w40b} + 0.5 \text{ wa40f} - 0.5 \text{ wa40b} - 0.5 \text{ w41f} \\
& + 0.5 \text{ w41b} - 0.5 \text{ w44} + \text{ w47f} - \text{ w47b} + 0.5 \text{ w50} + 0.5 \text{ w54f} - 0.5 \text{ w54b} \\
& - 0.5 \text{ w58f} + 0.5 \text{ w58b} + 0.5 \text{ w61} + 0.5 \text{ wn9f} - 0.5 \text{ wn9b} + \text{ wn19f} \\
& - \text{ wn19b} - 0.5 \text{ wn24xf} + 0.5 \text{ wn24xb} - 0.5 \text{ wn24y} - 0.5 \text{ wn36f} + 0.5 \text{ wn36b} \\
& - \text{ wn37f} + \text{ wn37b} + 0.5 \text{ wn47f} - 0.5 \text{ wn47b} - 0.5 \text{ wn88f} + 0.5 \text{ wn88b} \\
& + 0.5 \text{ wn70f} - 0.5 \text{ wn70b} + 0.5 \text{ wn110} - 0.5 \text{ wn112} - 0.5 \text{ wn113}
\end{aligned}$$

$$\begin{aligned}
wXIV = & -0.25 w1f + 0.25 w1b + 0.5 w2f - 0.5 w2b + 0.25 w3f - 0.25 w3b \\
& - 0.25 w4f + 0.25 w4b + 0.25 w5f - 0.25 w5b - 0.25 w7 - 0.25 w9 \\
& + 0.25 w10 + 0.25 w12f - 0.25 w12b + 0.25 w16 + 0.75 w17 \\
& + 0.25 w20 + 0.25 w22 + 0.25 w23 + 0.75 w26 + 0.5 w27 + 0.5 w28 \\
& + 0.5 w30 + 0.25 w31 - 0.5 w33f + 0.5 w33b + 0.25 w35 + 0.5 w39 \\
& + 0.25 w40f - 0.25 w40b + 0.25 wa40f - 0.25 wa40b + 0.75 w41f \\
& - 0.75 w41b + 0.75 w44 - 0.5 w47f + 0.5 w47b + 0.25 w50 + 0.5 w53 \\
& + 0.25 w54f - 0.25 w54b - 0.25 w58f + 0.25 w58b + 0.5 w60 \\
& + 0.25 w61 + 0.25 wn9f - 0.25 wn9b - 0.5 wn18f + 0.5 wn18b \\
& - 0.5 wn19f + 0.5 wn19b - 0.75 wn24xf + 0.75 wn24xb - 0.75 wn24y \\
& + 0.25 wn36f - 0.25 wn36b + 0.5 wn46yf - 0.5 wn46yb + 0.75 wn47f \\
& - 0.75 wn47b + 0.5 wn49f - 0.5 wn49b - 0.5 wn84f + 0.5 wn84b \\
& + 0.25 wn88f - 0.25 wn88b - 0.75 wn70f + 0.75 wn70b + 0.75 wn110 \\
& + wn111 + 0.75 wn112 + 0.75 wn113 - 0.5 wn134
\end{aligned}$$

$$\begin{aligned}
wXV = & -0.25 w1f + 0.25 w1b + 0.5 w2f - 0.5 w2b + 0.25 w3f - 0.25 w3b \\
& - 0.25 w4f + 0.25 w4b + 0.25 w5f - 0.25 w5b - 0.25 w7 - 0.25 w9 \\
& + 0.25 w10 + 0.25 w12f - 0.25 w12b + 0.25 w16 + 0.75 w17 \\
& + 0.25 w20 + 0.25 w22 + 0.25 w23 + 0.75 w26 + 0.5 w27 \\
& + 0.5 w28 + 0.5 w30 + 0.25 w31 - 0.5 w33f + 0.5 w33b + 0.25 w35 \\
& + 0.5 w39 + 0.25 w40f - 0.25 w40b + 0.25 wa40f - 0.25 wa40b \\
& + 0.75 w41f - 0.75 w41b + 0.75 w44 - 0.5 w47f + 0.5 w47b \\
& + 0.25 w50 + 0.5 w53 + 0.25 w54f - 0.25 w54b - 0.25 w58f \\
& + 0.25 w58b + 0.5 w60 + 0.25 w61 + 0.25 wn9f - 0.25 wn9b \\
& - 0.5 wn18f + 0.5 wn18b - 0.5 wn19f + 0.5 wn19b - 0.75 wn24xf \\
& + 0.75 wn24xb - 0.75 wn24y + 0.25 wn36f - 0.25 wn36b \\
& + 0.5 wn46yf - 0.5 wn46yb + 0.75 wn47f - 0.75 wn47b \\
& + 0.5 wn49f - 0.5 wn49b - 0.5 wn84f + 0.5 wn84b + 0.25 wn88f \\
& - 0.25 wn88b - 0.75 wn70f + 0.75 wn70b - 0.25 wn110 \\
& + 0.75 wn112 - 0.25 wn113 + wn120 + 0.5 wn134
\end{aligned}$$

$$\begin{aligned}
wXVI = & -0.25 w1f + 0.25 w1b + 0.5 w2f - 0.5 w2b + 0.25 w3f - 0.25 w3b \\
& - 0.25 w4f + 0.25 w4b + 0.25 w5f - 0.25 w5b - 0.25 w7 - 0.25 w9 \\
& + 0.25 w10 + 0.25 w12f - 0.25 w12b + 0.25 w16 + 0.75 w17 \\
& + 0.25 w20 + 0.25 w22 + 0.25 w23 + 0.75 w26 + 0.5 w27 \\
& + 0.5 w28 + 0.5 w30 + 0.25 w31 - 0.5 w33f + 0.5 w33b \\
& + 0.25 w35 + 0.5 w39 + 0.25 w40f - 0.25 w40b + 0.25 wa40f \\
& - 0.25 wa40b + 0.75 w41f - 0.75 w41b + 0.75 w44 - 0.5 w47f \\
& + 0.5 w47b + 0.25 w50 + 0.5 w53 + 0.25 w54f
\end{aligned}$$

$$\begin{aligned}
& - 0.25 \text{ w54b} - 0.25 \text{ w58f} + 0.25 \text{ w58b} + 0.5 \text{ w60} + 0.25 \text{ w61} \\
& + 0.25 \text{ wn9f} - 0.25 \text{ wn9b} - 0.5 \text{ wn18f} + 0.5 \text{ wn18b} - 0.5 \text{ wn19f} \\
& + 0.5 \text{ wn19b} - 0.75 \text{ wn24xf} + 0.75 \text{ wn24xb} - 0.75 \text{ wn24y} + 0.25 \text{ wn36f} \\
& - 0.25 \text{ wn36b} + 0.5 \text{ wn46yf} - 0.5 \text{ wn46yb} + 0.75 \text{ wn47f} - 0.75 \text{ wn47b} \\
& + 0.5 \text{ wn49f} - 0.5 \text{ wn49b} - 0.5 \text{ wn84f} + 0.5 \text{ wn84b} + 0.25 \text{ wn88f} \\
& - 0.25 \text{ wn88b} + 0.25 \text{ wn70f} - 0.25 \text{ wn70b} + \text{ wn71f} - \text{ wn71b} + \text{ wn72f} \\
& - \text{ wn72b} - 0.25 \text{ wn110} + 0.75 \text{ wn112} - 0.25 \text{ wn113} - 0.5 \text{ wn134}
\end{aligned}$$

$$\begin{aligned}
\text{wXVII} = & - 0.75 \text{ w1f} + 0.75 \text{ w1b} + 0.5 \text{ w2f} - 0.5 \text{ w2b} - 0.25 \text{ w3f} + 0.25 \text{ w3b} \\
& - 0.75 \text{ w4f} + 0.75 \text{ w4b} - 0.25 \text{ w5f} + 0.25 \text{ w5b} + 0.25 \text{ w7} - 0.75 \text{ w9} \\
& + 0.75 \text{ w10} - 0.25 \text{ w12f} + 0.25 \text{ w12b} - 0.25 \text{ w16} + 1.25 \text{ w17} \\
& + 0.75 \text{ w20} - 0.25 \text{ w22} - 0.25 \text{ w23} + 1.25 \text{ w26} + 0.5 \text{ w27} + 0.5 \text{ w28} \\
& + 0.5 \text{ w30} - 0.25 \text{ w31} - 0.5 \text{ w33f} + 0.5 \text{ w33b} + 0.75 \text{ w35} + 0.5 \text{ w39} \\
& - 0.25 \text{ w40f} + 0.25 \text{ w40b} - 0.25 \text{ wa40f} + 0.25 \text{ wa40b} + 1.25 \text{ w41f} \\
& - 1.25 \text{ w41b} + 1.25 \text{ w44} - 1.5 \text{ w47f} + 1.5 \text{ w47b} - 0.25 \text{ w50} + 0.5 \text{ w53} \\
& - 0.25 \text{ w54f} + 0.25 \text{ w54b} + 0.25 \text{ w58f} - 0.25 \text{ w58b} + 0.5 \text{ w60} \\
& - 0.25 \text{ w61} + \text{ wn7f} - \text{ wn7b} - 0.25 \text{ wn9f} + 0.25 \text{ wn9b} + \text{ wn17f} - \text{ wn17b} \\
& + 0.5 \text{ wn18f} - 0.5 \text{ wn18b} - 0.5 \text{ wn19f} + 0.5 \text{ wn19b} - 0.25 \text{ wn24xf} \\
& + 0.25 \text{ wn24xb} - 0.25 \text{ wn24y} + 0.75 \text{ wn36f} - 0.75 \text{ wn36b} + 0.5 \text{ wn46yf} \\
& - 0.5 \text{ wn46yb} + 1.25 \text{ wn47f} - 1.25 \text{ wn47b} + 0.5 \text{ wn49f} - 0.5 \text{ wn49b} \\
& - 0.5 \text{ wn84f} + 0.5 \text{ wn84b} + 0.75 \text{ wn88f} - 0.75 \text{ wn88b} - 0.25 \text{ wn70f} \\
& + 0.25 \text{ wn70b} + \text{ wn72f} - \text{ wn72b} + 0.25 \text{ wn110} + 0.25 \text{ wn112} \\
& + 0.25 \text{ wn113} - 0.5 \text{ wn134}
\end{aligned}$$

$$\begin{aligned}
\text{wXVIII} = & - 0.5 \text{ w1f} + 0.5 \text{ w1b} - 0.5 \text{ w3f} + 0.5 \text{ w3b} - 0.5 \text{ w4f} + 0.5 \text{ w4b} - 0.5 \text{ w5f} \\
& + 0.5 \text{ w5b} + 0.5 \text{ w7} - 0.5 \text{ w9} + 0.5 \text{ w10} - 0.5 \text{ w12f} + 0.5 \text{ w12b} - 0.5 \text{ w16} \\
& + 0.5 \text{ w17} + 0.5 \text{ w20} - 0.5 \text{ w22} - 0.5 \text{ w23} + 0.5 \text{ w26} - 0.5 \text{ w31} \\
& + 0.5 \text{ w35} - 0.5 \text{ w40f} + 0.5 \text{ w40b} - 0.5 \text{ wa40f} + 0.5 \text{ wa40b} + 0.5 \text{ w41f} \\
& - 0.5 \text{ w41b} + 0.5 \text{ w44} - \text{ w47f} + \text{ w47b} - 0.5 \text{ w50} - 0.5 \text{ w54f} + 0.5 \text{ w54b} \\
& + 0.5 \text{ w58f} - 0.5 \text{ w58b} - 0.5 \text{ w61} - 0.5 \text{ wn9f} + 0.5 \text{ wn9b} - \text{ wn14f} \\
& + \text{ wn14b} - \text{ wn19f} + \text{ wn19b} - 0.5 \text{ wn24xf} + 0.5 \text{ wn24xb} - 0.5 \text{ wn24y} \\
& + 0.5 \text{ wn36f} - 0.5 \text{ wn36b} + 0.5 \text{ wn47f} - 0.5 \text{ wn47b} + 0.5 \text{ wn88f} \\
& - 0.5 \text{ wn88b} - 0.5 \text{ wn70f} + 0.5 \text{ wn70b} + 0.5 \text{ wn110} + 0.5 \text{ wn112} \\
& + 0.5 \text{ wn113}
\end{aligned}$$

$$\begin{aligned}
\text{wXIX} = & - 0.5 \text{ w1f} + 0.5 \text{ w1b} - 0.5 \text{ w3f} + 0.5 \text{ w3b} - 0.5 \text{ w4f} + 0.5 \text{ w4b} \\
& - 0.5 \text{ w5f} + 0.5 \text{ w5b} + 0.5 \text{ w7} - 0.5 \text{ w9} + 0.5 \text{ w10} - 0.5 \text{ w12f} \\
& + 0.5 \text{ w12b} - 0.5 \text{ w16} + 0.5 \text{ w17} + 0.5 \text{ w20} - 0.5 \text{ w22} - 0.5 \text{ w23} \\
& + 0.5 \text{ w26} - 0.5 \text{ w31} + 0.5 \text{ w35} - 0.5 \text{ w40f} + 0.5 \text{ w40b} - 0.5 \text{ wa40f} \\
& + 0.5 \text{ wa40b} + 0.5 \text{ w41f} - 0.5 \text{ w41b} + 0.5 \text{ w44} - \text{w47f} + \text{w47b} \\
& - 0.5 \text{ w50} - 0.5 \text{ w54f} + 0.5 \text{ w54b} + 0.5 \text{ w58f} - 0.5 \text{ w58b} - 0.5 \text{ w61} \\
& + \text{wn6f} - \text{wn6b} + \text{wn7f} - \text{wn7b} + 0.5 \text{ wn9f} - 0.5 \text{ wn9b} - \text{wn19f} \\
& + \text{wn19b} - 0.5 \text{ wn24xf} + 0.5 \text{ wn24xb} - 0.5 \text{ wn24y} + 0.5 \text{ wn36f} \\
& - 0.5 \text{ wn36b} + 0.5 \text{ wn47f} - 0.5 \text{ wn47b} + 0.5 \text{ wn88f} - 0.5 \text{ wn88b} \\
& - \text{wn61f} + \text{wn61b} - 0.5 \text{ wn70f} + 0.5 \text{ wn70b} + 0.5 \text{ wn110} \\
& + 0.5 \text{ wn112} + 0.5 \text{ wn113}
\end{aligned}$$

Appendix C

Coal Analysis

The coal used at the pressurised pulverized coal combustion facility is the german lignite (from the rhenish coal-mining district).

Calorific Value

	unit	raw	dry	dry/ash-free
gross calorific value (G. C. V.)	kg/kJ	23352	25775	26919
net calorific value (N. C. V.)	kg/kJ	22173	24727	25824

Proximate Analysis

	unit	raw	dry	dry/ash-free
water	mass-%	9.40	-	-
ash	mass-%	3.85	4.25	-
volatiles	mass-%	45.93	50.70	52.95
coke (fix)	mass-%	40.82	45.05	47.05
summation	mass-%	100.00	100.00	100.00

Elementary Analysis

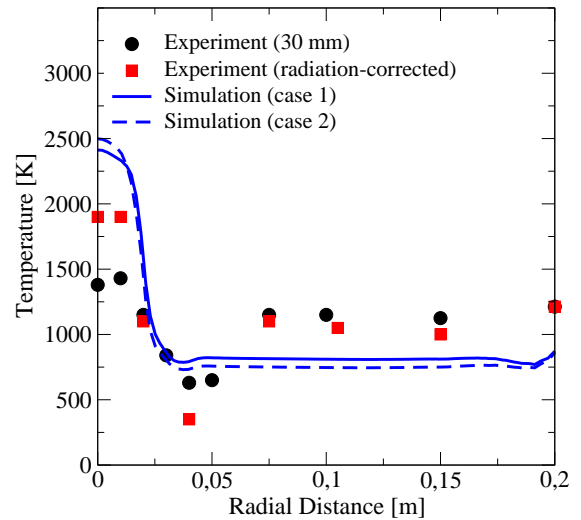
	unit	raw	dry	dry/ash-free
water (H ₂ O)	mass-%	9.40	-	-
ash	mass-%	3.85	4.25	-
carbon (C)	mass-%	59.60	65.80	68.70
hydrogen (H)	mass-%	4.35	4.80	5.01
oxygen (O)	mass-%	21.81	24.06	25.15
nitrogen (N)	mass-%	0.67	0.74	0.77
sulfur (S)	mass-%	0.32	0.35	0.37
summation	mass-%	100.00	100.00	100.00

Appendix D

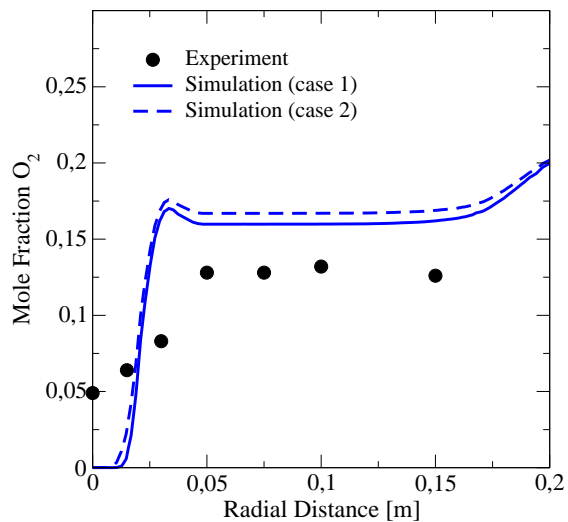
Influence of the Initial Composition of Volatiles

Species	Mole Fraction Case 1	Mole Fraction Case 2
CH ₄	0.19	0.11
H ₂	0.30	0.34
CO	0.22	0.28
CO ₂	0.29	0.27

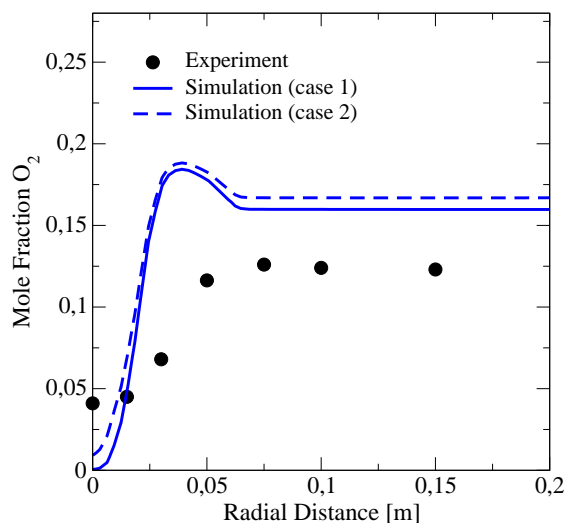
Composition of the volatiles escaped from the coal at 1 bar (case 1 = experimental data from [57]; case 2 = simulation from [2] corresponding to the experimental data of [57]) .



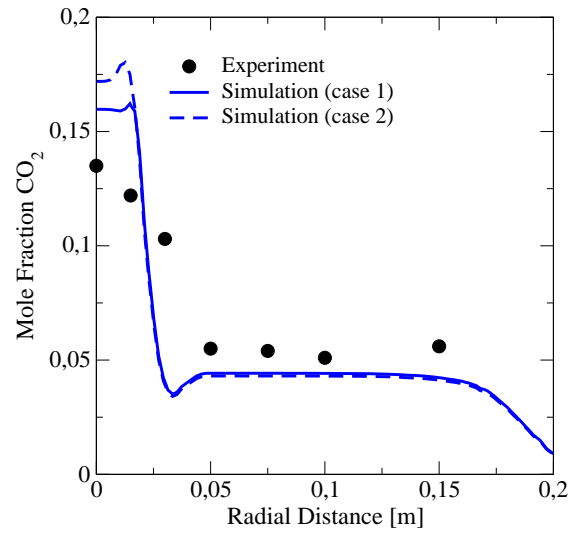
Comparison of the temperature predicted by the simulation (line = case 1; dotted line = case 2) with the experimental data at a distance of 30mm from the burner.



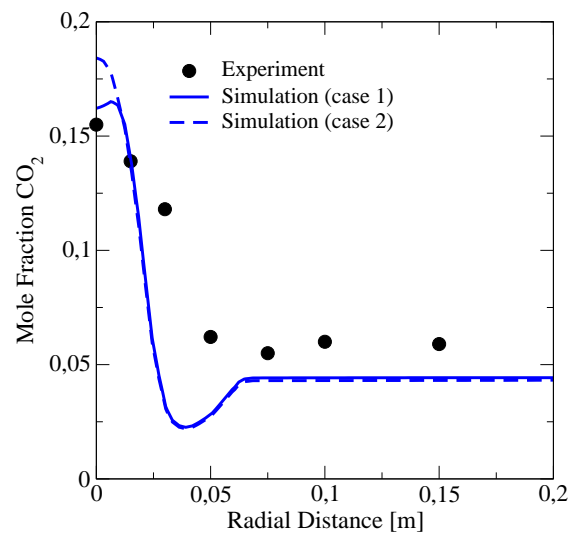
Comparison of the O₂ mole fraction predicted by the simulation (line = case 1; dotted line = case 2) with the experimental data at a distance of 30mm from the burner.



Comparison of the O₂ mole fraction predicted by the simulation (line = case 1; dotted line = case 2) with the experimental data at a distance of 100mm from the burner.



Comparison of the CO₂ mole fraction predicted by the simulation (line = case 1; dotted line = case 2) with the experimental data at a distance of 30mm from the burner.



Comparison of the CO₂ mole fraction predicted by the simulation (line = case 1; dotted line = case 2) with the experimental data at a distance of 100mm from the burner.

Appendix E

Nomenclature

Latin Letters

A_{ir}	frequency factor of elementary reaction ir
a_s	strain rate
a_{ij}	number of atoms of element j in a molecule of species i
c_p	heat capacity at constant pressure
c_{p_i}	heat capacity at constant pressure of species i
c_χ	constant in the model of the turbulent scalar dissipation rate, $c_\chi = 2.0$
c_1	k- ϵ model constant, $c_1 = 1.44$
c_2	k- ϵ model constant, $c_2 = 1.92$
d_p	particle diameter
Da	Damköhler number
D_i	binary diffusion coefficient of species i
E_{ir}	activation energy of elementary reaction ir
\mathbf{E}	identity matrix
f	probability density function (Pdf)
\mathbf{g}	gravitational acceleration
h	enthalpy
\mathbf{j}_i	molecular diffusion flux vector
\mathbf{j}_q	molecular heat flux vector
k	turbulent kinetic energy
k_{ir}	rate of reaction ir
L	characteristic length scale
Le	Lewis number
l_0	integral length scale
l_f	laminar flame thickness

l_m	mixing length
n_{ir}	temperature exponent of elementary reaction i
n_s	number of chemical species
P	probability
Pdf	probability density function
Pr	Prandtl number
p	pressure
p_i	partial pressure of species i
\dot{q}_r	radiative heat loss
RIF	Representative Interactive Flamelet
Re	Reynolds number
R_{gas}	the universal gas constant, $R_{gas} = 8.3143 \cdot 10^3 \text{ J}/(\text{kmol K})$
\mathbf{S}	rate of strain tensor
Sc	Schmidt number
s_L	laminar burning velocity
T	temperature
t	time
t_τ	Kolmogorov time scale
\mathbf{u}	sample space vector of velocity vector
V	volume
\mathbf{v}	velocity vector
W_i	molecular weight of species i
X_i	mole fraction of species i
\mathbf{x}	spatial vector
Y_i	mass fraction of species i
Z	mixture fraction
Z_j	mass fraction of chemical element j

Greek Letters

α_p	Planck's radiation coefficient
β	arbitrary coupling function
$\Delta h_{f,i}^0$	heat formation of species i
δ	Dirac delta function
ϵ	dissipation of turbulent kinetic energy
η	Kolmogorov length scale, sample space of the mixture fraction
κ	bulk viscosity

λ	thermal conductivity
λ	normalized air/fuel ratio
μ	dynamic viscosity
ν	kinematic viscosity
ν_j	number of atoms of element $j = \text{C, H, O, N}$ present in the mixture
$\nu'_{i,r}, \nu''_{i,r}$	stoichiometric coefficients of species i in reaction r
ω_i	chemical source term of species i
$\dot{\omega}_r$	reaction rate of reaction r
χ	scalar dissipation rate
Φ	equivalence ratio
ρ	density
σ_s	Stefan-Boltzmann constant, $\sigma_s = 5.669 \cdot 10^{-8} \text{ W}/(\text{m}^2\text{K}^5)$
τ_0	integral time scale
τ_c	characteristic time scale
τ_l	characteristic laminar time scale
τ_t	characteristic turbulent time scale
τ	Newtonian viscous stress tensor
∇	Nabla-operator, $\nabla = (\partial/\partial x, \partial/\partial y, \partial/\partial z)^T$
∇_u	divergence operator with respect to the three components of velocity, $\nabla_u = (\partial/\partial u_1, \partial/\partial u_2, \partial/\partial u_3)^T$

Symbols

\mathcal{L}	differential operator
---------------	-----------------------

Superscripts

$\overline{(\quad)}$	spatial averaging
$\overline{(\quad)}$	ensemble averaging
$\langle\langle(\quad)\rangle\rangle$	ensemble averaging
$\overline{(\quad)'}^{\text{Favre}}$	Favre ensemble averaging
$(\quad)'$	fluctuation around ensemble average
$(\quad)''$	fluctuation around Favre ensemble average

Subscripts

st	stoichiometric
t	turbulent
u	unburnt

Lebenslauf (Curriculum Vitae)

Persönliche Daten

Name: Sylvie Honnet
Geburtsdatum: 23. Juni 1978
Geburtsort: Evreux (Frankreich)
Familienstand: verheiratet
Nationalität: französisch

Schulbildung

1984-1989: Grundschule Nagel-Seez-Mesnil/Beaubray (F)
1989-1993: Collège Guillaume de Conches (F)
1993-1996: Lycée Verneuil-sur-Avre (F)
Abschluss: Abitur

Studium

1996-2001: Maschinenbaustudium an der INSA Rouen (F)
Abschluss: Diplom

Berufliche Tätigkeit

10/01- 08/07: wissenschaftliche Mitarbeiterin am Institut für
Technische Verbrennung der RWTH Aachen

